IChF
Institute of Physical Chemistry PAS

PhD Dissertation

Effects of Confinement on Ionic Liquids

Carolina Cruz Cardona

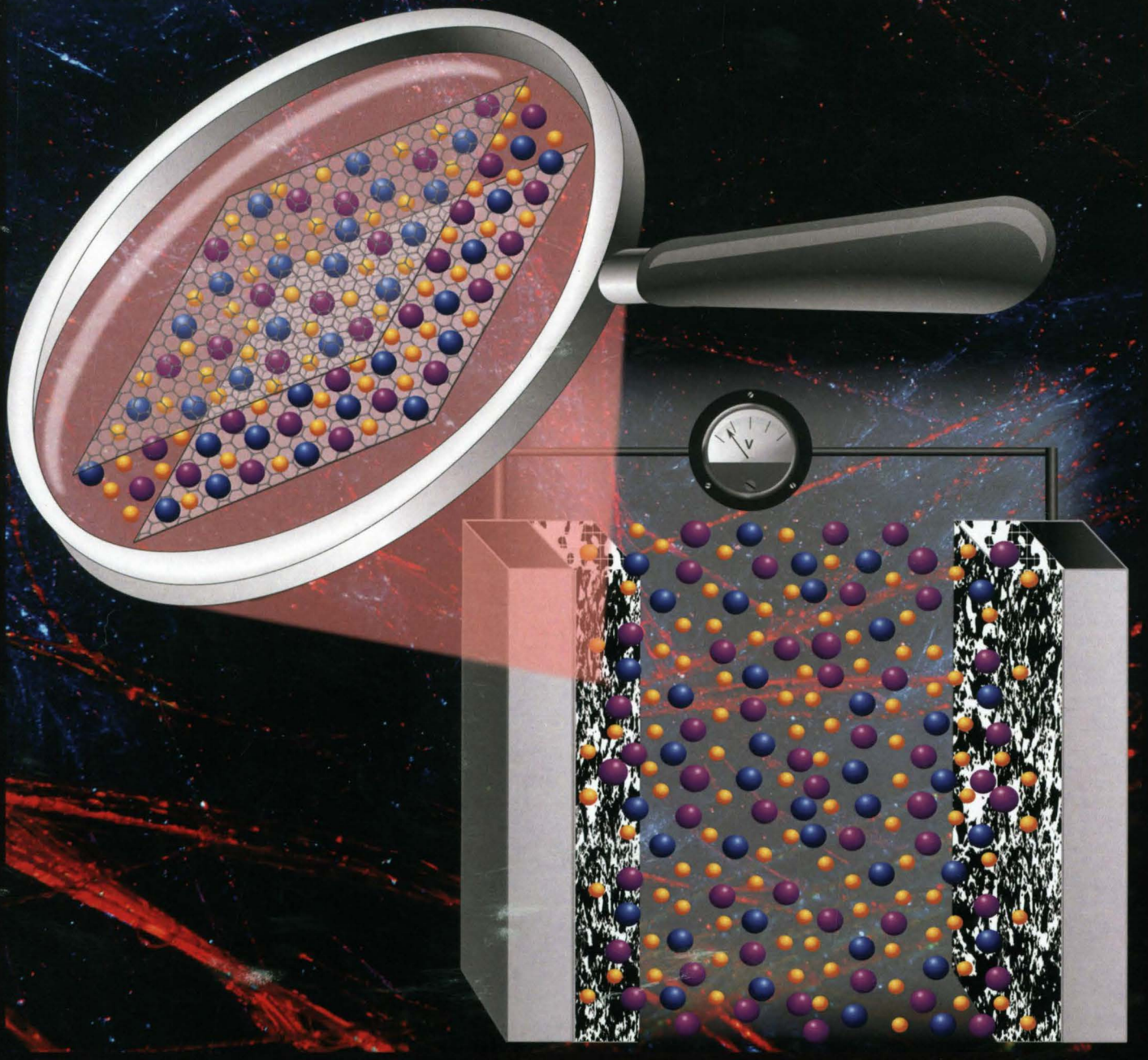

Effects of Confinement on Ionic Liquids

Carolina Cruz Cardona

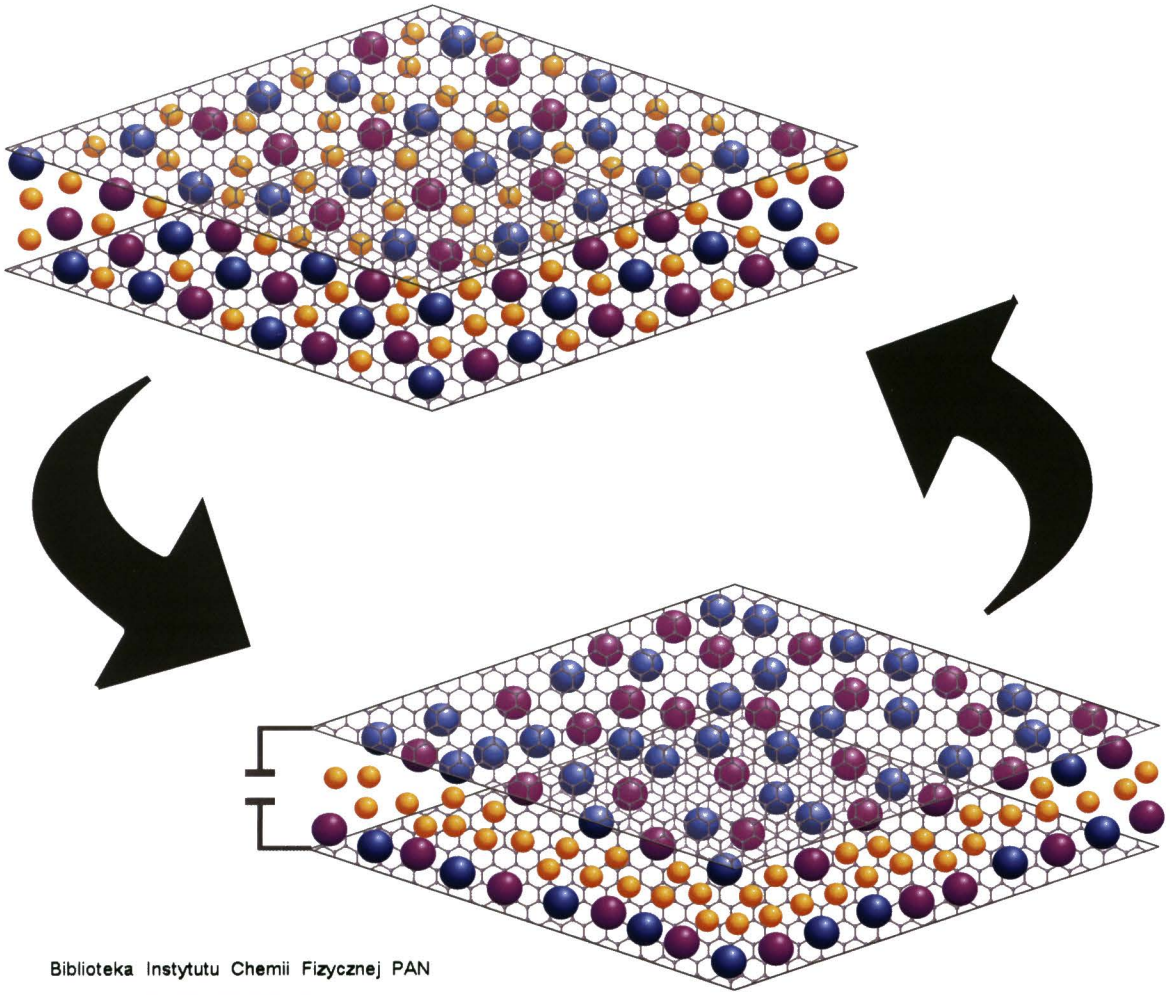

INSTITUTE OF PHYSICAL CHEMISTRY

POLISH ACADEMY OF SCIENCES

June, 2021

Institute of Physical Chemistry
Polish Academy of Sciences
Kasprzaka 44/52 01-224
Warsaw Poland

Effects of confinement on ionic liquids

Carolina Cruz Cardona

Supervisor: **Prof. dr hab. Alina Ciach**
Second supervisor: **Prof. Enrique Lomba**

This dissertation was prepared within the International PhD Studies at the Institute of Physical Chemistry of the Polish Academy of Sciences in Warsaw in the research group of Complex Systems and Chemical Processing of Information in collaboration with Prof. Enrique Lomba from the Institute of Physical Chemistry Rocasolano (IQFR) in Madrid.

Warsaw
June, 2021

To my parents

Funding

This research is part of a project that has received funding from the European Union's Horizon 2020 research and innovation programme under the Marie Skłodowska-Curie grant agreement No. 711859.

Scientific work funded from the financial resources for science in the years 2017-2022 awarded by the Polish Ministry of Science and Higher Education for the implementation of an international co-financed project.

Acknowledgments

First of all, I would like to express my deep gratitude to my supervisor, Professor Alina Ciach. Her help, support, and guidance have been valuable. She was always available despite her many responsibilities. Her extraordinary patience and confidence in my work were fundamental for the culmination of my thesis. It was indeed a pleasure and an inspiration working with you. I also would like to express my sincere appreciation to my co-supervisor, Professor Enrique Lomba, for his advice and guidance during my secondment at the Institute of Physical Chemistry Rocasolano (IQFR) in Madrid.

During this process, I have had the great pleasure of working with Dr. Svyatoslav Kondrat, who contributed significantly to my thesis project. He was always available for discussions and to clarify my doubts.

Many thanks to my colleagues and friends, especially to Andrés Arango and Horacio Serna, for creating a thriving discussion environment. They provided me helpful comments during my research.

Sincere thanks to all the staff and colleagues at the Institute of Physical Chemistry who helped me during my postgraduate work, and thanks to all those people who, in one way or another, contributed to the development of this work.

At this point, I could not forget thanking my former supervisor, Professor Daniel Barragán, for guiding me into the world of science. He drove me in the first instance to pursue a Ph.D. and do research.

Finalmente quiero dedicar estas palabras en mi español nativo para agradecer a mi familia, especialmente a mis padres que con su amor, motivación y apoyo me han llenado de fortaleza. Quiero agradecer profundamente a mi esposo, Amaury Toloza, quien me ha acompañado a lo largo del doctorado, con paciencia y comprensión. Él ha sido mi soporte emocional, así mismo sus habilidades en programación fueron de gran ayuda. Sin mi familia y mi esposo, nada de este trabajo hubiera sido posible.

Abstract

Ionic liquids and ionic liquids-solvent mixtures have attracted scientific interest and become the research focus as solvents in the green chemistry field and in surface science and physical chemistry due to their remarkable properties and features such as wide electrochemical and thermal stability, low vapor pressure, and the ability to mix them in order to tune specific properties. One of the most important applications of ILs is in the development and design of energy storage devices such as fuel cells, batteries, and supercapacitors, where ILs are usually in contact or confined by porous materials. Nevertheless, thermodynamic and structural properties of ILs/IL- mixtures near charged surfaces are not sufficiently understood. Moreover, these systems in the vicinity of their phase transformations exhibit some remarkable features, yet there is no theory able to describe the phase behavior of confined ionic liquids correctly. These difficulties in theoretical modeling are due to inhomogeneities and the interplay of entropic effects, dispersion, and long-range interactions.

This thesis is devoted to the theoretical description of ILs-solvent mixtures close to demixing. We have developed a mean-field model suitable for the IL-solvent mixtures confined by selective electrodes to fulfill this purpose. We have taken into account electrostatic forces, short-range dispersion interactions, and entropic effects in which we have implemented two approximations for describing excluded volume interactions, namely Carnahan-Starling and lattice-gas. Additionally, we have assumed selective electrodes within the parameter called *ionophilicity* that accounts for the surface's preference to ions or solvent. Thus, we have derived a grand-potential functional and minimized it to obtain the Euler-Lagrange (EL) equations for the excess density of ions and the charge density profiles. Then, we have proposed analytical and numerical approaches to solve the EL equations and found that the comparison between the analytical and numerical results is just valid at low voltages. Therefore, to study a wide range of voltages, we considered numerical results for further analysis.

We consider two cases. In the first case, the ILs-solvent mixture is in contact with a single electrode, and we demonstrate that, besides the well-known camel and bell-shaped capacitance, there is a *bird-shaped* capacitance that exhibits three peaks as a function of voltage, which emerges due to the proximity to demixing. Additionally, we find that although the camel-shaped capacitance is a signature of dilute electrolytes, such a shape can appear at high IL densities provided the electrode has a strong preference for solvent. Regarding the temperature effects, we find that the capacitance increases as the system's temperature is lowered to demixing, and

an enhancement of the energy storage accompanies such an increase.

In the second case, we study the IL-solvent mixture confined by a slit-shaped nanopore wider than a few ion diameters and reveal that such systems can undergo a capillary ionization transition where the pores spontaneously ionize or de-ionize upon infinitesimal changes of temperature, slit width, or voltage. We show that capillary ionization could be voltage-induced, and interestingly, such transition is followed by a subsequent de-ionization as the voltage increases. We find that ionization transitions produce sharp jumps in the accumulated charge and stored energy, finding practical applications in energy storage and heat-to-energy conversion.

Finally, we perform molecular dynamics simulations where we investigate the concentration fluctuations in a simple model of electrolyte, that is, two charged Lennard-Jones spheres in a solution of an uncharged Lennard-Jones liquid, confined between electrodes formed by parallel graphene layers. Using two approaches: constant potential and extensive constant charge simulations, the effect of the proximity to the demixing transition on the electric double layers is analyzed. In agreement with our previous theoretical findings, we find there is a considerable enhancement of the capacitance when approaching the demixing transition for dilute ionic solutions. This enhancement tends to disappear when the ionic concentration is increased. We also find that the ‘‘bird-like’’ capacitance, predicted by our theory, appears when Lennard-Jones interactions are taken into account and may lead to phase separation.

Contents

List of Figures

List of Tables

Abbreviations

IL	Ionic liquid
EDL	Electrical double layer
EW	Electrochemical window
PB	Poisson-Boltzmann
CS	Carnahan-Starling
BK	Bikerman-Kornyshev
GCS	Gouy-Chapman-Stern
PZC	Potential of zero charge
OP	Order parameter
lg	Lattice-gas
EL	Euler-Lagrange
FD	Finite differences
BC	Boundary conditions
ci	Capillary ionization
vdW	van der Waals
sat	Saturation
LJ	Lennard-Jones

Symbols

k_B	Boltzmann constant
T	Temperature
a	Molecular size
ϵ_r	Dielectric constant
λ_B	Bjerrum length
λ_D	Debye length
Ω	Grand thermodynamic potential
γ	Packing parameter
ξ	Correlation length
h_s	Ionophilicity
T_c	Critical temperature
ϕ	Order parameter
u	Electrostatic potential
ρ	Ion density
β	Inverse k_BT
ρ_b	Bulk density
C	Differential capacitance
Q	Accumulated charge
E	Stored energy
Γ	Ion adsorption
X_D	Charging parameter
w	Slit width
c	Charge density
U	Applied voltage
ρ_c	Critical density
μ	Chemical potential
K	Dispersion interactions
ξ_0	Spatial extension of dispersion interactions

Chapter 1

Introduction

During the last decades, ionic liquids (ILs) and IL–solvent mixtures have become the focus of research in electrochemistry due to their intriguing properties, such as exceptional electrochemical and thermal stability, low vapor pressure, among others, which make them attractive materials for many applications [1, 2], for instance, in electrochemical reactions, as lubricants for micro and nanodevices [3], as extraction liquids for the purification of metals, colloids, and biomass, etc [2]. One of the key applications is in generation and energy storage as supercapacitors, batteries, solar cells, and fuel cells. In conventional electrolytes, ions are described as small and almost round particles with a uniform charge density immersed in a solvent and interacting with each other by Coulomb forces [2]. However, in ILs there is no solvent unless it is added or absorbed from the environment, ions are not round, and their molecular charge densities are non-uniform. Thus, the effect of short-range interaction between ions, the shape of the ions, and charge distribution are crucial factors for describing their properties in both bulk and at interfaces.

Despite the progress, the studies performed so far have focused on the room–temperature ILs and IL–solvent mixtures far from phase transitions. However, it is well–known that, for neutral fluids, the fluid structure at a surface undergoes drastic changes as the system approaches a phase transformation, such as wetting transition and capillary condensation [4]. In particular, to date, there is no theory able to describe the phase behavior of confined ionic liquids correctly, and these difficulties in theoretical modeling are due to spatial inhomogeneities and long-range interactions.

Confinement effects are also an interesting factor to study. In general, fluids under confinement are of particular scientific interest. A fundamental understanding is needed for industrial applications in oil and gas, catalytic chemical reactions, mixture separations, lubrication, and adhesion. The implementation and design of such processes involving fluid confined by micro and mesopore materials are empirical and lacking a microscopic basis [5]. Specifically, ILs under confinement exhibit remarkable properties in energy storage applications [6–9], capacitive deionization [10–12], and heat-to-energy conversion [13–15]. For instance, subnanometer pores filled with an electrolyte provide the highest achievable capacitance [16–18] and stored energy [19] but with slow dynamics [20–23]. Using neat ILs enhances the electrical energy stored in micro and mesopores [24]. Unfortunately, neat ILs exhibit slow dynamics, and to

improve their conductivity, ILs are mixed with solvents such as acetonitrile or water [25–28], allowing to speed up the charging kinetics [29]. These previous works have focused on micro and mesopores filled with IL-solvent mixtures far from phase transitions. However, confined fluids show an exciting physics close to state transformations. A classic example is a capillary condensation [30, 31] which has numerous practical applications, particularly in determining a pore-size distribution of micro and mesoporous materials [32–34].

1.0.1 Scope of the thesis

This thesis is devoted to studying ionic liquid–solvent mixtures close to phase separation under various degrees of confinement. Firstly, we consider a mixture in contact with a single planar electrode. Then, we study the same IL-solvent mixture confined into slit-shaped pores substantially wider than the ion diameter. We propose a model within the mean-field theory to analyze the electrical double layers' temperature dependence close to demixing. The solvent is treated as a continuum (appropriate for small solvent molecules, such as water or acetonitrile), but ILs are described as amenable to phase separate into the ion-rich and ion-dilute phases. We study the influence of important parameters in the system's behavior, and special attention is paid to the temperature effects in the capacitance and the energy stored in the electrical double layer.

For a system composed of a single electrode, we show that the capacitance and stored energy become sensitive functions of temperature in the vicinity of demixing. We also demonstrate the emergence of a new, *bird*-shaped capacitance, having three peaks as a function of voltage. In the case of confinement by slit-shaped mesopores, we study a capillary phase transition induced by both confinement and voltage applied to the pore walls. We demonstrate that the pores can become spontaneously ionized or deionized in response to small temperature changes or potential differences applied to a pore. We show that such capillary ionization goes along with abrupt changes in charge and energy storage, finding practical applications in electrochemical energy storage and generation.

The thesis is organized as follows:

- Chapter 2: From the literature, we present a brief introduction and general description of the electrical double layer (EDLs) model and explain the well-known differential capacitance shapes: camel and bell. Next, we devote a section to the definition, properties, and applications of ionic liquids. Finally, we explain the electrical double layer in ionic liquids, and there is a section devoted to the confinement effects in such systems.
- Chapter 3: From the literature, we describe phase transitions, specifically the first-order demixing transition in binary mixtures. The geometry-induced phase transitions are discussed, in particular, the phase transitions in charged systems. In addition, we present the macroscopic derivation of the Kelvin equation.
- Chapter 4: We develop a generic model by combining the Poisson-Boltzmann and the mean-field theory for the demixing transition to describe a mixture of ionic liquid (IL) and

neutral solvent in contact with two planar electrodes. For describing the excluded-volume interaction, we consider two approximations: lattice-gas and Carnahan-Starling approximations. Additionally, we obtain the bulk phase diagram (for each excluded volume expression) and derive the Euler-Lagrange equations that result from the minimization of the grand thermodynamic potential. Finally, we present the thermodynamic characteristics to study the system's behavior.

- Chapter 5: We present analytical and numerical approaches to solve the proposed generic model. It is worth noting that the analytical approach is developed for the single-surface system. Regarding the numerical solution, we implement a finite differences scheme forwarded in time and centered in space.
- Chapter 6: Analytical and numerical results are presented for the case of a single surface in contact with an IL-solvent mixture. We show the charge density and ion density profiles as well as the differential capacitance comparing the analytical and numerical solutions of the model. Finally, we compute the thermodynamic characteristics of the system under consideration using the numerical solution.
- Chapter 7: We show the capillary ionization phase transition of an IL-solvent mixture confined by a slit-shaped mesopore. We obtain results by considering three cases: non-polarized slit mesopore, equally charged slit mesopore and oppositely charged electrodes. We demonstrate that capillary ionization can be induced not only by confining the mixture but also by applying voltage.
- Chapter 8: We perform Molecular Dynamics (MD) simulations to explore the bulk behavior and locate a phase separation. The results are compared to the Hypernetted-chain (HNC) theory. Then, we perform MD of a mixture of IL and solvent confined by two electrodes oppositely charged. A few simulations were run using a constant potential method in order to confirm that, for the charges and voltages of interest, the computationally less expensive constant charge approaches are accurate enough. The simulations were performed in LAMMPS, and Prof. Enrique Lomba, from the Institute of Physical Chemistry Rocasolano (IQFR) in Madrid, provided the HNC codes.

The majority of the results presented in the thesis have been published in the following papers:

1. C. Cruz, A. Ciach, E. Lomba, and S. Kondrat. ''Electrical Double Layers Close to Ionic Liquid-Solvent Demixing''. *Journal of Physical Chemistry C*, vol. 123, pp. 1596-1601, **2019**. DOI: 10.1021/acs.jpcc.8b09772.

2. C. Cruz, S. Kondrat, E. Lomba, and A. Ciach. ''Effect of proximity to ionic liquids-solvent demixing on electrical double layers''. *Journal of Molecular Liquids*, vol. 294, pp.111368, **2019**. DOI: 10.1016/j.molliq.2019.111368.

3. C. Cruz, S. Kondrat, E. Lomba, and A. Ciach. ''Capillary Ionization and Jumps of Capacitive Energy Stored in Mesopores''. *Journal of Physical Chemistry C*, vol. 125, pp. 10243–10249, **2021**. DOI: 10.1021/acs.jpcc.1c00624.

4. C. Cruz, E. Lomba, and A. Ciach. ‘‘Capacitance response and concentration fluctuations close to ionic liquid-solvent demixing’’. Submitted to *Journal of Molecular Liquids*, **2021**.

5. C. Cruz and A. Ciach. ‘‘Phase transitions and electrochemical properties of ionic liquids and ionic liquid - solvent mixtures’’. Submitted to *Molecules*, **2021**.

Chapter 2

Ionic Liquids and Electrical Double Layers

In this chapter, a brief introduction and general description regarding electrical double layers (EDLs) is presented. Next, in Section 2.2, we present the definition and properties of ionic liquids (ILs) and explain a few applications of them. Section 2.3 treats EDLs displayed by ILs. The well-known camel and bell-shaped capacitances are presented, and based on the packing parameter proposed by Kornyshev, we discuss their nature. Finally, confinement effects in ILs are discussed.

2.1 The Electrical Double Layer (EDL) Model

The double-layer model is used to analyze the ion's behavior in the vicinity of a charged surface. Electrical double layers (EDL) result from the formation of a'cloud' rich in ions with a charge of a sign opposite to the surface charge (known as *counterions*) and poor in ions of the same sign (known as *coions*). The EDL width is influenced by the competition between the ion's thermal motion, which tends to homogenize their distribution, and the Coulomb interactions, which attract the counterions to the surface [35, 36].

The classical theory of electrolytes was developed in the early $20th$ century, with the achievements of Gouy, Chapman, Debye, Hückel, and Langmuir gathered into the so-called Poisson-Boltzmann (PB) model [37, 38]. However, the first model for describing EDLs was proposed by Helmholtz in 1853. In the Helmholtz model (Figure 2.1a), the surface charge is neutralized by counterions which were assumed to be adsorbed at the electrode surface [39]. This model can be understood as a single layer of ions driven to the surface by its electric field, which is completely screened by the ionic layer.

On the other hand, the PB model is a mean-field model that considers the ions to be mobile in the electrolyte solution [39] and describes them as isolated point-like charges in a solvent represented by a continuum dielectric (Figure 2.1b) [35, 37, 40]. The Gouy-Chapman theory

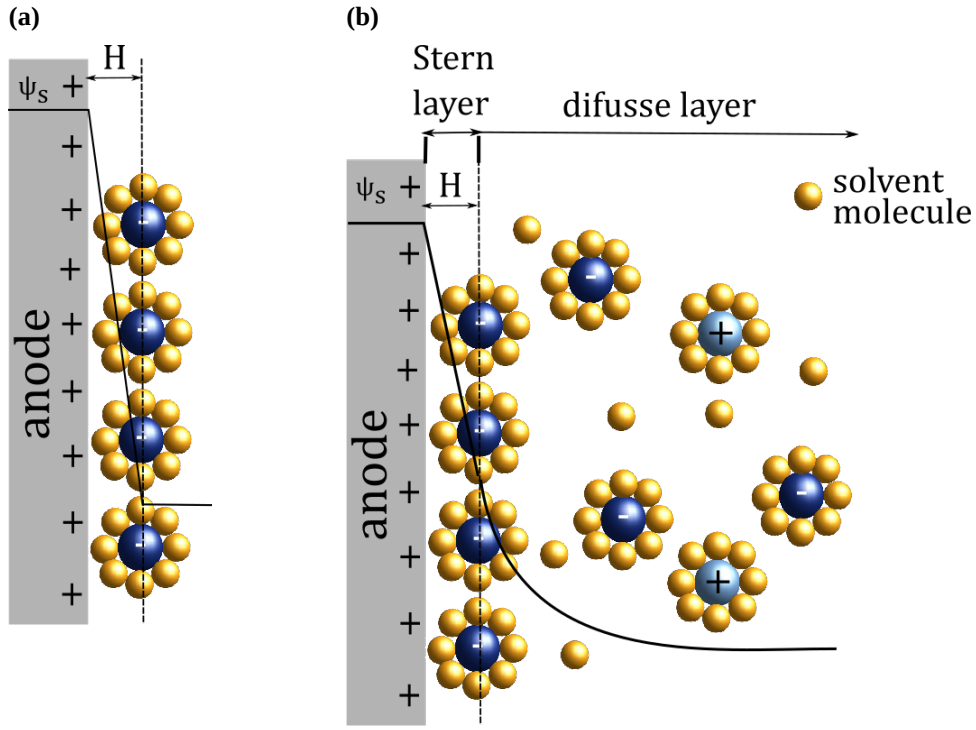

FIGURE 2.1 Schemes of the electric double layer structures. (a) Helmholtz Model. All the counterions are assumed to be adsorbed at the electrode surface. This structure is similar to the conventional dielectric capacitors with two planar electrodes separated by a distance H. **(b)** Poisson-Boltzmann (PB) model. The EDL consists of two parts, the Stern layer, which is a compact layer of immobile ions that are strongly adsorbed to the electrode surface, and the diffuse layer, where the ions are mobile.

assumes ions have no physical limitations to approach the surface. However, Stern modified this model proposing that ions have a finite size and they are not at the surface, but at some distance, H away from it [2]. Thus, there is a compact layer of counterions known as the Stern layer and a diffuse layer. In the Gouy-Chapman-Stern theory (GCS), the potential drops down linearly in the Stern layer and then exponentially through the diffuse layer [2]. Within the linearized PB (Debye–Hückel approximation), the thickness of the EDL is given by the Debye length

$$\lambda_D = (4\pi\rho_b\lambda_B)^{-1/2}, \tag{2.1}$$

where ρ_b is the ion density, and λ_B is the Bjerrum length given by

$$\lambda_B = e^2/(k_B T\epsilon_r) \tag{2.2}$$

where ϵ_r is the dielectric constant.

One significant effect which is not considered in the GCS theory is the excluded volume interactions that take into account the physical size of ions. The excluded volume interactions restrict the absorption of counterions and hence, influence the charge density in the EDL [41]. Even if the ion charge correlations and fluctuations are neglected, the application of the PB model to EDLs still forms the basis of the understanding of electrolyte solutions. For instance,

it predicts the well–known U–shaped dependence of the EDL capacitance on the applied potential [37].

2.1.1 Debye–Hückel theory

The key feature of the Debye–Hückel treatment is the linearization of the differential equation for the electrostatic potential (obtained from the Poisson's equation of electrostatics with the Boltzmann factor of statistical mechanics), which can be solved straightforwardly, leading to simple expressions for the thermodynamic properties of electrolyte solutions.

Let us consider the electrostatic potential, u, which satisfies the Poisson equation:

$$\frac{d^2u(z)}{dz^2} = -\frac{4\pi e}{\epsilon_r}c(z) \tag{2.3}$$

where $c(z) = \rho_+(z) - \rho_-(z)$ is the dimensionless charge density. The corresponding ion densities, $\rho_\pm(z)$, follow the Boltzmann distribution

$$\rho_\pm(z) = \rho_\pm \exp\left(\frac{eu(z)}{k_BT}\right) \tag{2.4}$$

where $\rho_\pm$ are the ion densities in the bulk where the potential decreases to zero and, due to charge neutrality in the bulk, $\rho_+ = \rho_- = \rho_b/2$. Additionally, the overall charge neutrality must satisfy

$$e\int_0^\infty c(z)dz = -\sigma \tag{2.5}$$

where σ is the surface potential [42]. By inserting Eq. (2.4) into Eq. (2.3), the Poisson-Boltzmann (PB) equation is obtained:

$$\frac{d^2u(z)}{dz^2} = \frac{2e\rho_b}{\epsilon_0\epsilon_r}\sinh\left(\frac{eu(z)}{k_BT}\right) \tag{2.6}$$

Eq. (2.6) is subjected to the boundary conditions: $du/dz(z \to \infty) = 0$ and $-du/dz(z = 0) = 4\pi e\sigma/\epsilon_r$, can be solved analytically provided that the surface potential is less than 25 mV and by approximating $\sinh(x) \overset{x\to 0}{\approx} x$ [42]. Under these assumptions, the Debye–Hückel equation for the electrostatic potential is obtained

$$u(z) = \frac{4\pi e\sigma}{\lambda_D\epsilon_r}\exp\left(-\frac{z}{\lambda_D}\right) \tag{2.7}$$

and, the corresponding density profiles and charge density are

$$\rho_\pm(z) = \rho_b \pm \frac{1}{\lambda_D}\frac{\mid\sigma\mid}{2e}\exp\left(-\frac{z}{\lambda_D}\right) \tag{2.8}$$

$$ec(z) = -\frac{\sigma}{\lambda_D}\exp\left(\frac{z}{\lambda_D}\right) \tag{2.9}$$

Subsequently, it was shown that the Debye–Hückel theory is exact in the limit of dilute

solutions, and thus, it is considered as a ‘‘limiting law’’, meaning that the thermodynamic properties of all electrolyte solutions must fulfill the Debye–Hückel expressions as the concentration decreases to zero [43].

2.2 Ionic Liquids (ILs)

Room-temperature ionic liquids (RTILs), or simply ionic liquids (ILs), are commonly defined as materials composed of an organic or inorganic anion and an organic cation that melt below $100\,^{\circ}\mathrm{C}$ to $150\,^{\circ}\mathrm{C}$. In conventional electrolytes, ions are described as small and almost round particles with a uniform charge density immersed in a solvent and interacting with each other by Coulomb forces [2]. However, in ILs, ions are not round, and their molecular charge densities are non-uniform. Additionally, there is no solvent unless it is added or absorbed from the environment. Due to these complex features, ILs are liquids at room temperature, and the effect of short-range interaction between ions, size and shape of the ions, and charge distribution are crucial factors for describing their properties in bulk and at interfaces.

Regarding their cation segment, ILs are commonly classified into four types: (1) alkylammonium-, (2) dialkylimidazolium-, (3) phosphonium-, and (4) *N*-alkylpyridinium-based ILs. Ammonium-based ILs exhibit electrochemical cathodic stabilities, low viscosities, and low melting points; thus, they have been used as electrolytes in electrochemical devices. Imidazolium-based ILs have been widely studied. They are easily synthesized and have remarkable stability under oxidative/reductive conditions. Therefore, imidazolium-based ILs are used as a catalyst to improve the reaction yield and the chemoselectivity of several organic reactions. However, it is important to note that the selection of this type of IL as a cosolvent for a reaction under basic conditions should be carefully considered to avoid undesired side reactions. For instance, in [44] the authors found that in a base-catalyzed Baylis-Hillman reaction in the presence of imidazolium-based ILs, the catalyst was deactivated due to a side reaction involving the imidazolium-based IL [45]. Pyridinium-based ILs are highly stable, and the catalytic role of this type of ILs is outstanding in the synthesis of some pharmaceutical agents [45]. Phosphonium-based ILs are the most thermally stable compared to the imidazolium- and pyridinium-based ILs. Thus, phosphonium-based ILs are suitable for reactions at higher temperatures (more than $100\,^{\circ}\mathrm{C}$). In [46], phosphonium-based ILs have been used for CO_2 capture.

ILs are versatile and have a unique combination of properties, meaning that, by mixing them and choosing the appropriate cation-anion combinations, it is possible to tune specific properties. The selection of the cation defines the stability of the IL, whereas its functionality is usually controlled by choosing the anion. Typically, ILs structure combines organic cations with either organic or inorganic anions. Figure 2.2 shows some common cations and anions to obtain ILs.

In a general view, most ILs remain in the liquid state up to temperatures in the range $200\,^{\circ}\mathrm{C}$ to $300\,^{\circ}\mathrm{C}$ (at atmospheric pressure), in contrast to water or common organic solvents that evaporate at lower temperatures [48]. Additionally, ILs have low volatility as a result of the strong ion–

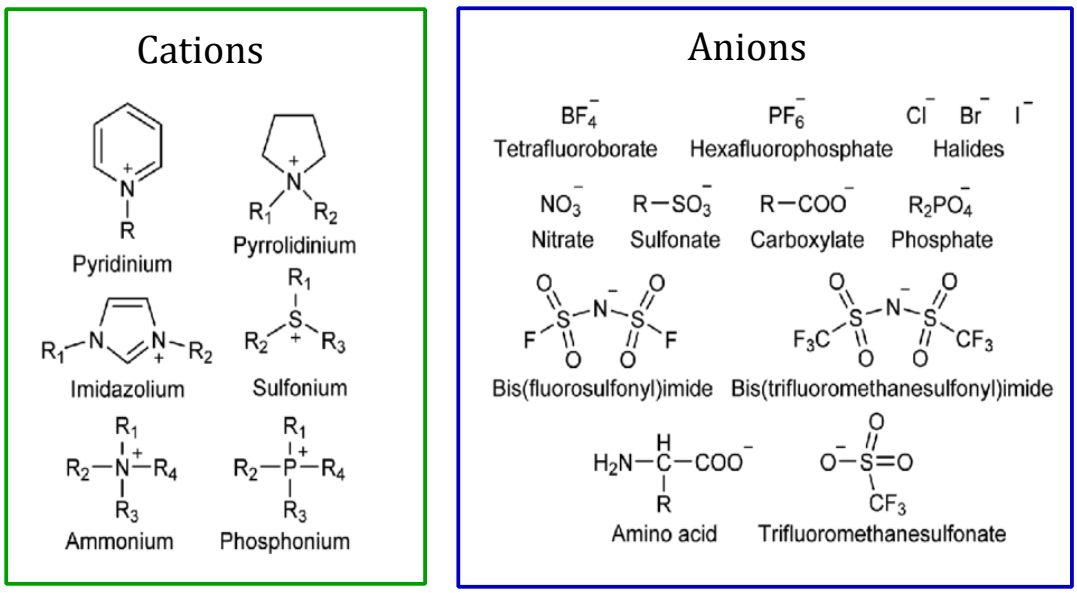

FIGURE 2.2 Typical cations and anions in ionic liquids. Typical basis of the cations are ammonium, imidazolium, sulfonium, piperidinium, and pyridinium ions. Halides, tetrafluoroborate, nitrate, sulfonate, carboxylate, phosphate, amino acid, among others, serve as a base of the anions for the preparation of ILs. The picture was modified from Ref. [47]

ion interactions [49]. Although, ILs are stable at high-operation temperatures in energy storage devices [50, 51], in some cases, undesired electrochemical reactions involving ILs could be activated [52]. Furthermore, it is important to note that, for temperatures higher than $200\,^{\circ}\mathrm{C}$ to $300\,^{\circ}\mathrm{C}$, ILs undergo thermal decomposition that may generate flammable and toxic gases [53, 54].

Another remarkable property of ILs is high viscosity. Conventional solvents exhibit viscosities within the range of $0.2\,\mathrm{cP}$ to $100\,\mathrm{cP}$ (at room-temperature), while the viscosity of ILs varies between $20\,\mathrm{cP}$ to $40.000\,\mathrm{cP}$ [55]. Despite the high ionic concentration (that could be understood as charge carriers), due to the high viscosity and low ion mobility, ILs have low conductivity at room-temperature [56], compared to the conventional aqueous electrolytes used in electrochemistry applications [1] [57]. For this reason, depending on the application (usually in generation and energy storage), ILs are mixed with a solvent, which facilitates the ionic diffusion.

Most of the ILs are electrochemically stable at charged interfaces. In applications such as batteries, supercapacitors, electrocatalysis, and electrodeposition, the ILs must remain as stable as possible in the potential range. The electrochemical window (EW), defined as the voltage range in which a substance is neither oxidized nor reduced, is a measure of such stability and is one of the most important characteristics to be identified for solvents and electrolytes. The large EW of some ILs allows achieving high electrode charge densities that are inaccessible for conventional electrolytes.

[1] Neat ILs have conductivity in the range of $0.1\,\mathrm{mS/cm}$ to $18\,\mathrm{mS/cm}$, while the conductivity of conventional aqueous electrolytes varies around $200\,\mathrm{mS/cm}$ to $800\,\mathrm{mS/cm}$.

2.2.1 Some applications of ILs

The interest in potential applications of ILs has grown during the last decades since they are promissory materials due to their unique combination of physical properties [58]. ILs can be found as lubricants, extraction liquids for purification of metals [59, 60], and biomass conversion [61, 62], green solvents for homogeneous and heterogeneous catalysis [1, 55, 63], media for electrochemical reactions and electrocatalysis [57, 64–66], antistatic agents in polymer science [52], carbon dioxide capture and separation [50], among others.

Specifically in energy storage, ILs are ideal electrolytes in dye sensitized solar cells, thermo–electrochemical cells, metal–air batteries, and supercapacitors due to their high ionic concentrations and stability [50]. Figure 2.3 shows the Ragone plot of a few types of energy storage devices. ILs are especially attractive in electrochemical double-layer capacitors (EDLCs) [2] which are microporous solids with an excellent electrochemical performance principally due to reversible ion adsorption in the porous electrodes [68]. The effects of confinement in ILs are discussed in Section 2.3.2.

In the Ragone plot, the power against the stored energy in the devices is presented. The specific energy is related to the ability of fast charging/discharging with minimal losses. In this sense, it is desired for the device to have high energy density without sacrificing power density. EDLCs have higher specific power and, in this sense, seem better than batteries; however, batteries have a higher specific energy. As a consequence, there is a growing interest focused on expanding the region occupied by EDLCs towards the upper-right corner of the plot. This is desirable since EDLCs can sustain several charging-discharging cycles and can be charged faster without involving any electrochemical reaction. With the growing interest on the development of renewable energy sources, these systems are potentially important since they may complement or even replace batteries in the energy storage field [2, 68].

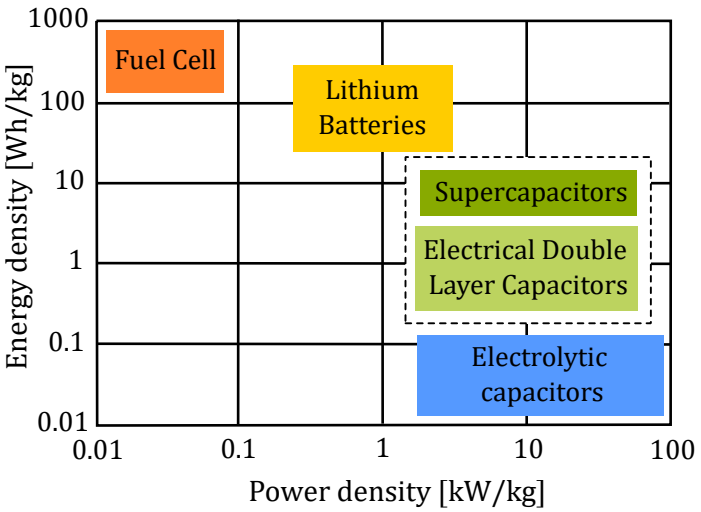

FIGURE 2.3 Ragone plot of a few types of energy storage devices. Specific power against specific energy is presented for some energy storage devices. Fuel cells exhibit the highest specific energy but at the same time the lowest specific power, while the EDLCs occupy a middle region between power and energy. The picture was modified from Ref. [58].

[2] Supercapacitors are classified into electrochemical double-layer capacitors (EDLCs) and pseudocapacitors, however, ILs are only used in EDLCs since pseudocapacitive mechanisms are generally not active in the presence of ILs [67].

2.3 Electrical Double Layers in Ionic Liquids

The classical models of EDL are only valid on the basis of dilute-solution approximation (concentrations below $0.01\,\mathrm{M}$) [40], but they are not longer valid for ILs and ILs–solvent mixtures due to strong Coulombic interactions and typically high concentrations of ions, at which the ion sizes can no longer be neglected [69–72]. Indeed, theories developed for EDLs have shown that excluded volume interactions are crucial to properly describe the structure of the EDL in ILs [41, 73–80]. In this respect, Kornyshev established the need for a paradigm change for describing EDLs in ILs. He proposed a mean-field lattice-gas model accounting for the finite-size of the ions on EDLs at IL–electrode interfaces and revealed that steric interactions restrict the absorption of counterions at an electrode and hence influence the charge density in the EDLs. This leads to the emergence of the so-called camel and bell-shape capacitances, obtained at low and high IL concentrations, respectively [78], instead of the Gouy-Chapman's U-shape.

ILs with and without dilution may exhibit self-assembly and non-monotonic variation of the EDL with respect to the concentration [40, 67]. In more detail, several experimental works have provided insights into the behavior of ILs at interfaces. One intriguing behavior is a strong layering effect at the interface observed for the first time by atomic force microscopy (AFM) [81–83], and then confirmed high-energy X-ray reflectivity [84, 85]. Although layering is present for all the ILs, Perkin *et al.* [86] have shown that substantial differences can be observed for the characteristic length, which is the distance between the successive layers of adsorbed ions. This indicates some kind of ''self-assembling'' properties, and in fact, the characteristic length can be related to the ions dimension, revealing the formation of patterns such as alternating cation-anion monolayers or tail-to-tail cation bilayers.

Temperature also plays an important role in the structure and capacitance of EDLs. However, contradictory results have been reported in the literature, and the consensus is yet to be reached as to whether capacitance increases or decreases with temperature and under which conditions. According to the Gouy-Chapman theory, the capacitance decreases for increasing temperature, but the experiments also showed the opposite trends [87–90]. For instance, Silva *et al.* [88] studied the ionic liquid 1-Butyl-3-methylimidazolium hexafluorophosphate ([BMIM][PF_6]) and three different electrodes and found that the differential capacitance increases with temperature at all potentials. Lockett *et al.* [87] found the same behaviour for imidazolium-based ionic liquids in contact with glassy carbon electrodes. More careful theoretical work suggested that both trends are possible [91–93], but there is no general agreement on the origin of this behavior. For instance, Holovko *et al.* [91] proposed that the increase of capacitance is related to the decreased inter-ionic interactions and weaker ion associations, while Chen *et al.* [93] argued that the temperature dependence of EDLs is chiefly determined by the strength and extent of van der Waals interactions. Interestingly, it was shown that the transition between the camel and bell-like capacitances could also be induced by varying temperature [93, 94], with the bell shape emerging at high temperatures due to breaking of 'ion

pairs' and consequently stronger screening [93].

2.3.1 Electrical double layer differential capacitance

The structure and the thermodynamic response of EDLs in ILs are strongly influenced by the interplay of finite size effects, van der Waals and Coulombic interactions [76, 95]. The classical methods for evaluating EDLs at electrode-ion interfaces involve measurements of the differential capacitance as a function of electrostatic potential, which is given by

$$C(U) = \frac{dQ}{dU} \tag{2.10}$$

where Q is the surface charge density at the electrode and U is the electrode potential.

One of the most interesting features of ILs is the complicated shape of the double layer capacitance as a function of the electrostatic potential. Most of the capacitance-voltage curves have one or two maxima depending on the type of IL, temperature, and the nature of the electrodes [96]. In order to get a deeper understanding of the differential capacitance shapes, Kornyshev *et al.* [2,97] proposed a mean-field theory that provides a classification by using a packing parameter, γ, which corresponds to the ratio of the ionic density in bulk to its maximal value in the double layer.

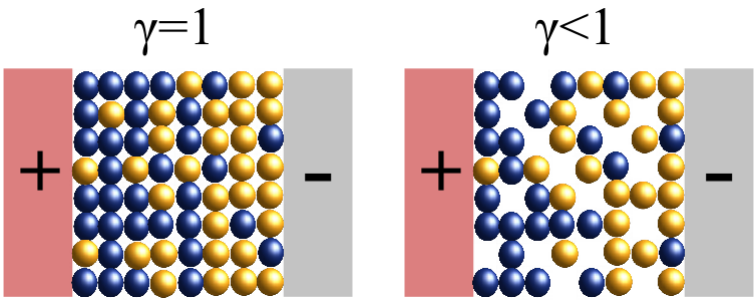

FIGURE 2.4 Schematic representation of the packing parameter, γ. Ionic liquid in contact with two electrodes of opposite charge. Blue spheres denote anions, while yellow spheres denote cations. The scheme at the left represents the packing parameter $\gamma = 1$, and the scheme at the right represents the packing parameter $\gamma < 1$ where the empty spaces denote voids in the lattice. The picture was modified from Ref. [2].

From a qualitative point of view, the capacitance curve will be bell- or camel-shaped regarding the value of γ, and provided anions and cations are of the same size [78]. For $\gamma < 1$ (see Figure 2.4-(right)), there are some voids at the EDL that will be filled up by ions as voltage increases, as a consequence, the capacitance will increase, exhibiting the camel shape, *i.e.*, a minimum at the potential of zero charge (PZC) [3] and two symmetric maxima [98]. Likewise, those voids can be either understood as spaces occupied by solvent molecules. Once the voltage increases, the solvent molecules are expelled out, and the EDL will be filled by ions.

[3] A metallic electrode carries a charge density whose magnitude depends on its potential. The specific potential at which no charge is carried is known as the potential of zero charge. This is a distinctive quantity for a given metal/solvent interface, and it is independent of the ions in the case in which there is no specific adsorption.

On the other hand, if there are no voids or no solvent molecules, $\gamma = 1$ (see Figure 2.4-(left)), the counterions will start to accumulate at the electrode and the EDL will get thicker, consequently, the capacitance will decrease, demonstrating the bell shape, which has a single maximum at the PZC and decreases monotonically as voltage decreases [98]. This behavior has been studied theoretically [73–75, 78, 94, 99–103] and experimentally [80, 87, 104]. Figure 2.5 shows the well-known bell (red line) and camel-shaped (black line) capacitance curves at two different bulk densities, $\rho_b = 0.35$ and $\rho_b = 0.04$, respectively. The camel-shaped capacitance is a signature of dilute electrolytes ($\gamma < 1$) and has been extensively studied [73–75, 78, 94, 99–103].

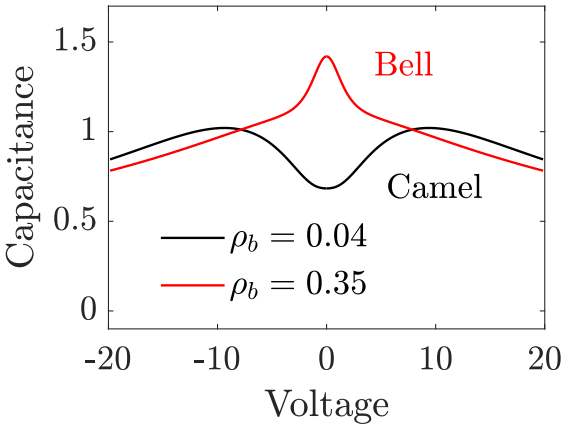

FIGURE 2.5 Capacitance shapes: Camel and Bell. Differential capacitance as a function of voltage showing the well-known camel and bell shapes at two different bulk densities, $\rho_b = 0.35$ and $\rho_b = 0.04$, respectively.

2.3.2 Confinement effects

ILs have become promising candidates, particularly when confined to pores of nanoscopic/mesoscopic dimensions [68, 105], for many applications in energy storage devices such as supercapacitors, dye-sensitized solar cells, and fuel cells [94, 105, 106]. The understanding of the structure of the ions on electrode surfaces and the properties of the electrical double layers (EDLs) displayed by the interactions between ions and polarized electrodes are of paramount importance and have been the subject of many theoretical and experimental works [107].

A deep understanding of the ILs behavior inside pores is still needed, and one of the features to analyze is whether the ions will locate preferentially at the surface or tend to keep a bulk-like structure [67]. Nuclear magnetic resonance (NMR) experiments performed on ILs confined in porous carbon electrodes revealed that the ILs spontaneously wet the carbon pores in the absence of any applied potential. However, when applying potential, charging occurs by adsorption of counterions and desorption of coions from the pores [108]. Similar results were reported from simulations of slit-shaped pores by performing molecular dynamics [109–111], or implementing classical density functional theory approaches [68, 112],

Specifically, in the theoretical formulations, Pizio *et al.* [68] found that the differential capacitance exhibits an oscillatory behavior as a function of the pore width, and the magnitude of the oscillations decreases when the electrostatic potential increases. Furthermore, the capacitance reaches a minimum value for narrower pores. The authors suggested that the capacitance oscillations could be related to the interference of the EDLs formed at the pore walls. Similar

behavior was also found by Jiang *et al.*in [112], where a classical density functional to describe an IL electrolyte inside a nanopore was implemented. The results unveil that the capacitance oscillations decay when the pore size increases from one to many times the ion diameter. Moreover, a peak capacitance was found due to the constructive interference of the EDLs at each wall. These results could imply that the optimal capacitance can be reached by controlling the pore width.

It is well known that confinement can induce phase transitions. For instance, capillary condensation of ILs mixtures in porous electrodes was reported in [113]. A simplified system of a single electrode pore immersed in a bulk electrolyte was considered, and, as a result of approaching capillary condensation, a fluctuation-enhanced capacitance over a range of surface potentials was found. This enhancement is attributed to density fluctuations in the screening electrolyte due to the phase transition. This enhanced capacitance was also found near the critical point. In real electrodes, the pore width is highly inhomogeneous; however, this could be advantageous for inducing fluctuation-enhanced capacitance. This fact relies on the idea that the topology of the pore can be tailored to display optimal capacitance over a specific potential window [113].

Another interesting behavior related to the confinement-induced phase transition is reported in [114]. Tuning-fork-based atomic force microscope measurements revealed a dramatic change of the ILs towards a solid-like phase denoting capillary freezing. This phase transition occurs below a threshold related to the nature of the confining materials; metallic surfaces promote freezing. Such behavior is explained by the fact that confinement shifts the freezing transition, and there is an influence of the electronic screening on IL wetting of the confining surfaces. These findings provide a better understanding of the ILs confined by metallic nanoporous since they treat an omitted phenomenon that, in fact, has application in the context of lubrication. In supercapacitors, for instance, freezing transitions are avoided by using disordered and rough surfaces. However, this may be beneficial in lubrication where the formation of a weak solid phase would prevent an undesired direct contact substrate–substrate [114].

In general, confinement will either promote or counteract phase transitions depending on the adsorbent-adsorbate interactions: repulsive interactions tend to lower the vapor-liquid or demixing critical points and depress the freezing temperature (here, the geometry of the confining environment is also important). The opposite behavior is induced by attractive wall-particle interactions [115].

Chapter 3

Phase Transitions in Mixtures

This chapter is devoted to describing phase transitions in mixtures. The emphasis is placed on the first-order demixing transition in binary mixtures (Section 3.1). In Section 3.2, the geometry-induced phase transitions, in particular, the phase transitions in charged systems, are presented. Additionally, the macroscopic derivation of the Kelvin equation is presented in this section.

3.1 First-order demixing transition in binary mixtures

In this thesis, I am interested in a mixture of IL and neutral solvent, which can phase separate below its upper critical point [116]. Phase separation processes in a mixture are often studied in terms of the grand thermodynamic potential given by

$$\Omega = \mathcal{U} - TS - \sum_i \mu_i N_i \tag{3.1}$$

where $\mathcal{U}$ is the internal energy, T is the temperature, S the entropy, μ_i, and N_i are the chemical potential and the number of particles of the specie i, respectively. When several chemical species are present in a mixture, the chemical potential of each species is defined as

$$\mu_i(T, V, N) = \left(\frac{\partial F}{\partial N_i}\right)_{T,V,N_{i\neq j}} \tag{3.2}$$

where F is the Helmholtz free energy. The grand thermodynamic potential $\Omega(T, V, \mu)$ is the Legendre transform of $F(T, V, N)$ where the natural variable N is replaced by μ.

The mixture of IL and solvent corresponds to a binary system and, in this case, Eq. (3.1) is re-written as follows

$$\Omega = \mathcal{U} - TS - \mu_n N - \Delta\mu N_{IL} \tag{3.3}$$

where $N = N_n + N_{IL}$ is fixed and $\Delta\mu = \mu_{IL} - \mu_n$. Likewise, $N_{IL} = N_+ + N_-$ and $N_{IL}/V = \rho$. In order to simplify the notation, we use μ as the chemical potential difference ($\mu = \mu_{IL} - \mu_n$) and $\rho = \rho_+ + \rho_-$ as the IL density.

Figure 3.1a is a schematic representation of the phase diagram in the chemical potential-temperature plane of the system under consideration. The coexistence line (at chemical potential μ_{sat}) ends at an upper critical point marked by a red circle. Additionally, Figure 3.2 is a schematic representation of the phase diagram in the concentration-temperature plane. Above the critical temperature T_c, the system is homogeneous at any temperature and bulk composition of IL. However, below T_c, the homogeneous IL-solvent mixture becomes unstable for a certain range of concentration. It will spontaneously phase-separate into two phases, one phase rich in IL and the other one rich in the solvent. These two phases coexist along a saturation composition curve, which terminates at a bulk critical point: (ρ_c, T_c), where ρ_c is the critical composition of IL. An example of an experimental phase diagram of an aqueous system of imidazolium-based ionic liquids taken from [117], is shown in Figure 3.1b.

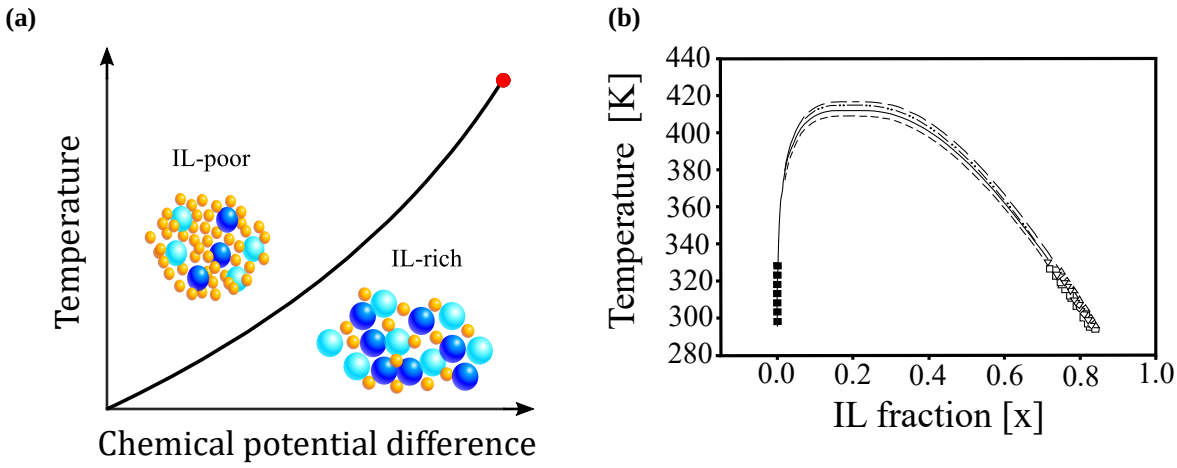

FIGURE 3.1 Scheme of an IL-solvent mixture phase diagram in the temperature-chemical potential plane, and experimental phase diagram of an aqueous system of imidazolium-based ionic liquids. **(a)** Scheme of an IL-solvent mixture phase diagram in the temperature-chemical potential plane. Below T_c (shown by a red circle), two phases coexist along a saturation chemical potential μ_{sat}. One phase is rich in IL, and the other phase is rich in the solvent. Light blue spheres denote cations, while blue spheres denote anions. Solvent molecules are denoted by yellow spheres. **(b)** Experimental phase diagram of an aqueous system of imidazolium-based ionic liquids. The picture was reproduced from [117].

At the critical point, a phase transition occurs due to the competition between the internal energy U that favors order, and the entropy S of the system, which benefits disorder, depending upon the temperature value, one of the terms dominates [118]. For $T \to \infty$, the entropic contribution of the thermodynamic potential dominates, meaning that molecules are arranged in a disordered phase. However, by decreasing temperature, the system starts ordering upon approaching an upper critical point implying that molecules can no longer move freely. As a consequence, droplets or correlated regions of the same type of molecules are formed provided that the interactions between like-molecules are strong enough. For $T \to T_c$, the size of the correlated regions, the so-called *correlation length* ξ, increases compared to the microscopic

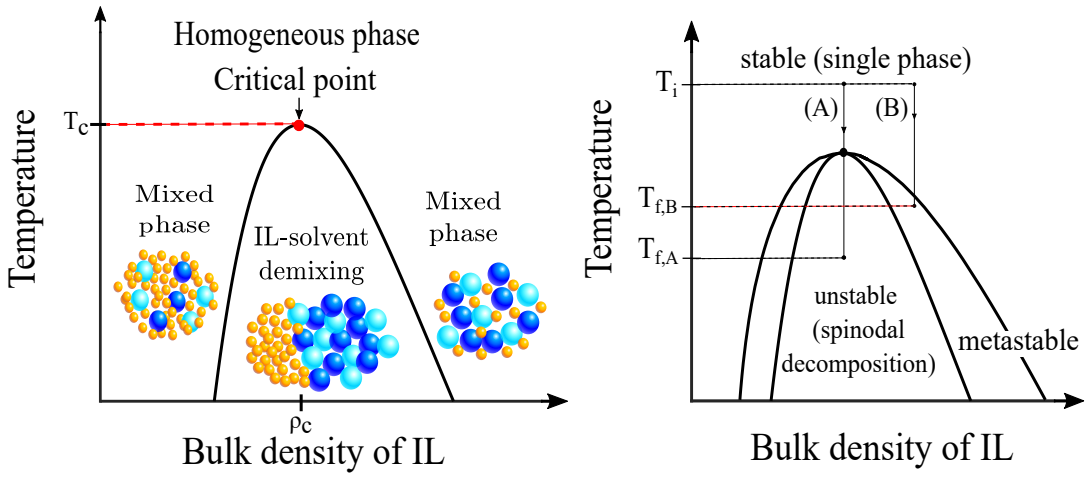

FIGURE 3.2 Scheme of an IL-solvent mixture phase diagram in the temperature-composition plane. At the left, light blue spheres denote cations while blue spheres denote anions. Solvent molecules are denoted by yellow spheres. Above the critical temperature T_c, the system is homogeneous for any temperature and bulk composition of IL. Below T_c, the mixture phase separates into one phase rich in IL and the other phase one rich in the solvent. The critical composition of IL is denoted by ρ_c. At the right, the binary mixture phase diagram showing critical (path A) and off-critical (path B) separations into the two-phase region from the one-phase region. Both paths start at T_i, however, critical separation ends at $T_{f,A}$ while off-critical separations ends at $T_{f,B}$.

lengths of the system, and at the critical point ($T = T_c$), ξ diverges.

The conventional classification of the phase transitions is given by the degree of singularity in the respective thermodynamic potential that describes the system. If the first-order derivative of the grand potential shows a discontinuity, then there is a first-order phase transition. On the other hand, if the second- or higher-order derivatives show a discontinuity or a divergence, the transition is called continuous, or second-order phase transition since the second- or higher-order derivative first displays a discontinuity or divergence.

At a first-order transition, an initially one-phase system separates into two different coexisting phases (*e.g.* vapor-liquid or liquid-liquid coexistence). Such phase separation is frequently studied by setting the system in a region of the phase diagram where the homogeneous state is stable. Then, a separation into two stable phases is induced by changing the temperature at a fixed concentration.

Consider the phase diagram shown in Figure 3.2-(right), a phase separation at higher temperatures, $T_i > T_c$, may be achieved either along the critical concentration line that crosses through the critical point (path A) or along off-critical paths (path B). Both paths end in a region bounded by the coexistence curve where there is an unstable region ($T_{f,A} < T_c$) and a metastable region ($T_{f,B} < T_c$). Either at $T_{f,A}$ or $T_{f,B}$, the binary mixture will spontaneously separate into stables IL-rich and IL-poor (solvent-rich) phases.

Let us consider now the phase diagram in Figure 3.3. In the one-phase region ($T_1 > T_c$), the grand thermodynamic potential function has a single minimum, while in the two-phase region ($T_2 < T_c$), it has two minima (*i.e.* the grand potential is bistable). In the coexisting phases, the intensive parameters: T, μ_i, and p are equal, and at equilibrium for fixed temperature and chemical potential, the grand potential in the two phases takes the same value. The system

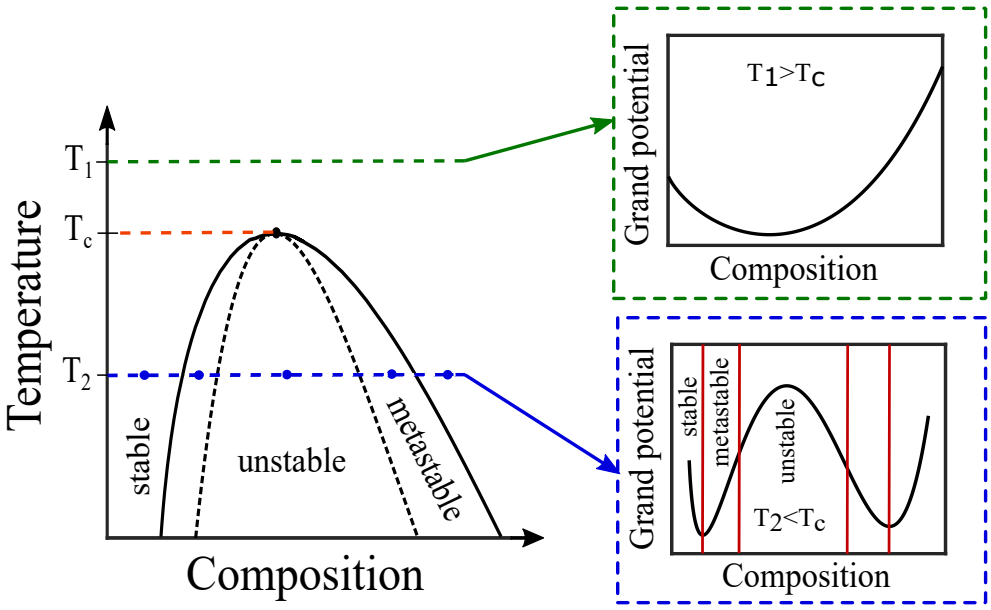

FIGURE 3.3 Scheme of grand potential as a function of composition at a fixed chemical potential. For a temperature in the one-phase region, $T_1 > T_c$ (where T_c is the critical temperature), the grand potential has one minimum. However, for a temperature in the two-phase region, $T_2 < T_c$, the grand potential has two minima representing the two phases: IL-rich and IL-poor phases.

becomes unstable under infinitesimal concentration fluctuations at the spinodal line (dashed line in Figure 3.3). For fixed μ, this line is determined by the condition

$$\frac{\partial^2 F}{\partial \rho^2} = \frac{\partial^2 \Omega}{\partial \rho^2} = 0 \tag{3.4}$$

recalling that $\mu = \mu_{IL} - \mu_n$ and $\rho = \rho_+ + \rho_-$ is the ion density. Likewise, the stability condition is

$$\frac{\partial^2 \Omega}{\partial \rho^2} \geq 0. \tag{3.5}$$

For a deeper understanding of the different shapes of the grand potential as a function of the order parameter [1], let us consider now a phase diagram in the chemical potential-temperature plane as shown in Figure 3.4a. The dashed lines denote the spinodals, whereas the solid line represents the bulk coexistence. The symbols mark the regions of interest inside the phase diagram.

At the spinodals, the grand potential has an inflection point. At the binodal line, marked by a triangle, both phases IL-rich and IL-poor coexist. Thus, the grand potential exhibits two minima of equal depth, meaning that both phases are equally stable (Figure 3.4b).

Inside the spinodal region (marked by a star and a circle in Figure 3.4a), the grand potential exhibits two minima, meaning that there are two phases, but just one of them is stable. At the left, marked by a star, the IL-poor phase is stable since the grand potential has a lower minimum for lower values of the order parameter (Figure 3.5a). At the right, marked by a circle, the IL-rich phase is stable since the grand potential exhibits a lower minimum for higher values of the

[1] In the case of binary mixtures, the order parameter usually is the composition, as shown in Figure 3.3

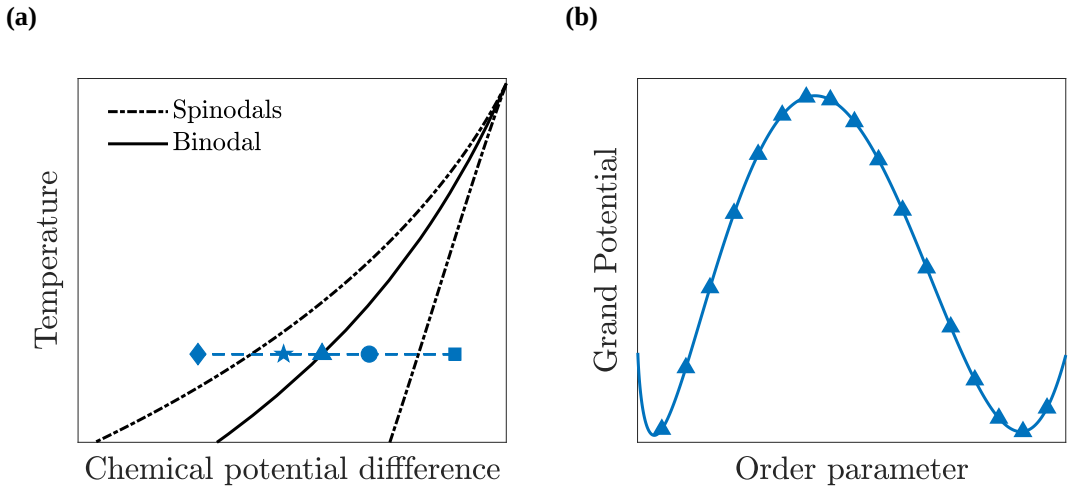

FIGURE 3.4 Scheme of a phase diagram in the temperature-chemical potential plane illustrating the spinodal and coexistence lines. (a) The symbols mark the regions of interest at which the grand potential as a function of the order parameter is plotted to study the system's behavior. **(b)** Grand potential as a function of the order parameter at the binodal line marked by a triangle in Figure 3.4a. At the binodal line, the IL-rich and IL-poor phases coexist; thus, the grand potential exhibits two minima of equal depth since both phases are stable.

order parameter (Figure 3.5b).

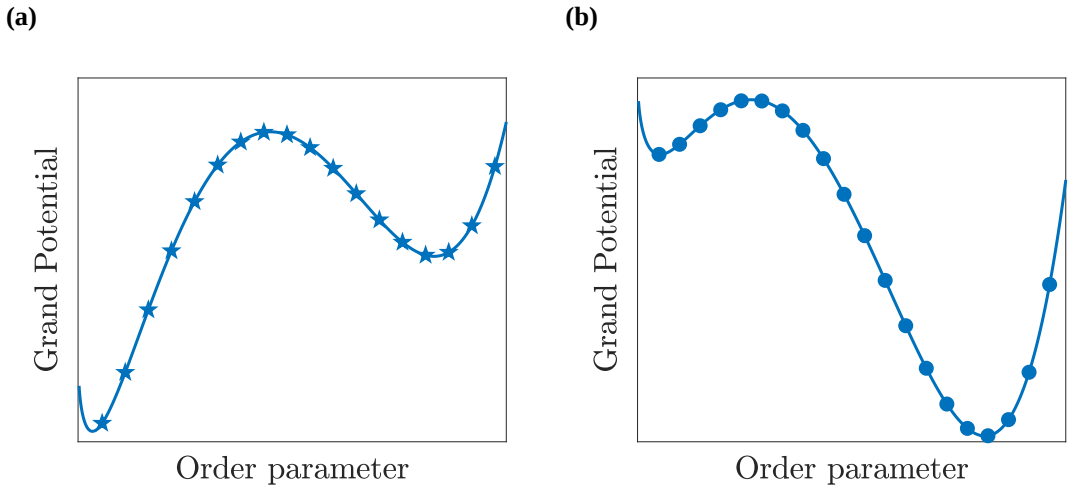

FIGURE 3.5 Grand potential as a function of the order parameter inside the spinodal region. (a) Grand potential as a function of the order parameter inside the region between the left spinodal and the coexistence line. In this region, the grand potential exhibits a lower minimum for lower values of the order parameter, meaning that the IL-poor phase is stable. This region is marked by a star in Figure 3.4a. **(b)** Grand potential as a function of the order parameter inside the region between the coexistence and the right spinodal line. In this region, the grand potential exhibits a lower minimum for higher values of the order parameter, meaning that the IL-rich phase is stable. This region is marked by a circle in Figure 3.4a.

Outside the spinodal region (marked by a diamond and a square in Figure 3.4a), the grand potential exhibits a single minimum, meaning that there is one phase. At the left, marked by a diamond, there is IL-poor phase, since the grand potential exhibits a global minimum at lower values of the order parameter (Figure 3.6a), whereas at the right, there is IL-rich phase (Fig-

ure 3.6b).

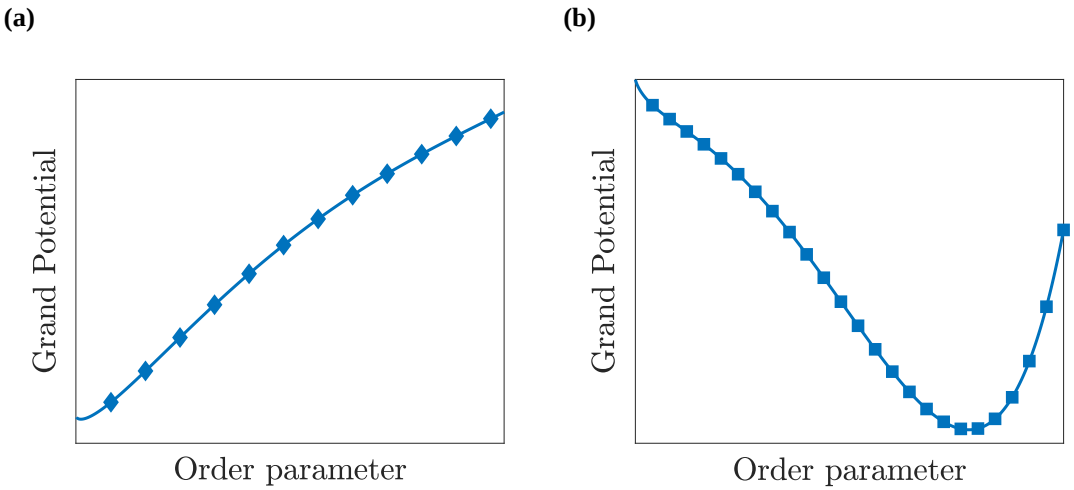

FIGURE 3.6 Grand potential as a function of the order parameter outside the spinodal region. (a) Grand potential as a function of the order parameter outside the spinodal region at the left. In this region, the grand potential exhibits a single minimum for lower values of the order parameter, meaning that there is only IL-poor phase. This region is marked by a diamond in Figure 3.4a. **(b)** Grand potential as a function of the order parameter outside the spinodal region at the right. In this region, the grand potential exhibits a single minimum for higher values of the order parameter, meaning that there is only IL-rich phase. This region is marked by a square in Figure 3.4a.

3.2 Geometry-induced phase transitions

Fluids under confinement can undergo a dramatic change in their equilibrium and dynamical properties. The behavior of a confined fluid is significantly different with respect to a bulk fluid, and this is directly related to the pore morphology, topology, and the magnitude of fluid–surface to fluid–fluid interactions. As a result, new phase transitions such as wetting, pre–wetting, capillary condensation, filling transitions in wedges, among others, may take place [119–122]. The fundamental understanding of these phase transitions involves finite-size effects and surface forces. Furthermore, when the pore size is of an order of magnitude comparable to the intermolecular forces, there will be a reduction of the number of nearest-neighbor molecules felt by the confined molecules. This effect leads to a shift in phase coexistence curves and a lowering of any critical points [5]. Such phenomenon is explained from the concept of *capillary criticality* that implies the existence of a temperature, T_{cc}, below the bulk critical temperature beyond which liquid-gas phase transition becomes reversible [122].

In the simplest case, gas-liquid condensation transitions are influenced by attractive walls. Let us consider a saturated gas in contact with a wall. A wetting transition occurs when a thick liquid layer condenses at the wall while the bulk fluid stays in the gas phase [31]. Depending on the nature of the surface forces, a drop placed on a substrate can either wet it or not and spreads over it to form a film. Correspondingly, a non-wetted surface, initially covered by a film, could be dewetted under an appropriate change of the parameters [4]. Additionally, pre–

wetting can also occur if the gas is unsaturated. Thus, there is a formation of a thin liquid layer at the wall [123].

If the confining geometry is cylindrical or slit-shaped pores, the most common example of confinement–induced phase transition is the capillary condensation phenomenon in which a gas at pressure $p < p_{sat}$ condenses to a liquid-like phase that fills the pore [31]. When the confining materials are charged then, electrocapillary phenomena take place. Electrocapillarity involves the thermodynamics of charged interfaces, and it is related to changes in the interfacial energy such as the electrode potential or to changes in the concentration of the electrolytes in solution [124]. Electrocapillarity research was started with the work of Gabriel Lippmann [125] who found that changes in voltage influence the capillary depression of mercury in contact with electrolyte solutions [126]. Nevertheless, it is important to note that electrocapillary phenomena are not only restricted to the study of the equilibrium properties of mercury/electrolyte solution interfaces but also refer to the study of other interfaces, for instance, interfaces between two immiscible electrolyte solutions [124].

In the presence of an electric field, oppositely charged ions are attracted to the interface between a conductive and a non-conductive (dielectric) material and exert an interfacial force. These induced forces are especially strong as the electric field becomes large. However, due to short-range attractions between ions of the same sign, and the entropy of mixing effect, co-ions are also attracted together with counterions. If the electric field is sufficiently strong, *electrowetting* occurs [126]. Additionally, in confinement, there are effects caused by the interplay of different length scales corresponding to particle sizes, ranges of intermolecular potentials, and dimensions of confinement [119, 127].

From a macroscopic treatment, consider a mixture of IL and solvent (see Figure 3.2-(left)) confined in an infinite capillary slit. In the limit of large slit width, w, the total grand potential of the confined phases is the sum of the bulk and surface contributions [31, 128]:

$$\Omega_{rich} = -p_{rich} A\, w + 2\sigma_{rich}(w,\mu)A \tag{3.6}$$

$$\Omega_{poor} = -p_{poor} A\, w + 2\sigma_{poor}(w,\mu)A \tag{3.7}$$

where p_{rich} is the pressure of the IL-rich phase and p_{poor} is the pressure of the IL-poor phase at the same chemical potential μ. Additionally, σ_{rich} and σ_{poor} are the surface excess grand potentials of the IL-rich and IL-poor phases, respectively, evaluated at μ_{sat} [31, 128, 129]. The coexistence of IL-rich and IL-poor phases occurs when $\Omega_{rich} = \Omega_{poor}$, then

$$p_{rich} - p_{poor} = \frac{2}{w}(\sigma_{rich} - \sigma_{poor}) \tag{3.8}$$

At constant temperature, $dp = \rho\, d\mu$, and by expanding $p_{rich}(\mu)$ and $p_{poor}(\mu)$ about p_{sat}, Eq. (3.8) can be written as

$$\mu - \mu_{sat} = \frac{2}{w}\frac{(\sigma_{rich} - \sigma_{poor})}{(\rho_{rich} - \rho_{poor})} \tag{3.9}$$

This treatment is valid under the assumption that the density profiles are almost constant in the slit [128], that is $\rho(z) \approx \rho_{rich}$ and $\rho(z) \approx \rho_{poor}$, where ρ_{rich}, ρ_{poor} are the density of the IL-rich and IL-poor phases, respectively.

Confinement shifts the location of the coexistence along a saturation chemical potential curve, μ_{sat}, to a capillary ionization curve that occurs along μ_{ci} and which ends at a capillary critical temperature. The phase boundary shift at which capillary ionization takes place satisfies the macroscopic Kelvin equation [121, 130]:

$$\mu_{ci} = \mu_{sat} + \frac{2\Delta\sigma}{w\Delta\rho} \tag{3.10}$$

Figure 3.7 shows the capillary ionization line obtained from the Kelvin equation (Eq. (3.10)). Note, it is shifted with respect to the bulk coexistence, μ_{sat}, shown in Figure 3.1a.

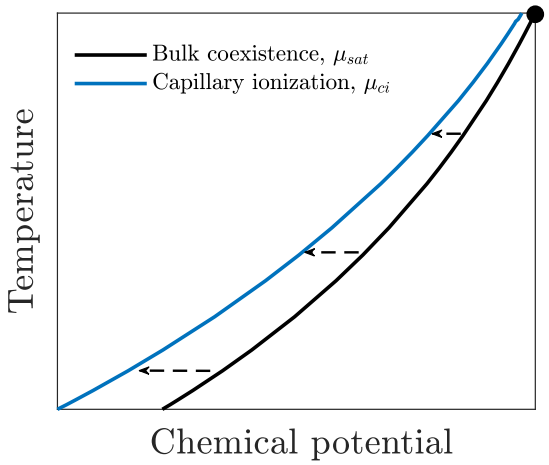

FIGURE 3.7 Capillary ionization of slit mesopores in the chemical potential-temperature plane. The black solid line denotes the bulk coexistence (at μ_{sat}) that ends at the critical point, while the solid blue line is the capillary ionization curve obtained from the Kelvin equation (Eq. (3.10)).

Chapter 4

Development of a Generic Model

In this chapter, the system under consideration is described, and a generic model to analyze its behavior is developed by combining the Poisson-Boltzmann and the mean-field theory for phase transitions in mixtures. Additionally, two approximations for describing the excluded-volume interactions are implemented: lattice-gas and Carnahan-Starling approximations. In Section 4.2, the phase diagram for the bulk system is presented. In Section 4.3, we derive the Euler-Lagrange equations that result from the minimization of the grand thermodynamic potential. Finally, in Section 4.4, the system's thermodynamic characteristics are obtained.

4.1 Construction of the Grand-potential functional

We consider a mixture of ionic liquid (IL) and neutral solvent, which can phase separate below its upper critical point. We are interested in the one-phase region close to demixing. Figure 4.1 shows the system under consideration. We assume that the mixture is in contact with two planar metallic electrodes separated by a distance w, and the electrostatic potential, U, is kept constant with respect to the bulk. Additionally, we consider that electrodes prefer ions or solvent molecules, meaning that the short-range (non-Coulombic) interactions between the ions/solvent and the surface are different. This preference is called *ionophilicty*, and it is denoted by h_s.

This system can be described by the following grand thermodynamic potential [98, 131]

$$\Omega[\rho_{\pm}, u]/A = \omega_{el} + \omega_{vdW} + \omega_s - Ts - \mu_i \int_0^w dz \rho_i(z), \tag{4.1}$$

where ω_{el}, ω_{vdW}, ω_s and s are the electrostatic energy, the internal energy associated with van der Waals-like dispersion (non-Coulombic) interactions, the energy associated with the pore walls, and the entropy (all per surface area), respectively; T is temperature, A is the surface area

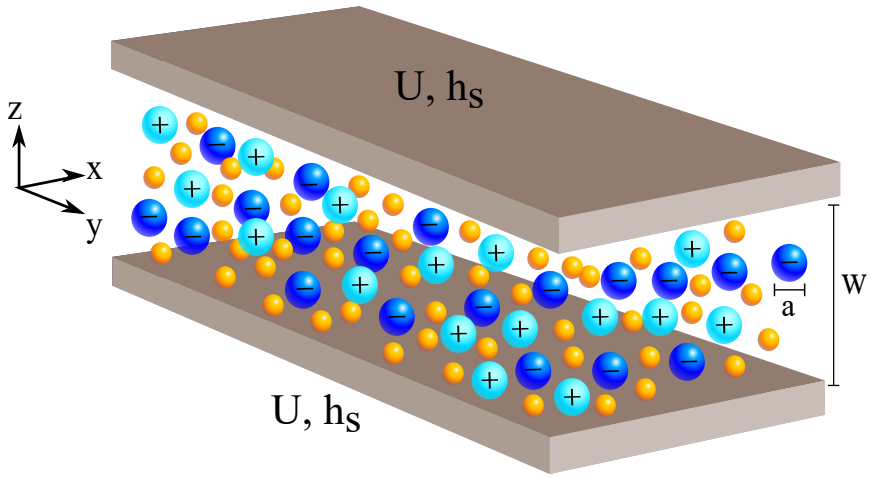

FIGURE 4.1 IL-solvent mixture in contact with a slit-shaped pore. The electrodes are separated by a distance w, and the electrostatic potential, U, applied at $z = 0$ and $z = w$ is kept constant with respect to the bulk. The ion diameter, a, is the same for cations (light blue spheres) and anions (blue spheres). Yellow spheres represent the solvent. The ionophilicity (or surface field) at $z = 0$ and $z = w$ is denoted by h_s and describes the electrode preference by ions or solvent.

of the electrode, μ_i is the chemical potential, and $\rho_i(z)$ is the local density of the *i*-th component, where $i = \{+, -, n\}$ denotes cations, anions and solvent, respectively.

The electrostatic energy, in k_BT units, is given by [73, 132–134]

$$\beta\,\omega_{el}[c(z), u(z)] = \int_0^w dz\Big[cu - \frac{1}{8\pi\lambda_B}\Big(\frac{\partial u}{\partial z}\Big)^2\Big] \tag{4.2}$$

where $\beta = 1/(k_BT)$, u is the electrostatic potential in k_BT/e units with k_B denoting the Boltzmann constant; $c = \rho_+ - \rho_-$ is the charge density per elementary charge e and $\lambda_B = \beta e^2/\epsilon_r$ is the Bjerrum length, where ϵ_r is the dielectric constant. It is well known that ϵ_r depends on temperature, particularly for polar solvents [135–137]. Nevertheless, we assume ϵ_r to be temperature-independent and note that its temperature variation should not affect the results qualitatively, as considered in [131] (see Appendix C). In addition, it is known that polarizability of solvent and ions may play an important role in the structure and properties of electrical double layers [97, 101, 132, 133, 138, 139]. To capture generic effects, we have decided to consider a position-independent dielectric constant, as in [73–76, 78, 79, 93, 97, 102, 139]. The change of ϵ_r close to the surface will affect the results quantitatively. However, it is reasonable to expect that the qualitative behavior will not be altered.

The term $\omega_{vdW} = \Omega_{vdW}/A$ describes the contribution from attractive non-Coulombic van der Waals-like interactions to the internal energy, which may lead to demixing of the IL and solvent, and it can be written as

$$\Omega_{vdW} = \frac{1}{2}\int d\mathbf{r}_1 \int d\mathbf{r}_2 \rho_i(\mathbf{r}_1) J_{ij}(\mathbf{r}_1 - \mathbf{r}_2)\rho_j(\mathbf{r}_2), \tag{4.3}$$

where $J_{ij}(\mathbf{r}_1 - \mathbf{r}_2)$ is the interaction between the species i, j at the positions $\mathbf{r}_1, \mathbf{r}_2$ respectively. We perform the coarse-graining procedure as in [133, 140], and assume that $J_{++} = J_{--} = J_{+-}$ and $J_{+n} = J_{-n}$. This assumption can be valid, provided that when the

phase separation is driven by the chemical difference between IL and neutral solvent, we can take into account only the effective interactions leading to phase separation. Thus, Eq. (4.3) simplifies to

$$\Omega_{vdW} = \frac{1}{2}\int d\mathbf{r}_1 \int d\mathbf{r}_2 \Big[J_{++}(r)\rho(\mathbf{r}_1)\rho(\mathbf{r}_2) + 2J_{+n}(r)\rho(\mathbf{r}_1)\rho_n(\mathbf{r}_2) + J_{nn}(r)\rho_n(\mathbf{r}_1)\rho_n(\mathbf{r}_2) \Big] \quad (4.4)$$

where $r = |\mathbf{r}_1 - \mathbf{r}_2|$, and $\rho(\mathbf{r}) = \rho_+(\mathbf{r}) + \rho_-(\mathbf{r})$ is the local density of the IL at position $\mathbf{r}$. Additionally, we neglect the density fluctuations (meaning that the fluid is incompressible) and assume fixed total density of the mixture

$$\rho_+(\mathbf{r}) + \rho_-(\mathbf{r}) + \rho_n(\mathbf{r}) = 1 \quad (4.5)$$

where $\rho_n(\mathbf{r})$ is the density of the neutral component in the mesoscopic region at $\mathbf{r}$. Inserting $\rho_n = 1 - \rho$ in Eq. (4.4) gives

$$\Omega_{vdW} = \frac{1}{2}\int d\mathbf{r}_1 \int d\mathbf{r}_2 \Big[J(r)\rho(\mathbf{r}_1)\rho(\mathbf{r}_2) + J_\mu(r)\rho(\mathbf{r}_1) \Big] \quad (4.6)$$

where $J(r) = J_{++}(r) - 2J_{+n}(r) + J_{nn}(r)$ represents the effective interactions leading to phase separation, and $J_\mu(r) = 2(J_{+n}(r) - J_{nn}(r))$. We assume that $\mu_+ = \mu_-$, then

$$\Omega_{vdW} - \sum_i \mu_i \int d\mathbf{r}\rho_i(\mathbf{r}) = \frac{1}{2}\int d\mathbf{r}_1 \int d\mathbf{r} J(r)\rho(\mathbf{r}_1)\rho(\mathbf{r}_1 + \mathbf{r}) - \mu \int d\mathbf{r}\rho(\mathbf{r}) \quad (4.7)$$

where μ is the difference between the chemical potentials of an IL and solvent given by

$$\mu = \mu_+ - \mu_n - \frac{1}{2}\int d\mathbf{r} J_\mu(r) \quad (4.8)$$

We have applied the approach used in [132, 133], which consists on implementing Taylor expansion of $\rho(\mathbf{r}_1 + \mathbf{r})$ in Eq. (4.7), around $\mathbf{r_1}$

$$\Omega_{vdW} - \sum_i \mu_i \int d\mathbf{r}\rho_i(r) = \frac{1}{2}\int d\mathbf{r}_1 \Big[\rho^2(\mathbf{r}_1)J_0 + \rho(\mathbf{r}_1)J_2 \frac{d^2\rho(\mathbf{r}_1)}{d\mathbf{r}_1^2} + ... \Big] - \mu \int d\mathbf{r}\rho(\mathbf{r}) \quad (4.9)$$

where $J_0 \approx \int d\mathbf{r} J(r)$ and $J_2 \approx \int d\mathbf{r} J(r) r^2/2$. Integration by parts of the second term in Eq. (4.9), leads to

$$\begin{aligned} \Big[\omega_{vdW} + \omega_s - \sum_i \mu_i \int dz \rho_i(z) \Big] &\approx K \Bigg\{ \int_0^w dz \left[\frac{\xi_0^2}{2} \left(\frac{\partial \rho}{\partial z} \right)^2 - \frac{1}{2}\rho^2 \right] \\ &+ \frac{\xi_0}{2}\rho_0^2 - h_s\rho_0 + \frac{\xi_0}{2}\rho_w^2 - h_s\rho_w \Bigg\} \\ &- \mu \int_0^w dz \rho(z) \end{aligned} \quad (4.10)$$

where

$$K = -J_0 = -\int d\mathbf{r} J(r) > 0 \tag{4.11}$$

measures the strength of the dispersion interactions, and

$$\xi_0^2 = \frac{1}{2}\frac{\int d\mathbf{r} J(r) r^2}{\int d\mathbf{r} J(r)} \tag{4.12}$$

describes the spatial extension of these interactions (ξ_0 is of the same order of magnitude as the molecular size a). In Eq. (4.10), we took into account that the interactions with the missing fluid neighbours beyond the system boundary should be subtracted (the first boundary term), and we included the direct short-range interactions of the fluid particles with the wall (the second boundary term).

$$\omega_s = -[h_s\rho(z=0) + h_s\rho(z=w)] = -[h_s\rho_0 + h_s\rho_w] \tag{4.13}$$

The electrode's ionophilicity is denoted by h_s and describes the preference of the electrode for ions or solvent; $h_s > 0$ means that the wall favors ions, and we assumed this preference to be the same for anions and cations.

Within the local density approximation, the entropy is

$$-Ts = -T\int_0^\infty dz s([\rho_i(z)]) = k_B T \int_0^\infty dz \left[\rho_+ \ln(a^3\rho_+) + \rho_- \ln(a^3\rho_-) + \beta f_{ex}(\rho)\right]. \tag{4.14}$$

The first two terms in Eq. (4.14) come from the entropy of mixing of ions, and the last term is the excess free energy associated with the excluded volume interactions. If the cations and anions are of comparable size, but the solvent molecules are much smaller, such that the solvent can be treated as a structureless continuum, it seems reasonable to use the Carnahan - Starling (CS) approximation [141] for the excluded volume interactions between the ions only, *i.e.*,

$$\beta f_{ex}^{CS}(\rho) = \rho\left(\frac{4\eta - 3\eta^2}{(1-\eta)^2} - 1\right), \tag{4.15}$$

where $\eta = \pi\rho a^3/6$ is the packing fraction of ions. However, if both ions and solvent are of comparable size, it might be more suitable to use the popular lattice-gas expression

$$\beta f_{ex}^{lg}(\rho) = (\rho_{tot} - \rho)\ln\left[a^3(\rho_{tot} - \rho)\right], \tag{4.16}$$

which arises from the solvent's ideal-gas entropy, $\beta f_{ex} = \rho_n \ln a^3\rho_n$, by assuming the local incompressibility conditions, $\rho_+(\mathbf{r}) + \rho_-(\mathbf{r}) + \rho_n(\mathbf{r}) = \rho_{tot}$ ($\rho_{tot} = a^{-3}$ for the lattice–gas model). Eq. (4.16) has been employed in a number of important studies, most notably by Bikerman [69], Wicke and Eigen [70, 72], Borukhov *et al.* [73], Kilic *et al.* [100] and Kornyshev [78].

In Eqs. (4.15) and (4.16), the cations and anions are assumed to be of the same size,*i.e.* ,

$a_- = a_+ = a$, whereas often $a_+ \neq a_-$ [142–144]. Gongadze [142] proposed an improved mean-field model of EDLs that accounts for such ion-size asymmetry and found that it leads to a pronounced decrease of the capacitance and to shape asymmetry of the capacitance-voltage curves (with respect to the potential of zero charge), which seems to be consistent with the experimental observations [87, 96]. These results suggest that the asymmetry in ion sizes may reduce the capacitance calculated in this work and bring asymmetry in the capacitance-voltage dependence, but the qualitative behavior due to proximity to demixing shall be captured already by a model featuring the same sizes of cations and anions.

Summing up, our final expression of the grand potential is [131]

$$\begin{aligned}\beta\,\Omega[\rho_\pm, u]/A = &\int_0^w dz \left[\rho_+ \ln(a^3\rho_+) + \rho_- \ln(a^3\rho_-) + \beta f_{ex}(\rho)\right] \\ &+ \int_0^w dz \left[cu - \frac{1}{8\pi\lambda_B}\left(\frac{\partial u}{\partial z}\right)^2\right] \\ &+ \beta K \left\{\int_0^w dz \left[\frac{\xi_0^2}{2}\left(\frac{\partial \rho}{\partial z}\right)^2 - \frac{1}{2}\rho^2\right] + \frac{\xi_0}{2}\rho_0^2 - h_s\rho_0 + \frac{\xi_0}{2}\rho_w^2 - h_s\rho_w\right\} \\ &- \beta\mu \int_0^w \rho dz\end{aligned} \tag{4.17}$$

4.2 Bulk system

In the absence of confinement surfaces, Eq. (4.17) simplifies to give the bulk system equation

$$\beta\Omega_b(\bar{\rho}_b)/V = -\beta K\frac{\bar{\rho}_b^2}{2} + \bar{\rho}_b \ln\left(\frac{\bar{\rho}_b}{2}\right) + \beta f_{ex}(\bar{\rho}_b) - \beta\mu\bar{\rho}_b. \tag{4.18}$$

where $V = wA$ is the volume, $\bar{\rho}_b = a^3\rho_b$ and ρ_b is the bulk ion density. The equilibrium condition, $\partial\Omega_b/\partial\bar{\rho}_b = 0$, leads to a non-linear equation, which we solved numerically. The solution reveals the existence of two phases, one enriched in ions called IL-rich phase ($\rho_b = \rho_{rich}$), and the other enriched in the solvent called IL-poor phase ($\rho_b = \rho_{poor}$). Figure 4.2 shows the phase diagrams obtained by implementing both CS and lattice-gas approximations. The solid lines denote the coexistence between IL-rich and IL-poor phases that occurs when $\Omega_b(\rho_{rich}) = \Omega_b(\rho_{poor})$, and is typical for IL-solvent mixtures [117, 145]. Additionally, there is a region of temperatures and IL densities where an IL-solvent mixture separates into the IL-poor and IL-rich phases. This region shrinks for increasing temperature and ends at a critical temperature T_c.

At the spinodal line, $\partial^2\Omega_b/\partial\rho_b^2 = 0$, the homogeneous IL-solvent mixture becomes unstable with respect to density fluctuations. Within our mean-field theory, the spinodal line is given by

$$\bar{T}_c(\bar{\rho}_b) = \alpha^{-1}(\bar{\rho}_b), \tag{4.19}$$

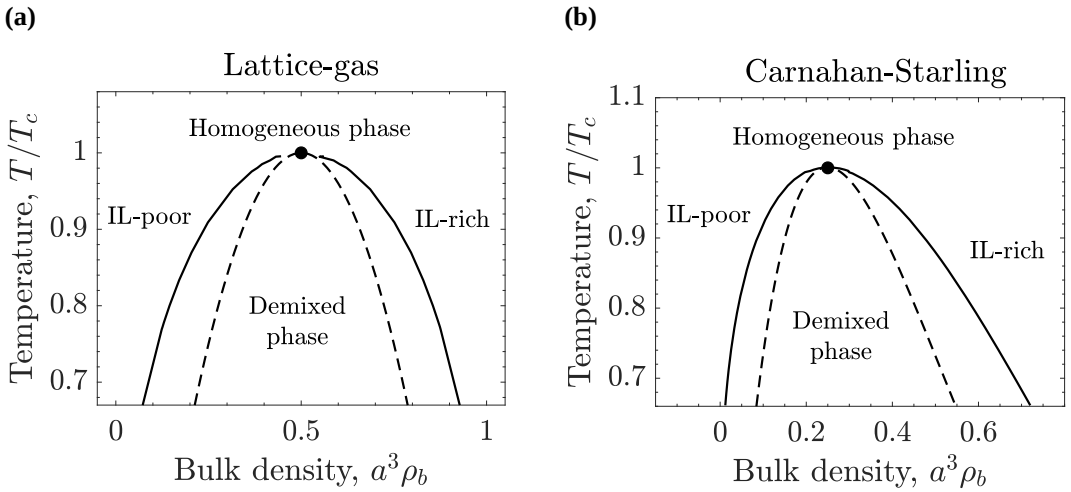

FIGURE 4.2 **Bulk phase diagrams of ionic liquid (IL)-solvent mixtures. (a)** Excluded volume given by the Carnahan-Starling approximation. **(b)** Excluded volume given by the lattice-gas approximation. The solid lines represent the first order phase transition between the homogeneous and IL-solvent demixed phases, and the dashed lines are the spinodal curves given by Eq. (4.19). The circles denote (upper) critical points. Temperature is expressed in terms of the critical temperature T_c.

where $\bar{T} = k_B T a^3/K$ is dimensionless temperature and

$$\alpha(\bar{\rho}_b) = \left[\left. \frac{\partial \mu_{ex}}{\partial \bar{\rho}} \right|_{\bar{\rho}=\bar{\rho}_b} + \bar{\rho}_b^{-1} \right]. \tag{4.20}$$

where $\mu_{ex} = \beta \partial f_{ex}/\partial \rho$. The spinodals are shown by dashed lines in Figure 4.2. The point on the spinodal that satisfies $d\bar{T}_c(\bar{\rho}_b)/d\bar{\rho}_b = 0$ corresponds to a critical point (solid circles in the same figure). For the CS and lattice-gas expressions, we found for the critical points $\bar{\rho}_c \approx 0.25$, $\bar{T}_c \approx 0.09$ and $\bar{\rho}_c \approx 0.5$, $\bar{T}_c \approx 0.25$, respectively. In addition, it is worth noting that the obtained phase diagrams are in good qualitative agreement with the experimental phase diagram shown in Figure 3.1b.

4.3 Euler-Lagrange equations

The equilibrium properties of the system are described by the minimum of Ω in Eq. (4.17). Minimization with respect to the electrostatic potential u gives

$$\lambda_D^2 \frac{d^2 u}{dz^2} = -c = (1 + \phi/\bar{\rho}_b) \tanh(u), \tag{4.21}$$

where $\lambda_D = (4\pi \rho_b \lambda_B)^{-1/2}$ is the Debye screening length in bulk electrolyte, ρ_b is the equilibrium ion density (in bulk), and $\phi = \bar{\rho} - \bar{\rho}_b$ is the order parameter. The boundary conditions are, $u(w) = u(0) = eU/k_B T_c$, where U is the applied voltage to a pore with respect to bulk electrolyte. Minimization with respect to the ion density, ρ, gives

$$\xi_0^2 \frac{d^2 \phi}{dz^2} + \phi = \bar{T} \left[\ln(1 + \phi/\bar{\rho}_b) - \ln(\cosh(u)) + \Delta\mu_{ex} \right], \tag{4.22}$$

where $\Delta\mu_{ex} = \mu_{ex} - \mu_{ex}^b$ with $\mu_{ex}^b = \mu_{ex}(z = \infty)$. The boundary conditions are $\xi_0\phi'(0) - \phi(0) + \bar{h_s} = 0$ and $\xi_0\phi'(w) + \phi(w) - \bar{h_s} = 0$, where $\bar{h_s} = a^3 h_s/\xi_0$.

4.4 Thermodynamic characteristics

In order to study and analyze the behavior of the ILs under confinement, we calculated some thermodynamic characteristics such as accumulated charge, stored energy, differential capacitance, amount of ions adsorbed into the pore, and the charging mechanisms. In this section, we derive these expressions, but the results are shown in Chapters 6-7 where we study two cases. In the first case (Chapter 6), the mixture of IL and solvent is in contact with a single surface ($w \to \infty$). In the second case (Chapter 7), the mixture of IL and solvent is confined by slit-shaped mesopore as it is schematically shown in Figure 4.1.

The charge accumulated in an EDL is [98, 131]

$$Q(u) = -\int_0^w c(z)\, dz \tag{4.23}$$

As it was presented in Section 2.3, the differential capacitance is given by Eq. (2.10). The energy stored in the surface is

$$E(U) = \int_0^U C(u)\, u\, du \tag{4.24}$$

Another important characteristic that gives us information about charging mechanisms inside the pore is the charging parameter, X_D, which is [146, 147]

$$X_D(u) = \frac{e}{C(u)}\frac{d\Gamma}{du} \tag{4.25}$$

where Γ is the amount of ions adsorbed in the pore [1] and is given by

$$\Gamma = \int_0^w (\rho(z) - \rho_b)\, dz \tag{4.26}$$

If $X_D(u) = 0$, the charging is due to swapping coions for counterions. However, if $X_D = 1$ there is counterion electrosorption (or simply adsorption), and $X_D > 1$ implies that both counterions and coions are adsorbed in the pore; a negative value of the charging parameter means desorption of ions from slit pore [98, 131].

However, when the mixture of IL and solvent is confined by a slit-shaped mesopore, capillary ionization transition can be induced by applying a voltage to a mesopore. This transition, occurring at $u = u_{ci}$, is accompanied by a sudden increase of the accumulated charge in the pore, which has important consequences for the differential capacitance and the stored energy. To analyze charging in this case, the charge accumulated in the slit pore is written as

$$Q(u) = Q_{poor}(u) + [Q_{rich}(u) - Q_{poor}(u)]\ \theta(u - u_{ci}) \tag{4.27}$$

[1] Γ also could be understood as the surface coverage by the ionic liquid.

where $Q_{poor}(u)$ and $Q_{rich}(u)$ are the accumulated charges in the IL-poor and IL-rich phases, respectively, and $\theta(x)$ is the Heaviside step function equal unity for $x > 0$ and zero otherwise. Then,

$$Q(u) = Q_{poor}(u) = -\int_0^w c_{poor}(z)dz \qquad \text{if } u < u_{ci} \tag{4.28}$$

$$Q(u) = Q_{rich}(u) = -\int_0^w c_{rich}(z)dz \qquad \text{if } u > u_{ci} \tag{4.29}$$

and the jump of the accumulated charge at the transition voltage u_{ci}, is given by

$$\Delta Q_{ci} = Q_{rich}(u_{ci}) - Q_{poor}(u_{ci}) \tag{4.30}$$

By inserting Eq. (4.28) and Eq. (4.29) in Eq. (2.10), one can write the capacitance as follows

$$C(u) = \frac{dQ_{poor}}{du}\theta(u_{ci} - u) + \frac{dQ_{rich}}{du}\theta(u - u_{ci}) + (Q_{rich} - Q_{poor})\,\delta(u - u_{ci}) \tag{4.31}$$

where $\delta(x)$ is the Dirac delta-function. Then,

$$C_{poor}(u) = \frac{dQ_{poor}}{du} \qquad \text{if } u < u_{ci} \tag{4.32}$$

$$C_{rich}(u) = \frac{dQ_{rich}}{du} \qquad \text{if } u > u_{ci} \tag{4.33}$$

where $C_{poor}(u)$ and $C_{rich}(u)$ are the capacitance in the IL-poor and IL-rich phases, respectively. At the capillary transition, the capacitance diverges, and its expression is given by

$$C(u_{ci}) = C_{poor}(u_{ci}) + \Delta Q_{ci}\delta(u - u_{ci}) \tag{4.34}$$

Replacing Eq. (4.31) into Eq. (4.24), we obtain the energy stored in a pore

$$E(U) = \int_0^U \frac{dQ}{du}u\,du = \int_0^U \frac{dQ_{poor}}{du}(1 - \theta(u - u_{ci}))u\,du + \int_0^U \frac{dQ_{rich}}{du}\theta(u - u_{ci})u\,du + \int_0^U (Q_{rich} - Q_{poor})\,\delta(u - u_{ci})u\,du \tag{4.35}$$

Recalling the Dirac delta-function properties, from the last term in Eq. (4.35), we obtain $(Q_{rich} - Q_{poor})u_{ci}$, and finally have

$$E_{poor}(U) = \int_0^U \frac{dQ_{poor}}{du}u\,du \qquad \text{if } U < u_{ci} \tag{4.36}$$

$$E_{rich}(U) = \int_0^{u_{ci}} \frac{dQ_{poor}}{du}u\,du + \int_{u_{ci}}^U \frac{dQ_{rich}}{du}\,u\,du + (Q_{rich} - Q_{poor})\,u_{ci} \quad \text{if } U > u_{ci} \tag{4.37}$$

Therefore, the stored energy acquires an additional contribution at the transition, $\Delta E_{ci} = u_{ci}\Delta Q_{ci}$.

Chapter 5

Analytical and Numerical Solution Approaches

In this chapter, we propose analytical and numerical approaches to solve the model developed in the previous chapter. Section 5.1 presents the analytical method, highlighting that the proposed solution only applies to the single-surface system. In Section 5.2, the numerical approach is developed for the slit-shaped mesopore system while the single-surface system is solved by implementing the `bvp4c` *routine in MATLAB® software .*

Recalling the Euler-Lagrange equations presented in Section 4.3, the model to be solved is

$$\lambda_D^2 \frac{d^2u}{dz^2} = -c = (1+\phi/\bar{\rho}_b)\tanh(u) \tag{5.1}$$

$$\xi_0^2 \frac{d^2\phi}{dz^2} + \phi = \bar{T}\left[\ln(1+\phi/\bar{\rho}_b) - \ln(\cosh(u)) + \Delta\mu_{ex}\right] \tag{5.2}$$

In the case of a single surface, the electrostatic potential is subjected to the boundary conditions given by Eqs. (5.3)-(5.4). On the other hand, in the slit-shaped mesopore system, the boundary conditions for the electrostatic potential are given by Eqs. (5.5)-(5.6).

$$u(0) = eU/k_BT_c \tag{5.3}$$

$$u(\infty) = 0 \tag{5.4}$$

$$u(0) = \pm eU/k_BT_c \tag{5.5}$$

$$u(w) = eU/k_BT_c \tag{5.6}$$

where U is the applied voltage at an electrode with respect to bulk and the signs $\pm$ correspond to the cases of electrodes equally and oppositely charged that are studied in Chapter 7.

Likewise, the order parameter, ϕ is subjected to Eqs. (5.7)-(5.8) for a single surface, and subjected to Eqs. (5.9)-(5.10) for a slit mesopore.

$$\xi_0\phi'(0) - \phi(0) + \bar{h_s} = 0 \quad (5.7) \qquad \xi_0\phi'(0) - \phi(0) + \bar{h_s} = 0 \quad (5.9)$$

$$\phi(\infty) = 0 \quad (5.8) \qquad \xi_0\phi'(w) + \phi(w) - \bar{h_s} = 0 \quad (5.10)$$

where the ionophilicity is $\bar{h_s} = a^3 h_s/\xi_0$. For the system consisting of a single surface, we have proposed both, an analytical (Section 5.1) and numerical (Section 5.2) approach to solve Eqs. (5.1) and (5.2) subject to their respective boundary conditions. However, in the case of the slit-shaped mesopore system, only the proposed numerical solution applies.

5.1 Analytical solution

For the system composed of a mixture of IL and solvent in contact with a single surface, an approximate analytical solution is obtained for weak surface potentials, eU/k_BT_c, and ionophilicities, $\bar{h_s}$. For this purpose, we have used the standard perturbation analysis in which we assumed $u = u_0 + \varepsilon u_1 + \varepsilon^2 u_2 + ...$ and $\phi = \phi_0 + \varepsilon\phi_1 + \varepsilon^2\phi_2 + ...$, where ε is a small parameter. In the first-order approximation, we obtained the following equations

$$\frac{d^2u_1}{dz^2} = \lambda_D^{-2} u_1(z) \quad (5.11)$$

and

$$\frac{d^2\phi_1}{dz^2} = \xi^{-2}\phi_1(z), \quad (5.12)$$

where

$$\xi = \xi_0\left(\frac{\bar{T}}{\bar{T}_c(\bar{\rho}_b)} - 1\right)^{-1/2} \quad (5.13)$$

is the correlation length and $\bar{T}_c$ is given by Eq. (4.19). The solutions to Eqs. (5.11) and (5.12) are

$$u_1(z) = \frac{eU}{k_BT_c}\exp(-z/\lambda_D) \quad (5.14)$$

and

$$\phi_1(z) = \frac{\bar{h_s}}{\xi_0/\xi + 1}\exp(-z/\xi) \quad (5.15)$$

From Eqs. (5.14) and (5.15) one can expect that, in the first-order approximation, the electrostatic potential u and the order parameter ϕ are fully decoupled, meaning that the behavior

of u is determined entirely by the Debye screening length, λ_D, as in the classical Debye-Hückel theory (Section 2.1.1), while the decay of ϕ is determined by the correlation length, ξ.

In the second order perturbation, we obtained

$$\frac{d^2u_2}{dz^2} = \lambda_D^{-2}u_2 + \frac{\lambda_D^{-2}}{\bar{\rho}_b}\phi_1 u_1 \tag{5.16}$$

and

$$\frac{d^2\phi_2}{dz^2} = \xi^{-2}\phi_2 + \frac{\bar{T}}{2\,\xi_0^2\,\bar{\rho}_b^2}\left[A(\bar{\rho}_b)\phi_1^2 - \bar{\rho}_b^2 u_1^2\right], \tag{5.17}$$

where

$$A(\bar{\rho}_b) = \bar{\rho}_b^2\left.\frac{\partial^2\bar{\mu}_{ex}}{\partial\bar{\rho}^2}\right|_{\bar{\rho}=\bar{\rho}_b} - 1. \tag{5.18}$$

It is worth noting that $A(\bar{\rho}_b = \bar{\rho}_c) = 0$, where $\bar{\rho}_c$ is the critical density. Thus, in the second-order, the electrostatic potential u and the order parameter ϕ become coupled. This coupling determines the highly non-linear behavior of the system as it approaches demixing. The solutions to Eqs. (5.17) and (5.16) are presented in Appendix A.

Additionally, the differential capacitance can be computed by plugging the electrostatic potential, u, obtained by the perturbation expansion, into Eq. (4.23) and (2.10), then

$$C = C_0 + C_2\left(\frac{eU}{k_BT_c}\right)^2 + ..., \tag{5.19}$$

where

$$C_0 = C_D\left[1 + \frac{\bar{h_s}\,\xi/\lambda_D}{(1+\xi_0/\xi)(2\xi/\lambda_D+1)} + O(\bar{h_s}^2)\right] \tag{5.20}$$

and

$$C_2 = \frac{C_D}{4}\left[\frac{3(4\xi/\lambda_D + \xi/\xi_0 + 1)\left[(\xi/\xi_0)^2+1\right]}{2(\xi/\xi_0+1)(2\xi/\lambda_D+1)^2\bar{\rho}_b\;\alpha(\bar{\rho}_b)} - 1\right] + O(\bar{h_s}), \tag{5.21}$$

where $C_D = (a/\lambda_D)C_H$ is the Debye capacitance and $C_H = \epsilon_r/4\pi a$ the Helmholtz capacitance.

5.2 Numerical solution

For the single-surface system, the EL equations (Eqs. (5.1)-(5.2) subjected to Eqs. (5.3)-(5.4) and (5.7)-(5.4)-(5.8)) have been solved by implementing `bvp4c` routine in MATLAB® software. However, when the slit-shaped mesopore is considered, the solution becomes numerically unstable.

In order to avoid those numerical problems and obtain a more stable solution when varying parameters, we can solve the system by implementing a finite differences (FD) scheme in which we have control over the stability method. For this purpose, Eqs. (5.1)-(5.2) can be expressed as a reaction-diffusion system that takes the form of semi-linear parabolic partial differential equations as follows:

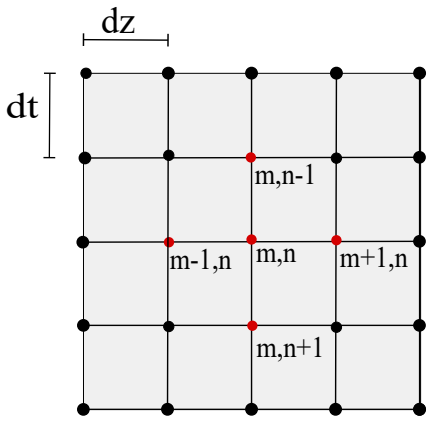

FIGURE 5.1 Finite difference discretization grid. Grid scheme where n represents time nodes and m spatial nodes. The separation between nodes are dz and dt for space and time respectively.

$$\partial_t q = D\,\partial_{zz}\,q + R(q), \tag{5.22}$$

where $q(z,t)$ corresponds to the unknown function, D is the diffusion coefficient, and R accounts for the generation term. Then, by inserting a first order time derivative, we can write the set of differential equations as follows:

$$\partial_t u = -\lambda_D^2 \partial_{zz} u + \left(1 + \frac{\phi}{\bar{\rho}_b}\right) \tanh(u) \tag{5.23}$$

$$\partial_t \phi = -\xi_0^2\,\partial_{zz}\phi - \phi + \bar{T}\left[\ln\left(1 + \frac{\phi}{\bar{\rho}_b}\right) - \ln(\cosh(u)) + \Delta\mu_{ex}\right] \tag{5.24}$$

We intend to find the steady state solution which corresponds to the solution of the original set of equations. Thus, we use a finite differences scheme that is forwarded in time and centered in space.

By implementing a finite difference scheme forwarded in time and centered in space as shown in Figure 5.1, we write Eqs. (5.23)-(5.24) in a discrete form:

$$u_m^{n+1} = u_m^n + D_u(u_{m+2}^n - 2\,u_{m+1}^n + u_m^n) + \Delta t\, R_u \tag{5.25}$$

$$\phi_m^{n+1} = \phi_m^n + D_\phi(\phi_{m+2}^n - 2\,\phi_{m+1}^n + \phi_m^n) + \Delta t\, R_\phi \tag{5.26}$$

where the diffusion coefficients, D_u and D_ϕ, are given by

$$D_u = -\frac{\Delta t\,\lambda_D^2}{\Delta z^2} \tag{5.27}$$

$$D_\phi = -\frac{\Delta t\,\xi_0^2}{\Delta z^2} \tag{5.28}$$

and Δt and Δz are the temporal and spatial discretization steps. The generation terms, R_u and

R_ϕ, are:

$$R_u = \left(1 + \frac{\phi_m^n}{\bar{\rho}_b}\right) \tanh(u_m^n) \tag{5.29}$$

$$R_\phi = -\phi_m^n + \bar{T}\left[\ln\left(1 + \frac{\phi_m^n}{\bar{\rho}_b}\right) - \ln(\cosh(u_m^n)) + \Delta\mu_{ex}\right] \tag{5.30}$$

5.2.1 Boundary conditions

The boundary conditions for ϕ are

$$\xi_0\,\phi'(0) - \phi(0) + \bar{h}_s = 0 \tag{5.31}$$

$$\xi_0\,\phi'(w) + \phi(w) - \bar{h}_s = 0 \tag{5.32}$$

Introducing the temporary derivative and expressing Eqs. (5.31)-(5.32) in a discrete form gives

$$\xi_0\left(\frac{\phi_2^n - \phi_1^n}{\Delta z}\right) - \phi_1^n + \bar{h}_s = \frac{\phi_1^{n+1} - \phi_1^n}{\Delta t} \tag{5.33}$$

$$\xi_0\left(\frac{\phi_w^n - \phi_{w-1}^n}{\Delta z}\right) + \phi_w^n - \bar{h}_s = \frac{\phi_w^{n+1} - \phi_w^n}{\Delta t} \tag{5.34}$$

Then, solving for the node forwarded in time, we have

$$\phi_1^{n+1} = \phi_1^n + \Delta t\left[\xi_0\left(\frac{\phi_2^n - \phi_1^n}{\Delta z}\right) - \phi_1^n + \bar{h}_s\right] \tag{5.35}$$

$$\phi_w^{n+1} = \phi_w^n + \Delta t\left[\xi_0\left(\frac{\phi_w^n - \phi_{w-1}^n}{\Delta z}\right) + \phi_w^n - \bar{h}_s\right] \tag{5.36}$$

Likewise, the boundary conditions for the electrostatic potential, u, are

$$u(0) - eU/k_BT_c = 0 \tag{5.37}$$

$$u(w) - eU/k_BT_c = 0 \tag{5.38}$$

Since there are no spatial derivatives, then

$$u_1^{n+1} = u_w^{n+1} = eU/k_BT_c. \tag{5.39}$$

5.2.2 Solution stability

For the model (Eqs. (5.1)-(5.2)) to be stable, the coefficients D_u and D_ϕ must fulfill [148]:

$$D_u \leq 0.25 \tag{5.40}$$

$$D_\phi \leq 0.25$$

The values of Δt and Δz have been chosen in such a way that the stability condition is preserved.

Chapter 6

Electrical Double Layers Close to Ionic Liquid–Solvent Demixing

In this chapter, we study an IL-solvent mixture in contact with a planar metallic electrode close to demixing. We consider the Lattice-gas and Carnahan-Starling approximations to describe the excluded-volume interactions. In Section 6.1, we present the charge density and ion density profiles as well as the differential capacitance calculated from the analytical solution of the model. These results are compared with those obtained by the full numerical solution. Finally, in Section 6.2, we present the thermodynamic characteristics of the system under consideration calculated from the numerical solution presented in Chapter 5.

We consider a mixture of ionic liquid and neutral solvent, which is in contact with a planar metallic electrode, and the electrostatic potential, U, is kept constant with respect to the bulk as shown in Figure 6.1. Our interest is in the one-phase region just above demixing.

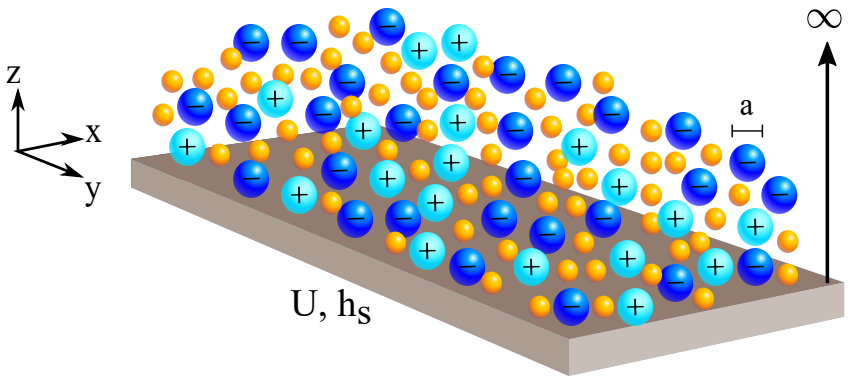

FIGURE 6.1 IL-solvent mixture in contact with a planar metallic electrode. The electrostatic potential, U, applied at $z = 0$ is kept constant with respect to the bulk. The ion diameter, a, is the same for cations (light blue spheres) and anions (blue spheres). Yellow spheres represent the solvent. The ionophilicity (or surface field) at $z = 0$ is denoted by h_s and describes the electrode preference for ions or solvent.

6.1 Analytical results

First, we analyze the results obtained from the analytical solution based on the perturbation expansion approach developed in Section 5.1, and compare them with the numerical solution to Eqs. (5.1)-(5.2), subjected to the boundary conditions given by Eqs. (5.3)-(5.4) for u and Eqs. (5.7)-(5.8) for ϕ. Figure 6.2 shows the charge density and ion density profiles by considering the lattice-gas and Carnahan-Starling approximations for the excluded volume interactions. Solid lines denote the numerical solution, whereas the dashed lines correspond to the second-order analytical solution. Regarding the ion density, ρ, analytic and numerical solutions differ significantly for increasing the applied potential. However, for the charge density, the perturbation expansion provides a relatively good approximation, and the solutions agree even for higher potentials.

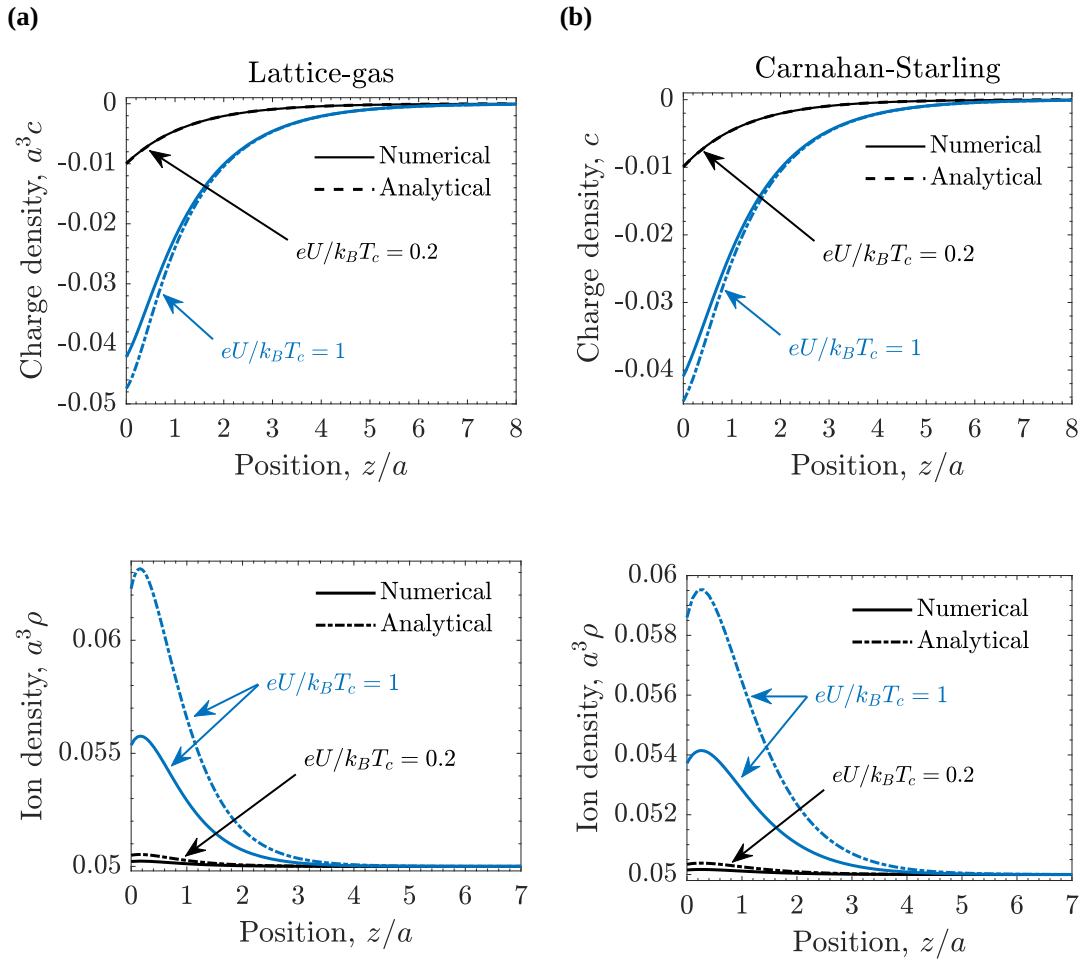

FIGURE 6.2 Density profiles comparing analytical and numerical solutions for the lattice-gas and Carnahan-Starling approximations. (**a**) Charge density (top) and ion density (bottom) profiles for the Lattice-gas approximation. (**b**) Charge density (top) and ion density (bottom) profiles for the Carnahan-Starling (CS) approximation. The dashed and solid lines correspond to the analytical and numerical solutions, respectively. The profiles were obtained at the applied potentials, eU/k_BT_c, as indicated on the plots, for ionophilicity $a^3h_s/\xi_0 = 0$, temperature $T/T_c = 1.5$, and bulk density $a^3\rho_b = 0.05$.

Recalling Eq. (5.19), the analytical differential capacitance is given by

$$C = C_0 + C_2\left(\frac{eU}{k_B T_c}\right)^2 + ... \tag{6.1}$$

where the coefficients C_0 and C_2 are given by Eqs. (5.20) and (5.21), respectively. The sign of C_2 describes the shape of the capacitance at low potentials. A positive C_2 corresponds to the so-called camel shape that exhibits a minimum at zero potential $U = 0$. A negative C_2 means a maximum at $U = 0$ and is often associated with the bell-shaped capacitance [78]. Such capacitance shapes have been extensively studied in the literature [78,79,87,93,94,97,101,139, 149, 150].

By monitoring the change of the sign of the coefficient C_2, it is possible to locate the transition between camel to bell-shaped capacitance. To do so from the analytical solution, let us neglect the dispersion interactions (that is $K = 0$) in Eq. (4.17) then, Eq. (5.20) becomes

$$C_0 = C_D, \tag{6.2}$$

and (5.21) reduces to

$$C_2 = \frac{C_D}{4}\left(\frac{3}{2\bar{\rho}_b\,\alpha(\bar{\rho}_b)} - 1\right) \tag{6.3}$$

Therefore, for $K = 0$, the sign of C_2, and thus the capacitance shape, depends solely on the IL density. For the lattice–gas model, combining Eq. (4.16) and Eq. (6.3) gives

$$C_2 = \frac{C_D}{4}\left(1 - 3\bar{\rho}_b\right) \tag{6.4}$$

which changes sign at $\rho_b^{lg} = 1/3$, meaning a transformation between the bell and camel shapes at ρ_b^{lg}, as first pointed out by Kornyshev [78]. For the CS approximation (Eq. (4.15)), it is obtained

$$C_2 = \frac{C_D}{4}\left[\frac{3(1-\eta_b)^4}{2(1+4\eta_b+4\eta_b^2-4\eta_b^3+\eta_b^4)} - 1\right] \tag{6.5}$$

where $\eta_b = a^3\pi\rho_b/6$. After solving the equation $C_2 = 0$ numerically, we obtained the transition between the camel and bell shapes at $\rho_b^{CS} \approx 0.098$. It is worth noting that this value is significantly lower than $\rho_b^{lg} = 1/3$ predicted by the lattice-gas model. This is similar to the critical density, which is also higher for the lattice-gas model (see Figure 4.2).

On the other hand, when dispersion interactions are considered ($K \neq 0$), Eq. (5.21) includes temperature dependence and becomes complex. Thus, we have solved it numerically by using `bvp4c` routine in MATLAB® $2017a$ software. Figures 6.3a and 6.3b show the diagrams for each excluded-volume approximation with the transition lines separating the regions of positive and negative curvatures in the low voltage capacitance. The examples of the capacitance shapes are presented in Figures 6.3c and 6.3d for the parameters shown by colored symbols in Figures 6.3a and 6.3b. The capacitance curves demonstrate that our analytical solutions are valid only in the vicinity of $u = 0$. The full numerical solution is needed to describe the capacitance behavior

properly.

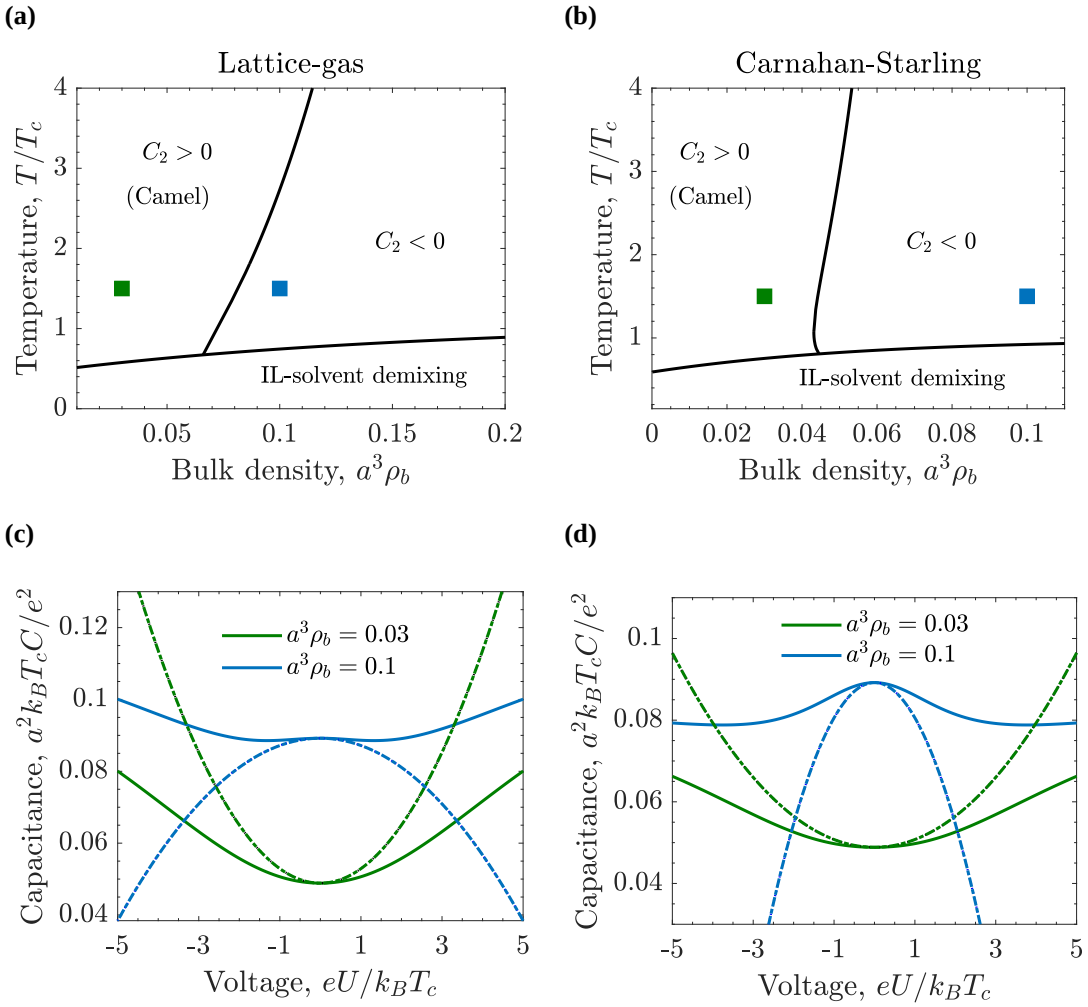

FIGURE 6.3 Differential capacitance comparing analytical and numerical solutions for the lattice-gas and Carnahan-Starling approximations. (a) Capacitance diagram showing the region of positive and negative sign of coefficient C_2 in the low-voltage capacitance (see Eq. (5.21)) for the Lattice-gas (lg) approximation (Eq. (4.16)). **(b)** Capacitance diagram showing the region of positive and negative sign of coefficient C_2 in the low-voltage capacitance (see Eq. (5.21)) for the Carnahan-Starling (CS) approximation (Eq. (4.15)). **(c)** Example of capacitance in the low-voltage region for the CS aproximation. **(d)** Example of capacitance in the low-voltage region for the lg approximation. The capacitance curves were obtained at temperature $T/T_c = 1.5$ and two different bulk densities marked by colored square symbols in their respective capacitance diagram. Dashed lines denote the analytical approximation, whereas the solid lines were obtained by solving Eqs. (4.21)-(4.22) numerically (see Section 5.2). In all the plots, the ionophilicity $a^3 h_s/\xi_0 = 0$, and for typical values of the ion diameter $a = 0.7\,\mathrm{nm}$ and room temperature for T_c, the various units are: thermal voltage $e/k_B T_c \approx 26\,\mathrm{mV}$ for voltage, thermal electric capacitance $e^2/(k_B T_c a^2) \approx 620\,\mu\mathrm{F\,cm^{-2}}$ for capacitance.

6.2 Numerical results

The full numerical solution of Eqs. (4.21) and (4.22) allows us to explore and analyze the system's behavior in a wide range of voltages, temperatures, and densities. First, in order to calculate the differential capacitance (according to Eq. (2.10)), we fix the voltage and the

temperature above demixing and vary the bulk density. Figure 6.4 is a phase diagram in the temperature-bulk density plane. The colored symbols mark three different bulk densities at a fixed temperature above the demixing region, $T/T_c = 1.2$.

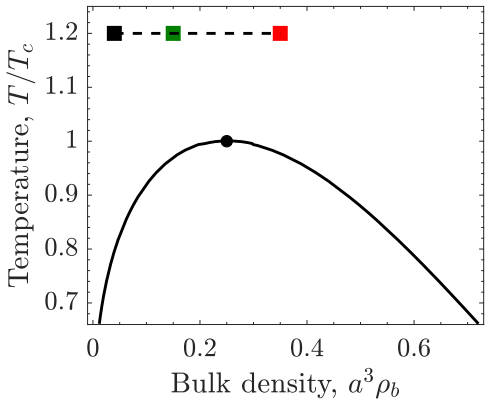

FIGURE 6.4 Phase diagram in the temperature-bulk density plane illustrating the region at which numerical results are obtained. Initially, we are interested in the region above demixing ($T/T_c > T_c$) to analyze the system's behavior when the bulk density is varied.

Figures 6.5a and 6.5b show that, for both approximations CS and lg, the differential capacitance can have multiple peaks as a function of the applied potential U, depending on the IL concentration ρ_b. As it was presented in Section 2.3.1, the case of low ion concentrations has been extensively studied, and consistently, for $a^3\rho_b$ the capacitance curve exhibits a minimum at the PZC and two symmetric maxima. In other words, at low concentrations, the capacitance displays a camel-like shape. Likewise, at higher concentrations, we obtained the well-studied bell-shaped capacitance that exhibits a single maximum at the PZC and decreases monotonically as the voltage increases. Interestingly, our calculations revealed that the capacitance could exhibit three peaks at intermediate IL concentrations. The first peak is at the PZC, which is characteristic of high densities, whereas the two other peaks at the positive and negative potentials. Inspired by the camel- and bell-like shapes proposed by Kornyshev, we call this new shape "bird-like" capacitance, given the similarity of its shape to a flying bird. It is worth noting that the Lattice-gas approximation also predicts the bird-shaped capacitance, and this is surprising since recently Chen *et al.* [93] extended the steric-only lattice-gas model (*i.e.*, $K = 0$ in Eq. (4.17)) to account for the temperature dependence and studied the capacitance in a wide range of temperature. Still, they did not observe the bird-like capacitance. Additionally, we note that Alam *et al.* [150] have experimentally observed the appearance of humps at the potential of zero charge in the U-shaped capacitance for N_2-saturated room-temperature ILs on some electrodes; the emergence of wings in the bell-shaped capacitance was reported in a simulation study by Sha *et al.* [105] for *neat* BMIM-PF_6 on a gold surface. Our analysis suggests that these behaviors can be related to the wetting properties of ionic liquids.

Figures 6.6a and 6.6b present the capacitance diagrams in the ionophilicity-bulk density plane for a temperature above the critical temperature, that is, $T/T_c = 1.2$, meaning that the IL–solvent is always in the mixed state. These diagrams show the regions where the capacitance

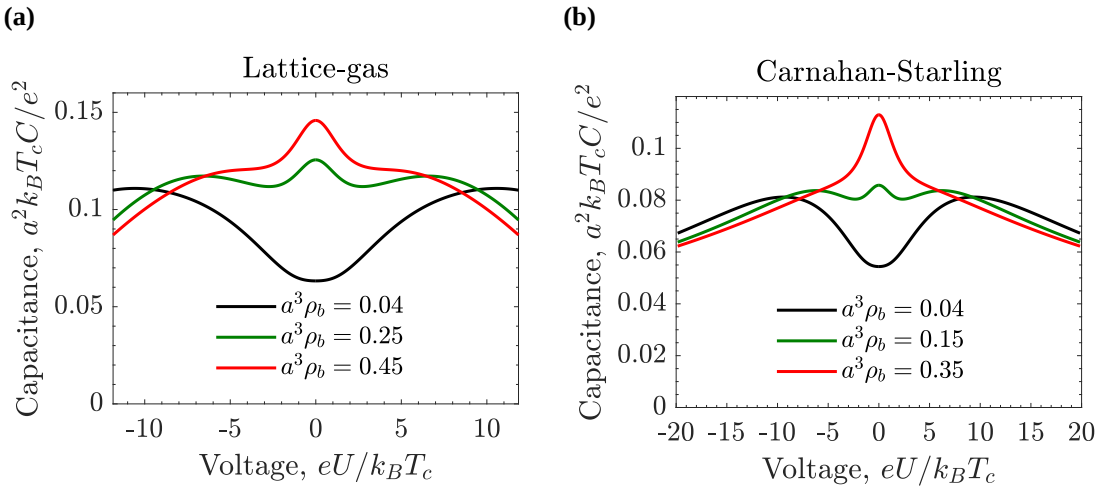

FIGURE 6.5 Differential capacitance shapes. **(a)** Differential capacitance for the Lattice-gas (lg) approximation as a function of applied potential at constant temperature,$T/T_c = 1.2$, ionophilicity $\bar{h_s} = a^3h_s/\xi_0 = 0.13$, and three different bulk densities, demonstrating the camel-, bird-, and bell-shaped capacitance. **(b)** Differential capacitance for the Carnahan-Starling (CS) approximation as a function of applied potential at constant temperature,$T/T_c = 1.2$, ionophilicity $\bar{h_s} = a^3h_s/\xi_0 = 0.025$, and three different bulk densities, demonstrating the camel-, bird-, and bell-shaped capacitance. For typical values of the ion diameter $a = 0.7\,\mathrm{nm}$ and room temperature for T_c, the various units are: thermal voltage $e/k_BT_c \approx 26\,\mathrm{mV}$ for voltage, thermal electric capacitance $e^2/(k_BT_ca^2) \approx 620\,\mu\mathrm{F\,cm^{-2}}$ for capacitance.

curves present shapes of camel, bird, and bell for the CS and lattice-gas approximations. The diagrams of both models exhibit a similar topology. However, for the lattice-gas model, the transformations between the different capacitance shapes are shifted to higher densities. This is consistent with the case in which the dispersion interactions were neglected (see Figure 6.3) and is in similarity to the bulk phase diagram, in which the demixing region is also shifted to higher densities (Figure 4.2b).

Figures 6.6c and 6.6d show the capacitance diagrams for a temperature below the critical temperature $T/T_c = 0.9$. Interestingly, the CS approximation predicts the camel-like shape even for high densities, but only provided the electrode is strongly ionophobic. This could be since, close to demixing, an ionophobic electrode (negative or low values of h_s) can induce a (macroscopically) thick layer of an ion-poor (or solvent-rich) phase in such a way that the system in the vicinity of the electrode behaves as being effectively dilute. Additionally, for higher temperatures (far from demixing according to Figure 6.4), only the bell shape is observed for dense ILs. It is also interesting to highlight that the bell- and camel-like shapes are separated by a narrow domain of bird-like capacitance. However, for the lattice-gas approximation, there is no camel shape at high densities, and only the bird- and bell-shaped capacitance are displayed.

Changes in the temperature can also induce a transformation from one capacitance shape to another at fixed bulk density, as is shown in Figures 6.7a and 6.7b. In this sense, it is interesting to analyze the advantages, from an energetic point of view, of decreasing the temperature

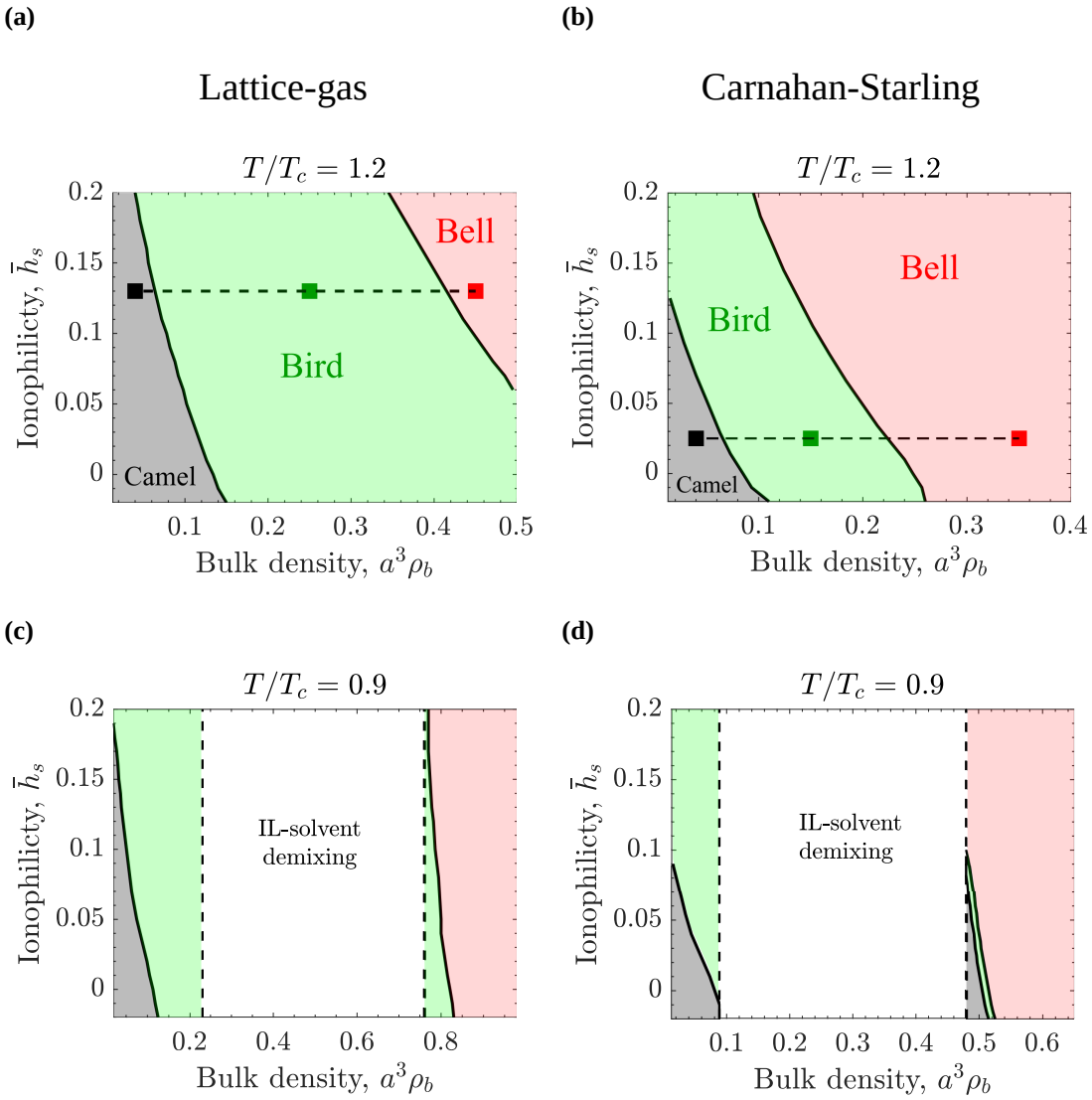

FIGURE 6.6 Differential capacitance diagrams close to demixing. **(a)** Capacitance diagram for the Lattice-gas (lg) approximation showing the regions of camel, bird, and bell-like capacitance at constant temperature, $T/T_c = 1.2$. The dashed horizontal line denotes the value of $\bar{h_s} = a^3 h_s/\xi_0 = 0.13$ and the symbols mark the bulk densities ρ_b used in Figure 6.5a. **(b)** Capacitance diagram for the Carnahan-Starling (CS) approximation showing the regions of camel, bird, and bell-like capacitance at constant temperature, $T/T_c = 1.2$. The dashed horizontal line denotes the value of $\bar{h_s} = a^3 h_s/\xi_0 = 0.025$ and the symbols mark the bulk densities ρ_b used in Figure 6.5b. **(c)** Capacitance diagram for the lg approximation for temperature below T_c, $T/T_c = 0.9$. The white region denotes the domain of the IL-solvent demixing (Figure 4.2a). **(d)** Capacitance diagram for the CS approximation for temperature below T_c, $T/T_c = 0.9$. The white region denotes the domain of the IL-solvent demixing (Figure 4.2b). For typical values of the ion diameter $a = 0.7\,\mathrm{nm}$ and room temperature for T_c, the various units are: thermal voltage $e/k_BT_c \approx 26\,\mathrm{mV}$ for voltage, thermal electric capacitance $e^2/(k_BT_ca^2) \approx 620\,\mu\mathrm{F\,cm^{-2}}$ for capacitance.

towards demixing where the bird-like capacitance emerges from the bell shape.

Additionally, to achieve a deeper insight into the charging process close to demixing, we calculated the stored energy and the charging parameter given by the Eqs. (4.24)-(4.25), respectively. Figures 6.8a and 6.8b show the stored energy obtained at two different temperatures for the lg and CS approximations. In the range of applied voltages, the stored energy is higher at $T/T_c = 1$, which is closer to demixing. The increase of the stored energy for decreasing

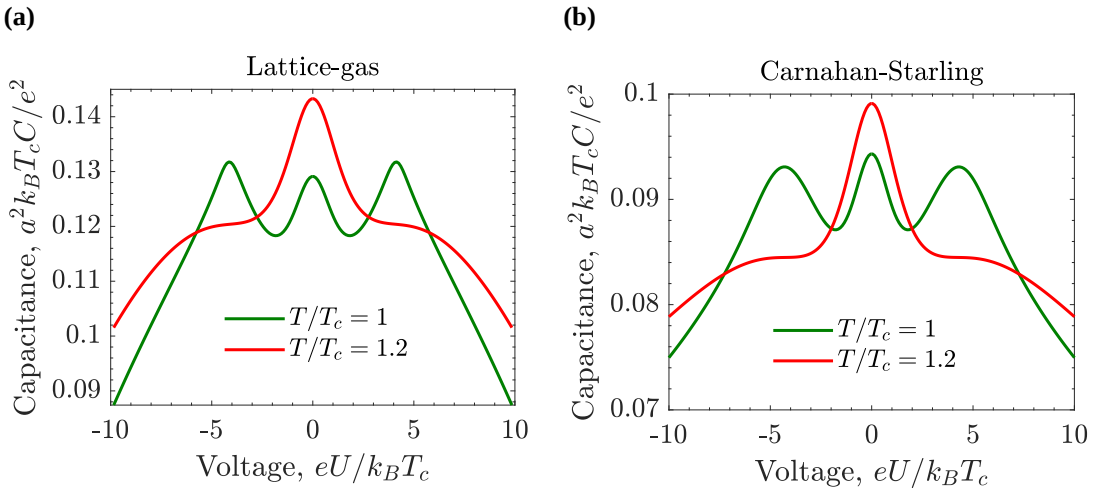

FIGURE 6.7 Differential capacitance close to demixing. (a) Differential capacitance for the Lattice-gas (lg) approximation as a function of applied potential at constant bulk density $\rho_b = 0.17$, ionophilicity $\bar{h_s} = a^3h_s/\xi_0 = 0.08$, and two different temperatures, demonstrating the bell-shaped capacitance for $T/T_c = 1.2$ and the bird-shaped capacitance for $T/T_c = 1$. **(b)** Differential capacitance for the Carnahan-Starling (CS) approximation as a function of applied potential at constant bulk density $\rho_b = 0.17$, ionophilicity $\bar{h_s} = a^3h_s/\xi_0 = 0.08$, and two different temperatures, demonstrating the bell-shaped capacitance for $T/T_c = 1.2$ and the bird-shaped capacitance for $T/T_c = 1$. For typical values of the ion diameter $a = 0.7\,\mathrm{nm}$ and room temperature for T_c, the various units are: thermal voltage $e/k_BT_c \approx 26\,\mathrm{mV}$ for voltage, thermal electric capacitance $e^2/(k_BT_ca^2) \approx 620\,\mu\mathrm{F\,cm^{-2}}$ for capacitance.

temperature can be related to the capacitance behavior. Close to demixing, capacitance increases due to the voltage-induced increase of ion density at the surface vicinity, such that the bell-shaped capacitance acquires wings, and then, the bird-shaped emerges (Figures 6.7a and 6.7b). The charging parameter, shown in Figures 6.8c and 6.8d, also corroborates this fact, since X_D becomes greater than unity for the temperature close to demixing, meaning that both cations and anions are adsorbed into the surface layer, leading to a strong peak in the charging parameter and the capacitance. However, for higher voltages, the charging parameter decreases to $X_D \approx 1$, which is consistent with the capacitance behavior that also decreases in this range of voltages. Specifically, in the case of the lattice -gas approximation (Figures 6.8a), the temperature dependence of the stored energy is weaker as compared to the CS model (Figures 6.8b). Furthermore, the two curves cross each other at higher voltages, and the stored energy becomes higher for higher temperatures. Nonetheless, qualitatively, the differential capacitance (Figures 6.7a) and the charging parameter (Figures 6.8c) exhibit similar behaviors as for the CS model.

Finally, in order to get a bigger picture of the energy dependence on temperature, Figures 6.9a and 6.9b show the stored energy and the accumulated charge, respectively, as a function of the temperature at voltage $eU/k_BT_c = 20$, bulk density $\rho_b = 0.17$ and ionophilicity $a^3h_s/\xi_0 = 0.08$ for the CS approximation. Consistently to Figure 6.8b, the stored energy (as well as the accumulated charge) increases when the temperature decreases from $T/T_c = 1.2$ to $T/T_c = 1$ (see Figures 6.9a and 6.9b) or, in other words, there is an energetic gain while the

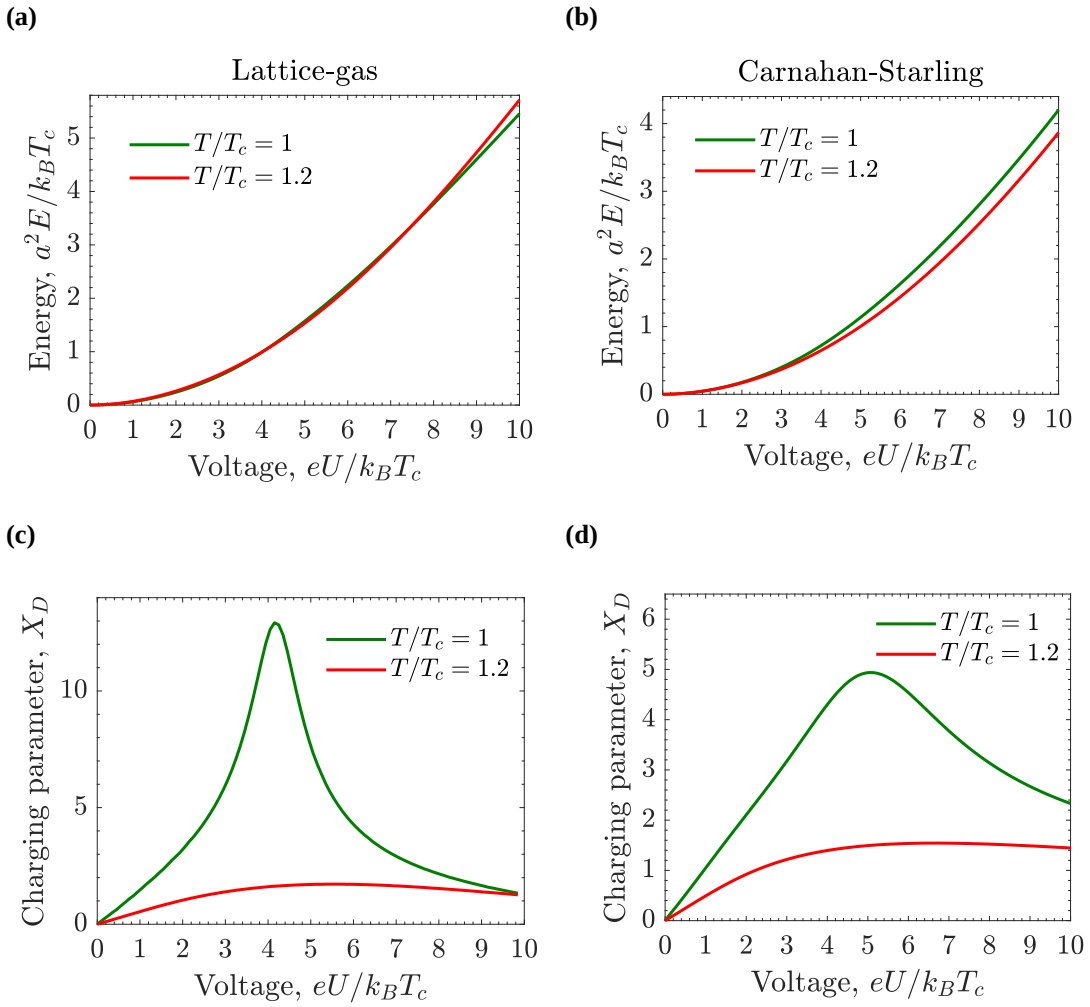

FIGURE 6.8 Energy storage and charging close to demixing. **(a)** Stored energy for the Lattice-gas (lg) approximation as a function of applied potential. **(b)** Stored energy for the Carnahan-Starling (CS) approximation as a function of applied potential at constant bulk density $\rho_b = 0.17$, ionophilicity $\bar{h_s} = a^3 h_s/\xi_0 = 0.08$, and two different temperatures: $T/T_c = 1.2$ (red curve) and $T/T_c = 1$ (green curve). **(c)** Charging parameter for the lg approximation as a function of applied potential. **(d)** Charging parameter for the CS approximation as a function of applied potential. In all the plots, the bulk density $\rho_b = 0.17$, ionophilicity $\bar{h_s} = a^3 h_s/\xi_0 = 0.08$, and two different temperatures: $T/T_c = 1.2$ (red curves) and $T/T_c = 1$ (green curves). For typical values of the ion diameter $a = 0.7\,\mathrm{nm}$ and room temperature for T_c, the various units are: thermal voltage $e/k_BT_c \approx 26\,\mathrm{mV}$ for voltage, and $k_BT_c/a^2 \approx 0.84\,\mathrm{mJ\,cm^{-2}} \approx 0.23\,\mathrm{nW\,cm^{-2}}$ for energy.

system approaches demixing. This temperature dependence of the stored energy can be used to generate electricity from waste heat [15, 151–154]. Figure 6.9d shows the order parameter and charge density profiles. At temperature $T/T_c = 1$, the order parameter grows next to the surface by accumulating more co-ions (besides the counterions) so that the ion density at the electrode increases. For the reason that the dispersion interactions favor higher ion densities, partially compensating the electrostatic repulsions. Therefore, the stored energy and the accumulated charge are higher for decreasing temperature. It is worth noting that a small peak developed in the ion density ρ and the charge density c at short distances arises due to "missing neighbors" created by the electrode (term $(\xi_0/2)\rho_0^2$ in Eq. (4.17)).

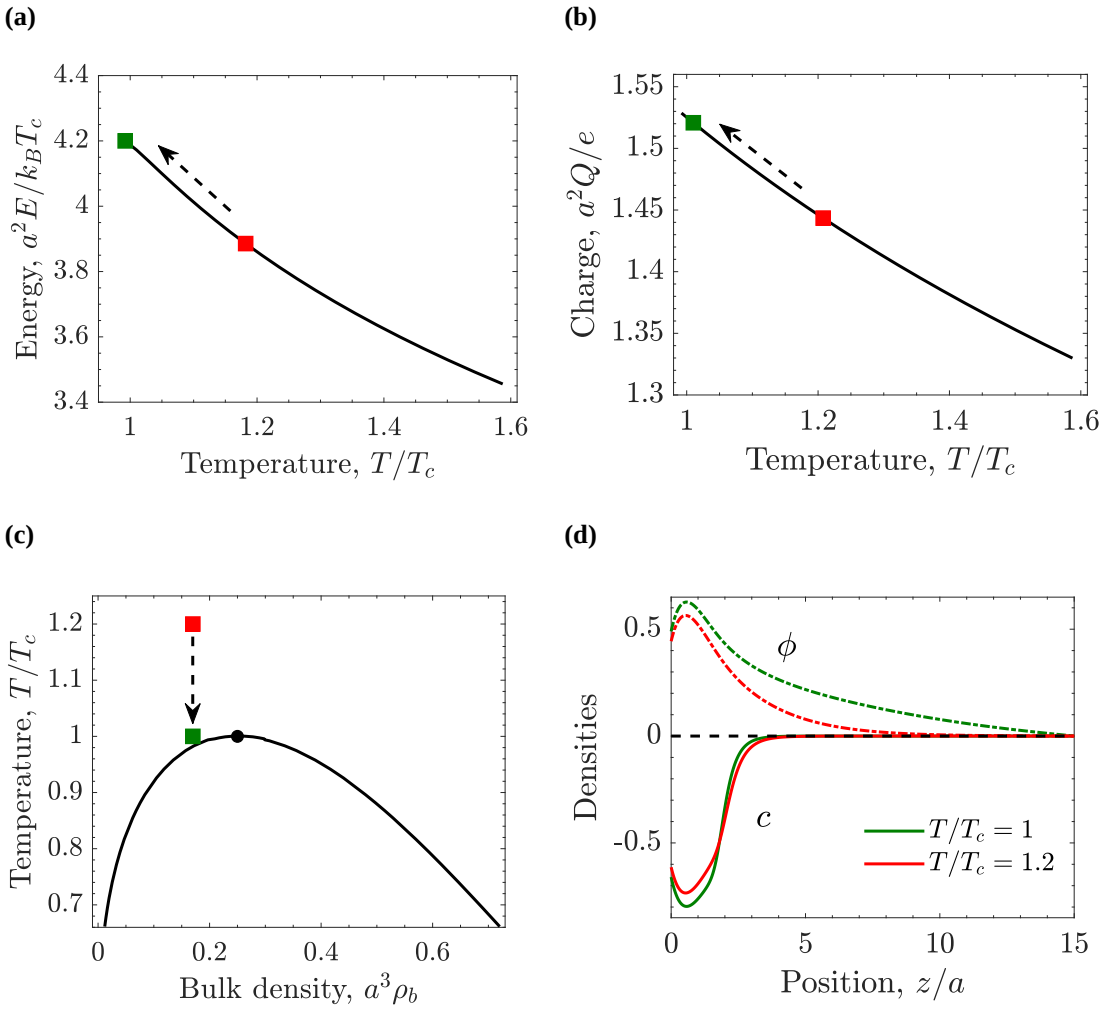

FIGURE 6.9 Stored energy behavior as a function of temperature for the Carnahan-Starling (CS) approximation. (a) Stored energy as a function of the temperature. **(b)** Charge accumulated in the EDL as a function of the temperature. The charge increases when the temperature decreases towards demixing **(c)** Bulk phase diagram in the temperature-bulk density plane showing the temperatures used in panel (a)-(b), the red square denotes $T/T_c = 1.2$, whereas the green square represents $T/T_c = 1.0$. The stored energy increases when the temperature decreases towards demixing. **(d)** Densities profiles. Order parameter $\phi = a^3(\rho - \rho_b)$ (dashed lines), where $\rho = \rho_+ + \rho_-$ is the ion density, and the charge density $c = a^3(\rho - \rho_b)$ (solid lines) calculated at $T/T_c = 1$ (green lines) and $T/T_c = 1.2$ (red lines) marked by colored squares in the previous panels. In panels (a),(b) and (d), the bulk density $\rho_b = 0.17$, voltage $eU/k_BT_c = 20$, and ionophilicity $\bar{h_s} = a^3h_s/\xi_0 = 0.08$. For typical values of the ion diameter $a = 0.7\,\mathrm{nm}$ and room temperature for T_c, the various units are: thermal voltage $e/k_BT_c \approx 26\,\mathrm{mV}$ for voltage, $e/a^2 \approx 2\,e\,\mathrm{nm}^{-2} \approx 32\,\mu\mathrm{C\,cm}^{-2}$ for accumulated charge, and $k_BT_c/a^2 \approx 0.84\,\mathrm{mJ\,cm}^{-2} \approx 0.23\,\mathrm{nW\,cm}^{-2}$ for energy.

Chapter 7

Capillary Ionization and Charging of Slit Mesopores

In this chapter, we demonstrate that a mixture of IL and neutral solvent confined into a slit-shaped mesopore undergoes a capillary ionization transition under certain conditions. In Section 7.1, the results for the case of non-polarized slit mesopore are shown; while in Section 7.2, we reveal that the capillary ionization transition can be induced by applying voltage. Additionally, we present the thermodynamic characteristics derived in Chapter 4 and analyze the influence of the slit width and electrode's ionophilicity on the energy storage. Finally, in Section 7.3, we present the calculations for the case in which the electrodes are oppositely charged and compute the integral capacitance, which will be useful in the next chapter.

We consider the mixture of IL and neutral solvent confined into a slit-shaped mesopore as shown in Figure 4.1 and take into account the Carnahan-Starling expression to describe the excluded volume interactions. As it was presented in Section 3.2, confinement induces new phase transitions and, given the system under consideration, we demonstrate that *capillary ionization* transition can be induced by changing parameters such as temperature, slit width (w), ionophilicity (h_s), and potential difference (U) applied to the pore walls. Detailed information about how the capillary ionization transition is obtained is presented in Appendix B.

7.1 Non-polarized slit-shaped mesopores

First, the case of non-polarized mesopores ($U = 0$) is studied. Figure 7.1 shows the phase diagrams in the temperature-bulk density (Figure 7.1a) and the temperature-chemical potential (Figure 7.1b) planes. Black lines denote the bulk coexistence, while the blue lines correspond to the capillary ionization (ci) curve for a slit width $w = 20a$, which is shifted with respect to the bulk system. The location of a capillary ionization transition is estimated by implementing

the Kelvin equation (Eq.(3.10)) and is shown by a solid blue line in Figure 7.1. We obtain a good quantitative agreement with the numerical solution curve shown by unfilled squares in Figure 7.1.

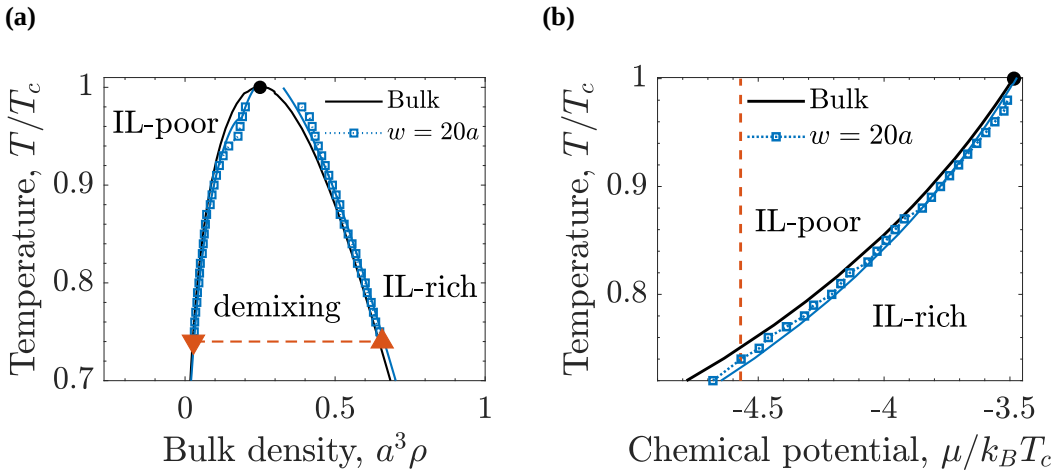

FIGURE 7.1 Capillary ionization of non-polarized slit mesopores I. (a) Phase diagram in the temperature - bulk density plane. The solid black line denotes the bulk coexistence, the solid blue line is the capillary ionization transition line estimated by the Kelvin equation, and the unfilled squares show to the capillary ionization curve obtained by numerical solution. **(b)** Phase diagram in the temperature-chemical potential plane. The colors and symbols are the same as in (a). In all the plots, the ionophilicity $a^3h_s/\xi_0 = 0.25$, and slit width $w = 20a$.

Concerning the Kelvin equation (given by Eq. (3.9)), it is important to highlight that σ_{rich} and σ_{poor} were calculated as follows, respectively

$$2\sigma_{rich} = \Omega_{rich}/A - w\,\Omega_b/V \tag{7.1}$$

$$2\sigma_{poor} = \Omega_{poor}/A - w\,\Omega_b/V \tag{7.2}$$

where Ω_b is the grand potential of the bulk system given by Eq. (4.18), and Ω_{rich} and Ω_{poor} are the grand potentials of the IL-rich and IL-poor phases, respectively, given by Eq. (4.17). From the bulk coexistence, the IL-rich and IL-poor densities, ρ_{rich} and ρ_{poor}, are known [1]. Knowing the respective densities, the EL equations are solved and their solutions are inserted in Eqs. (4.17) and (4.18) to compute Ω_{rich} and Ω_{poor}.

Figure 7.2a shows the phase diagram in the temperature-ionophilicity plane, at chemical potential $\mu/k_BT_c = -4.57$ and slit width $w = 20a$, which consists of a line of first-order phase transitions between the IL-poor and IL-rich phases. Thus, a phase transition can be induced by changing temperature or the pore wall's preference towards ions or solvent. At higher values of a^3h_s/ξ_0, the IL-rich phase is more stable since the mesopore walls have a stronger preference for IL to solvent, meaning that the walls are ionophilic. On the other hand, at lower or negative

[1] ρ_{rich} corresponds to the right branch of the temperature-bulk density phase diagram, whereas ρ_{poor} is the left branch in such diagram.

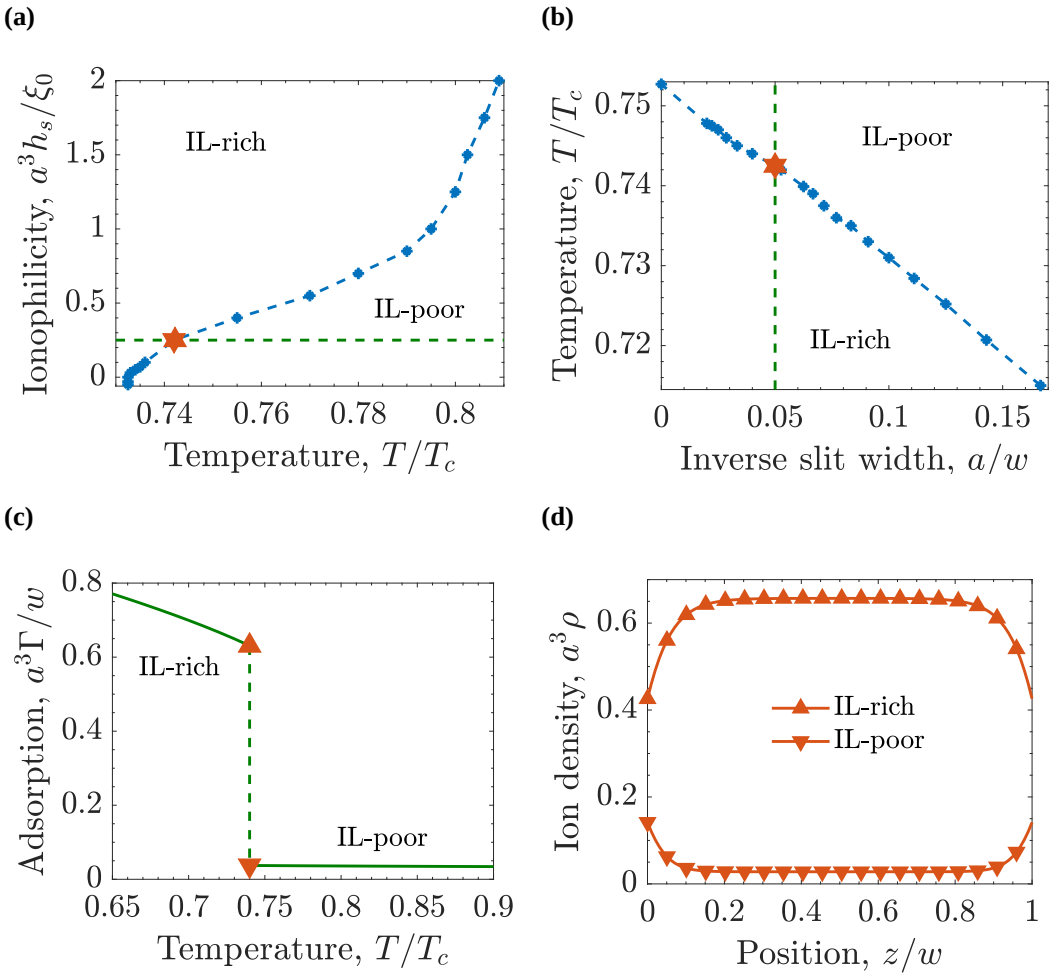

FIGURE 7.2 Capillary ionization of non-polarized slit mesopores II. **(a)** Capillary phase transition diagram in the temperature-ionophilicity plane at chemical potential $\mu/k_BT_c = -4.57$ and slit width $w = 20a$. The horizontal dashed line shows the value $a^3h_s/\xi = 0.25$ used in the results shown below, and orange symbols mark the transition temperature, T_{ci}, for this value of h_s. **(b)** Capillary phase transition diagram in $(w^{-1}, T/T_c)$ plane at chemical potential $\mu/k_BT_c = -4.57$ and ionophilicity $a^3h_s/\xi = 0.25$. The vertical dashed line indicates the slit width, $w = 20a$, implemented in the results shown below. As in (a), orange symbols mark the transition temperature, T_{ci}, for this value of $1/w$. **(c)** Amount of IL adsorbed in the pore as a function of temperature at chemical potential $\mu/k_BT_c = -4.57$, slit width $w = 20a$, and ionophilicity $a^3h_s/\xi_0 = 0.25$. Orange filled triangles (up and down), denote the transition temperature, $T_{ci} = 0.74$. **(d)** Ion density profiles inside the pore at the coexistence indicated in panel (c).

values of a^3h_s/ξ_0, solvent molecules are preferred by the pore walls, and thus, the IL-poor region is wider. Figure 7.2b is the phase diagram in the temperature-inverse of the slit width plane at chemical potential $\mu/k_BT_c = -4.57$ and ionophilicity $a^3h_s/\xi_0 = 0.25$. Thus, a phase transition can be induced by changing temperature, slit width, or the walls' preference towards ions or solvent.

Figure 7.2c shows the amount of IL adsorbed in the mesopore and reveals that capillary ionization is induced by decreasing temperature, meaning that the amount of the IL adsorbed in the pore suddenly increases at the transition as the temperature is decreased. At temperatures $T/T_c < T_{ci}/T_c$, where T_{ci} is the temperature at which capillary ionization occurs, the IL-rich phase is stable since the pore surface is ionophilic, and the thermal effects are negligible com-

pared to the IL-surface interactions. Figure 7.2d corresponds to the ion density profiles inside the pore calculated at the parameters shown by orange symbols in Figure 7.1a and Figures 7.2a and 7.2b, that is, at chemical potential $\mu/k_BT_c = -4.57$, ionophilicity $a^3h_s/\xi_0 = 0.25$ and slit width $w = 20a$.

7.2 Voltage-induced capillary ionization and charging of slit mesopores. The case of equally charged electrodes

In this section, we study the system's behavior when voltage is applied to a pore with respect to the bulk electrolyte at chemical potential $\mu/k_BT_c = -4.57$, slit width $w = 20a$, and ionophilicity $a^3h_s/\xi_0 = 0.25$. Figure 7.3 shows phase diagrams plotted in the temperature-chemical potential plane for different applied voltages, eU/k_BT_c, where the results from the Kelvin equation (Chapter 3) and the numerical solution (Chapter 5) are compared. As the applied voltage increases from 0 to 20, the transition curve is moved to the left (with respect to the curve at zero voltage), meaning that the IL-rich region becomes wider as the voltage increases. Counterintuitively, at $eU/k_BT_c = 46$, the transition line moves to the right between curves at $eU/k_BT_c = 20$ and $eU/k_BT_c = 10$. In general, there is a good agreement between the results obtained from the Kelvin equation (solid blue lines in the plots) and the numerical solution (blue squares in the plots). However, as the voltage increases, there is no similarity between the two curves in the IL-rich region, meaning that the proposed model is not suitable for such very high ion densities.

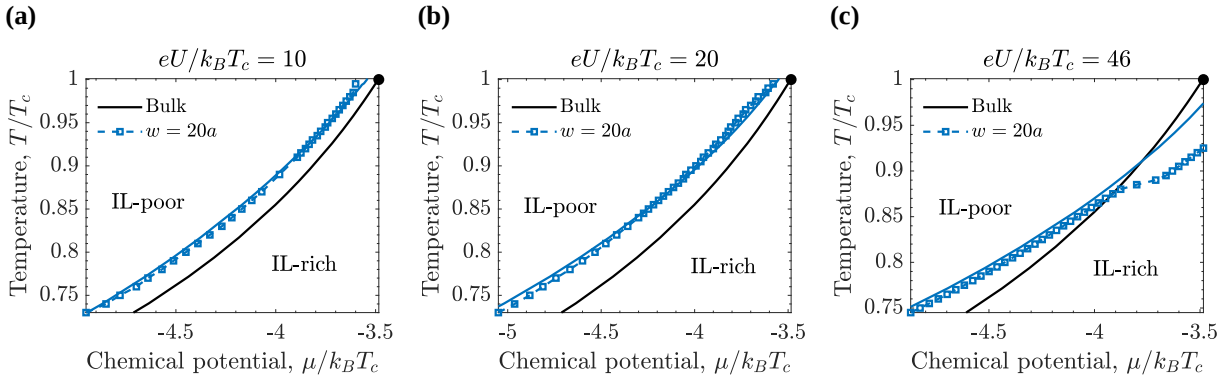

FIGURE 7.3 Capillary ionization of equally charged slit-shaped mesopore under applied voltages. Phase diagram plotted in the temperature-chemical potential plane for different applied voltages. **(a)** Voltage-induced capillary ionization at applied voltage $eU/k_BT_c = 10$. **(b)** Voltage-induced capillary ionization at applied voltage $eU/k_BT_c = 20$. **(c)** Voltage-induced capillary ionization at applied voltage $eU/k_BT_c = 46$. The slit width $w = 20a$, where a is the ion diameter, and the ionophilicity $a^3h_s/\xi_0 = 0.25$, where ξ_0 is the bare correlation length. In all the plots, the symbols have been obtained by numerical calculations shown in Chapter 5, and the blue solid line corresponds to the results of the Kelvin equation derived in Chapter 3 (Eq. (3.10)).

Figure 7.4a is a phase diagram plotted in the voltage-temperature plane and shows that the region of the IL-rich phase becomes wider as the voltage is applied to a pore with respect to the bulk electrolyte. The applied potential favors the counter-ions to stay inside the pore, and at the

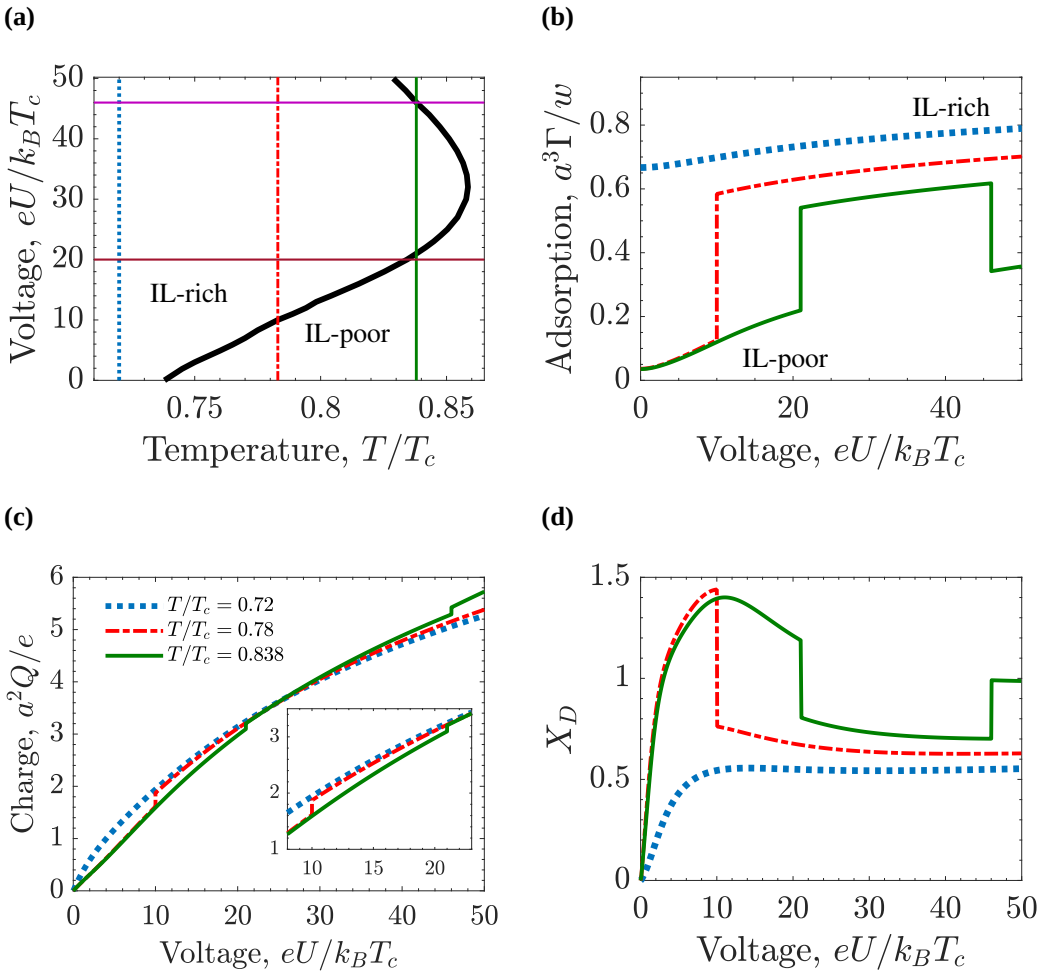

FIGURE 7.4 Voltage-induced capillary ionization and charging of equally charged slit-shaped mesopore. (a) Phase diagram in the voltage-temperature plane. The thick black line denotes the first-order transitions between the IL-rich and IL-poor phases while the thin vertical lines indicate the temperatures: $T/T_c = 0.72$ (blue), $T/T_c = 0.78$ (red), $T/T_c = 0.838$ (green), used in the other panels. The horizontal lines show the values of voltage used in Figure 7.9. **(b)** Amount of IL adsorbed in the pore. **(c)** Accumulated charge in the pore as a function of the applied voltage. **(d)** Charging parameter, X_D. In all the plots the pore width $w = 20a$, chemical potential $\mu/k_BT_c = -4.57$ and ionophilicity $a^3h_s/\xi_0 = 0.25$, where ξ_0 is the bare correlation length and a the ion diameter. For typical values of the ion diameter $a = 0.7\,\mathrm{nm}$ and room temperature for T_c, the various units are: thermal voltage $e/k_BT_c \approx 26\,\mathrm{mV}$ for voltage, and $e/a^2 \approx 2\,e\,\mathrm{nm}^{-2} \approx 32\,\mu\mathrm{C\,cm}^{-2}$ for accumulated charge.

same time, co-ions are brought along. However, at high voltages, $eU/k_BT_c > 32$, the transition curve bends, and the IL-poor phase becomes wider, implying that the capillary ionization transition takes place from the IL-rich phase to the IL-poor phase for increasing voltage. The vertical lines denote the temperatures at which the thermodynamic characteristics such as accumulated charge, differential capacitance, adsorption, charging parameter, and stored energy are calculated. Figures 7.4b to 7.4d show the ion adsorption, Γ, accumulated charge, (Q), and the charging parameter, X_D, respectively, calculated at three different temperatures. Capillary ionization transition can be induced by applying a voltage to a mesopore, and this transition is accompanied by an abrupt increase of the charge accumulated in the pore (Figure 7.4c); this fact has important consequences for capacitance and energy storage.

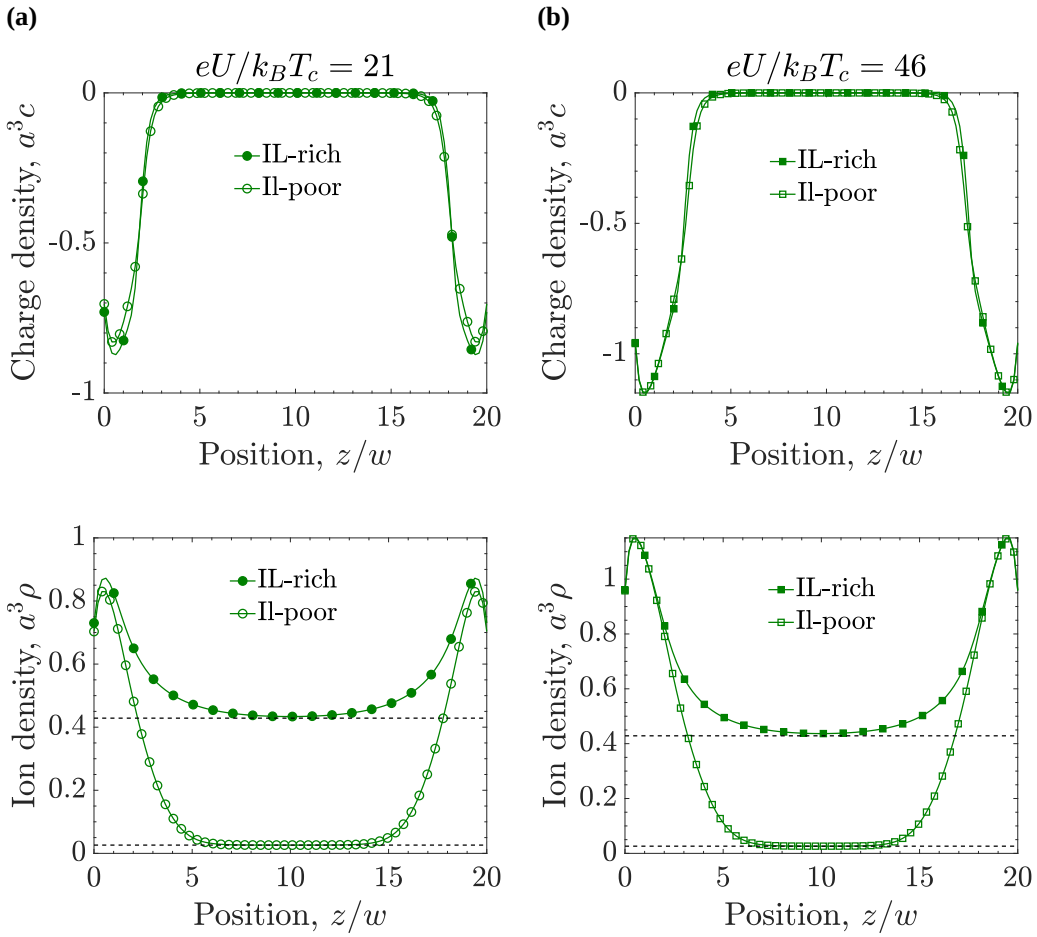

FIGURE 7.5 Charge and ion density profiles at the capillary ionization transition of equally charged slit-shaped mesopores. (a) Charge and ion density profiles at $eU/k_BT_c = 21$. **(b)** Charge and ion density profiles at $eU/k_BT_c = 46$. In all the plots, the chemical potential $\mu/k_BT_c = -4.57$, the temperature $T/T_c = 0.838$, slit width $w = 20a$, and ionophilicity $a^3h_s/\xi_0 = 0.25$, where ξ_0 is the bare correlation length and a the ion diameter. The dashed horizontal lines show the bulk values in the corresponding phases. The filled symbols represent the IL-rich phase while the unfilled symbols denote the IL-poor phase.

In the case in which there is no transition ($T/T_c = 0.72$), the characteristics Γ, Q, and X_D are all continuous functions of voltage. At $T/T_c = 0.78$, a capillary phase transition occurs at $eU/k_BT_c = 10$, and thus, there is a jump in Γ that represents the transition from the IL-poor to IL-rich phase. However, the behavior at $T/T_c = 0.838$ seems peculiar since Γ exhibits two transitions, from the IL-poor to IL-rich phase at $eU/k_BT_c = 21$, and the other one from IL-rich to IL-poor phase at $eU/k_BT_c = 46$. Figure 7.4d shows the charging parameter, X_D. In the IL-poor phase, X_D quickly becomes larger than unity, which means that charging proceeds by adsorption of both co and counter-ions. In the IL-rich phase, $0 < X_D < 1$ and hence charging is a combination of counter-ion adsorption and co-ion swapping for counter-ions.

In order to obtain a deeper understanding of the re-entrant behavior of the capillary ionization line in Figure 7.4a, we analyze the charge and ion density profiles for $T/T_c = 0.838$ at $eU/k_BT_c = 21$ and $eU/k_BT_c = 46$ (Figure 7.5). The difference between the ion structures near the pore walls in the IL-rich and IL-poor phases decreases for increasing voltage. At high voltage, the charge density as well as the ion density near the pore walls ($z/w < 2.5$ and

$z/w > 17.5$) are the same in both phases. Thus, the thermodynamic state becomes determined by the in-pore bulk region, favoring the IL-poor phase.

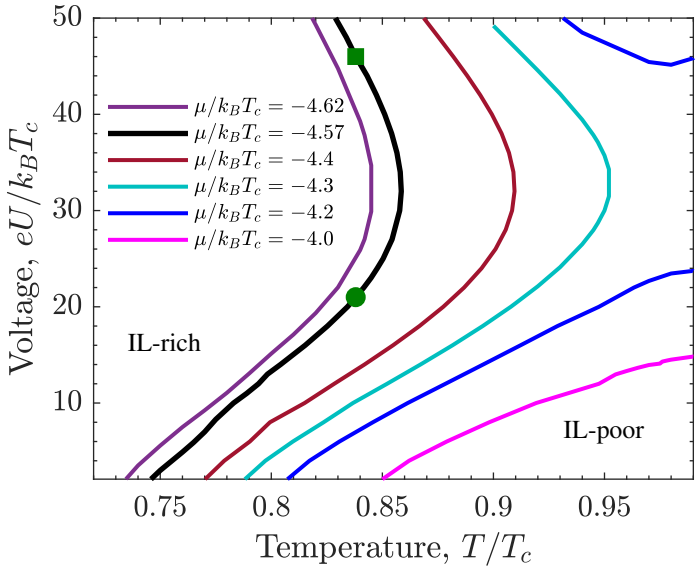

FIGURE 7.6 Voltage-induced capillary ionization of equally charged slit-shaped mesopore at different chemical potentials. Phase diagrams in the voltage-temperature plane showing first-order transitions between the IL-rich and IL-poor phases for a few values of the chemical potential. The black thick line corresponds to the chemical potential $\mu/k_BT_c = -4.57$ of Figure 7.4a. The pore width $w = 20a$ and ionophilicity $a^3h_s/\xi_0 = 0.25$, where ξ_0 is the bare correlation length and a the ion diameter. The green symbols mark the voltages used to calculate the profiles shown in Figure 7.5.

Intending to obtain a wider picture of the re-entrant behavior, we consider a few more chemical potentials in the phase diagram plotted in the temperature-voltage plane. Figure 7.6 shows that at high temperatures, it is possible that, instead of bending, the transition line breaks into two lines ending at their respective critical points; these critical points form a critical line at which the surface of first-order transitions ends. However, in this region, locating the transitions appears problematic within our numerical approach.

Figure 7.7a shows the differential capacitance. At low temperatures, the system is in the IL-rich region, characterized by a high ion density, and hence, the capacitance has a bell shape, consistent with earlier studies [78]. At higher temperatures, the IL-poor phase becomes stable, and the capacitance shape changes to bird-like [80, 98]. It is worth noting that, according to Eq. (4.34), the capacitance at the capillary ionization diverges; thus, the vertical arrows in Figure 7.7a for the temperatures $T/T_c = 0.78$ and $T/T_c = 0.838$ denote this divergence, meaning that the capacitance tends to infinity at the capillary ionization transition. Figure 7.7b corresponds to the stored energy in the pore, and from Eq. (4.37), one can see that there is an additional contribution at the transition given by $\Delta E_{ci} = u_{ci}\Delta Q_{ci}$, which appears as a jump in the stored energy.

Figure 7.8 shows the magnitude of the jumps in the accumulated charge, ΔQ_{ci}, and stored energy, ΔE_{ci}, along the transition line in Figure 7.4a. This transition curve bends at $eU/k_BT_c \approx 32$ and for voltages $eU/k_BT_c < 32$, the transition proceeds from IL-poor to IL-rich

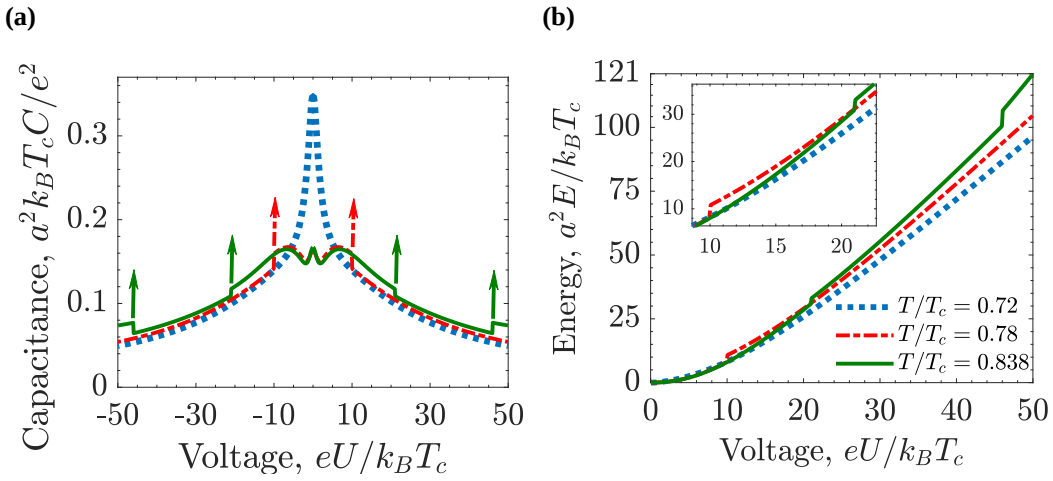

FIGURE 7.7 Differential capacitance and stored energy at the capillary ionization of equally charged slit-shaped mesopore. (a) Differential capacitance.**(b)** Stored energy. The chemical potential $\mu/k_BT_c = -4.57$, the pore width $w = 20a$, and ionophilicity $a^3h_s/\xi_0 = 0.25$, where ξ_0 is the bare correlation length and a the ion diameter. In both plots, blue lines denote $T/T_c = 0.72$, red $T/T_c = 0.78$, and green $T/T_c = 0.838$. The vertical arrows indicate that capacitance diverges at the capillary ionization transition according to the Dirac delta function in Eq. (4.34). For typical values of the ion diameter $a = 0.7\,\mathrm{nm}$ and room temperature for T_c, the various units are: thermal voltage $e/k_BT_c \approx 26\,\mathrm{mV}$ for voltage, thermal electric capacitance $e^2/(k_BT_ca^2) \approx 620\,\mu\mathrm{F\,cm^{-2}}$ for capacitance, and $k_BT_c/a^2 \approx 0.84\,\mathrm{mJ\,cm^{-2}} \approx 0.23\,\mathrm{nW\,cm^{-2}}$ for energy.

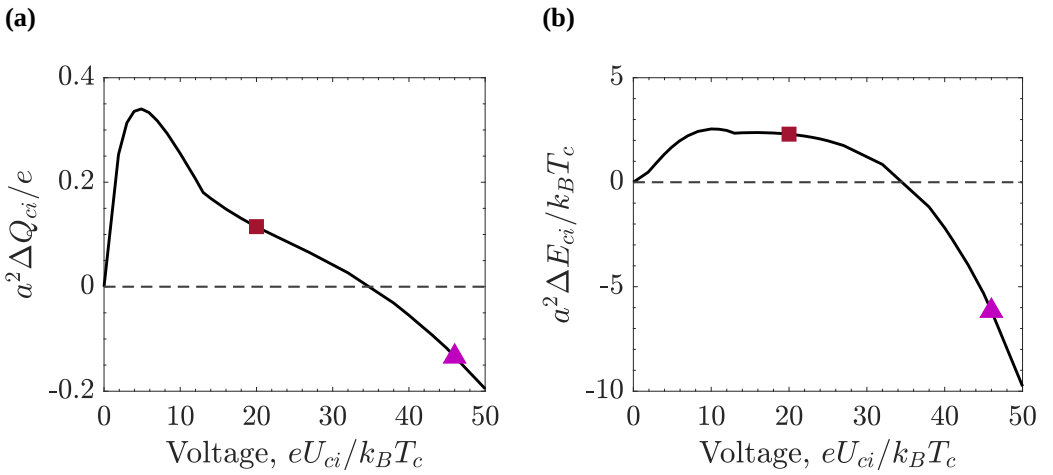

FIGURE 7.8 Magnitude of the jumps in the accumulated charge and stored energy along the capillary ionization line. (a) Jumps in the accumulated charge as a function of the transition voltage eU_{ci}/k_BT_c. **(b)** Jumps in the stored energy as a function of the transition voltage eU_{ci}/k_BT_c. Chemical potential $\mu/k_BT_c = -4.57$, slit width $w = 20a$ and ionophilicity $a^3h_s/\xi_0 = 0.25$, where ξ_0 is the bare correlation length and a the ion diameter. Symbols mark the transition voltage in Figure 7.9. For typical values of the ion diameter $a = 0.7\,\mathrm{nm}$ and room temperature for T_c, the various units are: thermal voltage $e/k_BT_c \approx 26\,\mathrm{mV}$ for voltage, $e/a^2 \approx 2\,e\,\mathrm{nm^{-2}} \approx 32\,\mu\mathrm{C\,cm^{-2}}$ for accumulated charge, and $k_BT_c/a^2 \approx 0.84\,\mathrm{mJ\,cm^{-2}} \approx 0.23\,\mathrm{nW\,cm^{-2}}$ for energy.

phase, and thus, the magnitude of the jump in the charge and the energy is positive. Nevertheless, this jump upon capillary ionization is negative for voltages $eU/k_BT_c > 32$, where the transition occurs from the IL-rich to IL-poor phase. Examples of a positive and negative magnitude of the jump in the charge and the energy are shown in Figure 7.9 which corresponds to the charge

and stored energy in a pore as a function of the temperature, calculated at $eU/k_BT_c = 20$ and $eU/k_BT_c = 46$ (these voltages are marked by symbols in Figure 7.8). It is important to note that there is no direct linear correspondence between the accumulated charge (integral capacitance) and the stored energy. In particular, a decrease in the accumulated charge may accompany an increase in the stored energy.

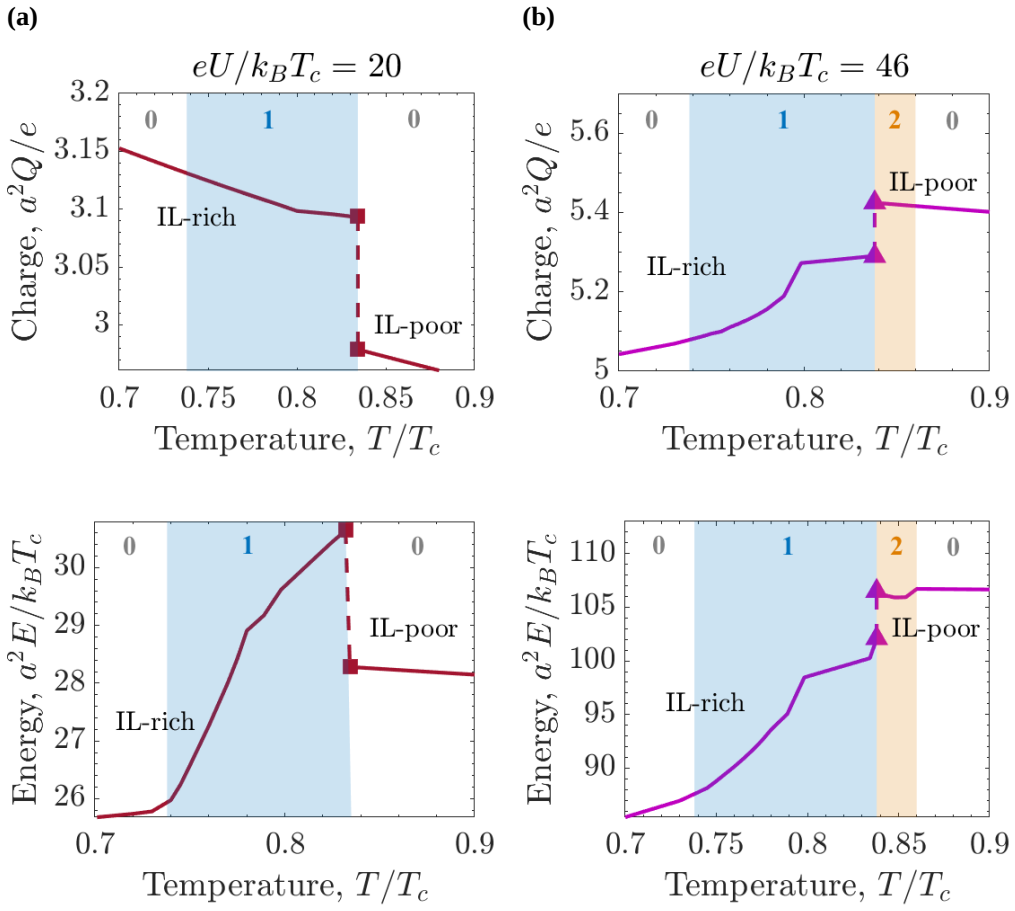

FIGURE 7.9 Accumulated charge and stored energy in equally charged slit-shaped mesopore as a function of temperature. **(a)** Accumulated charge (top) and stored energy (bottom) for applied voltage $eU/k_BT_c = 20$. **(b)** Accumulated charge (top) and stored energy (bottom) for applied voltage $eU/k_BT_c = 46$. The colored areas show the regions with one and two transitions as indicated by the corresponding numbers. Chemical potential $\mu/k_BT_c = -4.57$, slit width $w = 20a$ and ionophilicity $a^3h_s/\xi_0 = 0.25$, where ξ_0 is the bare correlation length and a the ion diameter.

7.2.1 Influence of the slit width and ionophilicity on the energy storage

It is interesting to study the influence of ionophilicity and the slit width on both the accumulated charge and the stored energy of the system. Figures 7.10a and 7.10b show the accumulated charge and stored energy as a function of the ionophilicity for three different temperatures: $T/T_c = 0.72$, $T/T_c = 0.78$ and $T/T_c = 0.838$ at voltage $eU/k_BT_c = 50$ and fixed slit width $w = 20a$. The accumulated charge increases for increasing ionophilicity, meaning that more ions are attracted to the electrode's surface. However, the stored energy decreases at higher ionophilicities, and the capacitance's shape could explain such behavior. Strongly ionophilic

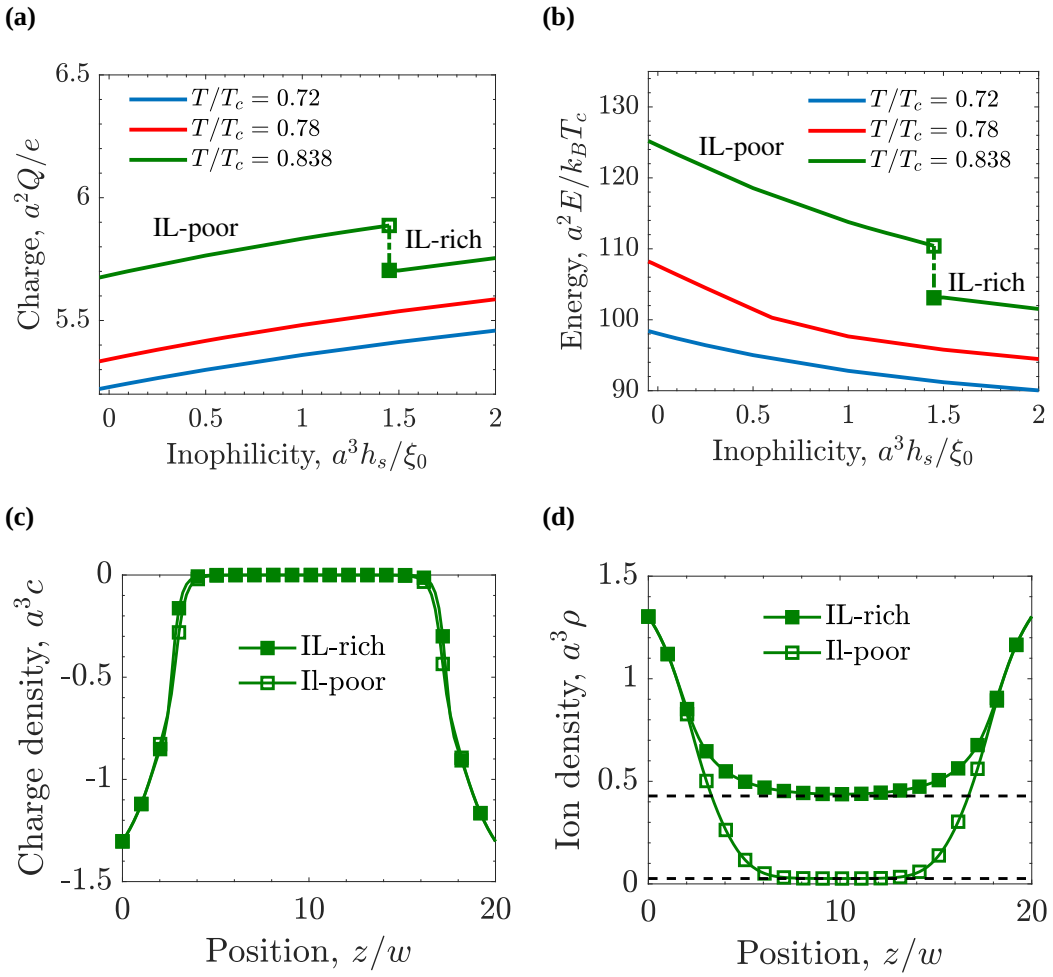

FIGURE 7.10 Ionophilicity's influence on the accumulated charge and stored energy of equally charged slit-shaped mesopore. (a) Accumulated charge as a function of the ionophilicity at voltage $eU/k_BT_c = 50$ and slit width $w = 20a$. The blue lines correspond to temperature $T/T_c = 0.72$, red lines to $T/T_c = 0.78$, and green lines to $T/T_c = 0.838$. **(b)** Stored energy as a function of the ionophilicity at voltage $eU/k_BT_c = 50$ and slit width $w = 20a$. The blue lines correspond to temperature $T/T_c = 0.72$, red lines to $T/T_c = 0.78$, and green lines to $T/T_c = 0.838$. In panels (a) and (b), the filled and unfilled squares mark the parameters used in panels (c) and (d), and denote the IL-rich and IL-poor phases coexisting at the capillary ionization transition. **(c)** Charge density profile at $T/T_c = 0.838$, ionophilicity $a^3h_s/\xi_0 = 1.45$, and slit width $w = 20a$. **(d)** Ion density profile at $T/T_c = 0.838$, ionophilicity $a^3h_s/\xi_0 = 1.45$, and slit width $w = 20a$. In all the plots, the chemical potential $\mu/k_BT_c = -4.57$, ξ_0 is the bare correlation length and a the ion diameter. For typical values of the ion diameter $a = 0.7\,\mathrm{nm}$ and room temperature for T_c, the various units are: thermal voltage $e/k_BT_c \approx 26\,\mathrm{mV}$ for voltage, $k_BT_c/a^2 \approx 0.84\,\mathrm{mJ\,cm^{-2}} \approx 0.23\,\mathrm{nW\,cm^{-2}}$ for energy, and $e/a^2 \approx 2\,e\,\mathrm{nm^{-2}} \approx 32\,\mu\mathrm{C\,cm^{-2}}$ for accumulated charge.

electrodes display a bell-shaped capacitance in which there is a high amount of ions close to the electrode's surface (maximum at PZC). Still, the capacitance rapidly decreases for higher voltages. The stored energy is directly related to the capacitance's behavior, and for this reason, decreases when ionophilicity increases. Consistently to Figure 7.4a, there is a jump in the accumulated charge and the stored energy indicating the capillary phase transition at temperature $T/T_c = 0.838$. The filled and unfilled squares denote the IL-rich and IL-poor phases, respectively, that coexist at the phase transition ($a^3h_s/\xi_0 = 1.45$). Figures 7.10c and 7.10d show

the ion and charge density profiles at the capillary ionization transition. At such high voltage, $eU/k_BT_c = 50$, the near-surface structure of ions are similar in both phases. Thus, the system's behavior is determined by the bulk-like conditions.

Figures 7.11a and 7.11b show the accumulated charge and the stored energy, respectively, as a function of the slit width at voltage $eU/k_BT_c = 50$, temperature $T/T_c = 0.838$ (this temperature is shown by a green vertical line in Figure 7.4a), and three different values of the surface field or ionophilicty: $a^3h_s/\xi_0 = -0.05$, $a^3h_s/\xi_0 = 0.25$, and $a^3h_s/\xi_0 = 2$. These values correspond to cases of ionophobic electrodes, medium ionophilic electrodes and strongly ionophilic electrodes, respectively.

In Figure 7.11a, the accumulated charge is higher for the strongest ionophilic electrode ($a^3h_s/\xi_0 = 2$), meaning that more ions are brought to the surface. Thus the electrostatic attractions and the van der Waals interactions between the pore walls and the ions are additive and stronger than the repulsive forces. The jump in every curve marks the capillary ionization transition occurring at w_{ci}. For $w < w_{ci}$, the IL-rich phase is stable, whereas the IL-poor phase is stable for $w > w_{ci}$. The accumulated charge decreases when the slit width increases within the respective stable phase. In a wider slit, the ion-wall interactions become weaker since the ions are distributed in a wider space, and then, the accumulated charge decreases.

Let us consider $a^3h_s/\xi_0 = 0.25$ (red curve in Figure 7.11a). The filled and unfilled squares mark the IL-rich and IL-poor phases, respectively, coexisting at the capillary phase transition. For $w \leq 10a$, the ions in the center of the slit perceive both electrodes with equal strength, and the attraction of counterions and repulsion of coions to the center of the slit is stronger since it comes from two electrodes. Close to an electrode, the second one does not interact strongly with ions if the first one is far away. For this reason, for $w > 20a$, the accumulated charge depends on w very weakly. The central part is bulk-like and does not contribute to the charge. Figure 7.11c shows the charging parameter, X_D. At $u < U_{ci}$ (with $eU_{ci}/k_BT_c = 17.6$), the IL-poor phase is stable and, as it was presented in Section 4.4, since $X_D > 1$ in the IL-poor phase, both coions and counterions are adsorbed into the surface. Consistently, the differential capacitance (Figure 7.11d) is higher for $u < U_{ci}$. On the other hand, for $u > U_{ci}$, the IL-rich phase is stable and $0 < X_D < 1$, meaning that there is a partial swapping of coions for counterions. Then, the charging parameter decreases as the voltage increases. The differential capacitance exhibits such behavior as well, implying that, near the surface, there is a dense layer of counterions as the voltage increases. Thus, there is a screening that causes a rapid decrease in the capacitance.

The stored energy, however, decreases for strongly ionophilic electrodes, and the differential capacitance shapes can explain such a behavior. As presented in Figure 6.6 (Chapter 6), strongly ionophilic electrodes display a bell-shaped capacitance, characterized by a peak at PZC (due to the high amount of ions in the surface); however, capacitance decreases for higher voltages due to the screening of a dense ionic layer at the electrode surface. An ionophobic electrode displays the camel-shaped capacitance that exhibits a minimum at PZC and two maxima at higher voltages. Since the energy depends on $C(u)\ u$ (see Eq. (4.24)), therefore the maximum

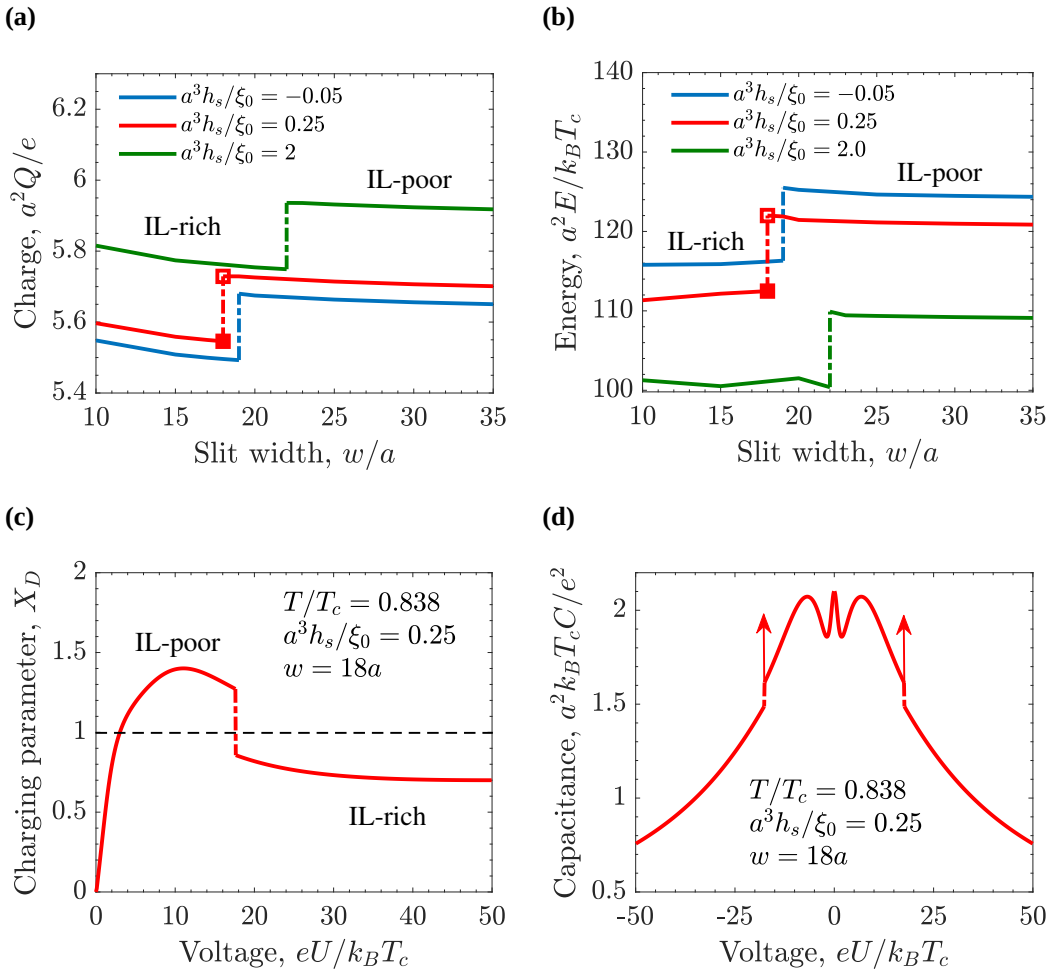

FIGURE 7.11 Influence of the slit width on the accumulated charge and stored energy of equally charged slit-shaped mesopore. **(a)** Accumulated charge as a function of the ionophilicity at voltage $eU/k_BT_c = 50$ and temperature $T/T_c = 0.838$. The blue lines correspond to ionophilicity $a^3h_s/\xi_0 = -0.05$ (ionophobic electrodes), red lines to $a^3h_s/\xi_0 = 0.25$ (medium-ionophilic electrodes), and green lines to $a^3h_s/\xi_0 = 2$ (strongly ionophilic electrodes); where ξ_0 is the bare correlation length and a the ion diameter. **(b)** Stored energy as a function of the ionophilicity at voltage $eU/k_BT_c = 50$ and temperature $T/T_c = 0.838$. The blue lines correspond to ionophilicity $a^3h_s/\xi_0 = -0.05$ (ionophobic electrodes), red lines to $a^3h_s/\xi_0 = 0.25$ (medium-ionophilic electrodes), and green lines to $a^3h_s/\xi_0 = 2$ (strongly ionophilic electrodes); where ξ_0 is the bare correlation length and a the ion diameter. In panels (a) and (b), the filled and unfilled squares denote the IL-rich and IL-poor phases coexisting at the capillary ionization transition. **(c)** Charging parameter as a function of the voltage at temperature $T/T_c = 0.838$, ionophilicity $a^3h_s/\xi_0 = 0.25$, and slit width $w = 18a$. **(d)** Differential capacitance at temperature $T/T_c = 0.838$, ionophilicity $a^3h_s/\xi_0 = 0.25$, and slit width $w = 18a$. The vertical arrows indicate that capacitance diverges at the capillary ionization transition according to the Dirac delta function in Eq. (4.34). In all the plots, the chemical potential $\mu/k_BT_c = -4.57$. For typical values of the ion diameter $a = 0.7\,\mathrm{nm}$ and room temperature for T_c, the various units are: thermal voltage $e/k_BT_c \approx 26\,\mathrm{mV}$ for voltage, $k_BT_c/a^2 \approx 0.84\,\mathrm{mJ\,cm^{-2}} \approx 0.23\,\mathrm{nW\,cm^{-2}}$ for energy, and $e/a^2 \approx 2\,e\,\mathrm{nm^{-2}} \approx 32\,\mu\mathrm{C\,cm^{-2}}$ for accumulated charge.

at larger voltages leads to larger energy. Medium-ionophilic electrodes display the bird-shaped capacitance.

7.3 Voltage-induced capillary ionization and charging of slit mesopores. The case of oppositely charged electrodes

In this section, we study the case in which the walls of the mesopore are oppositely charged [2] at chemical potential $\mu/k_BT_c = -4.57$, slit width $w = 20a$, and ionophilicity $a^3h_s/\xi_0 = 0.25$. In this case, the solution presented in Chapter 5 remains valid but the BCs related to the electrostatic potential are $u(0) = -eU/k_BT_c$ and $u(w) = eU/k_BT_c$.

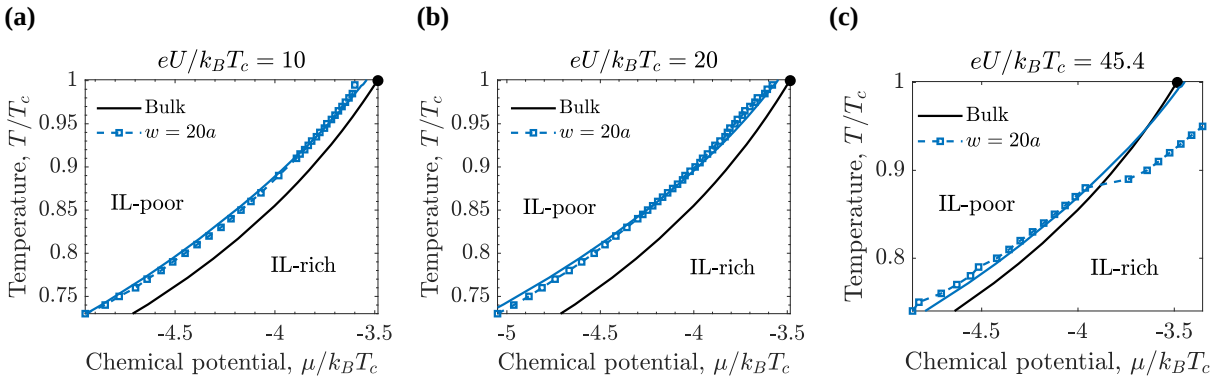

FIGURE 7.12 Capillary ionization of oppositely charged slit-shaped mesopores. Phase diagram plotted in the temperature-chemical potential plane for different applied voltages. **(a)** Voltage-induced capillary ionization at applied voltage $eU/k_BT_c = 10$. **(b)** Voltage-induced capillary ionization at applied voltage $eU/k_BT_c = 20$. **(c)** Voltage-induced capillary ionization at applied voltage $eU/k_BT_c = 45.4$. The slit width $w = 20a$, where a is the ion diameter, and the ionophilicity $a^3h_s/\xi_0 = 0.25$, where ξ_0 is the bare correlation length. In all the the plots, the symbols have been obtained by numerical calculations shown in Chapter 5, and the blue solid line corresponds to the results of the Kelvin equation derived in Chapter 3 (Eq. (3.10)).

Figure 7.12 shows phase diagrams plotted in the temperature-chemical potential plane for different applied voltages, eU/k_BT_c, where the results from the Kelvin equation (Chapter 3) and the numerical solution (Chapter 5) are compared. As the applied voltage increases from 0 to 45.4, the transition curve is moved to the left (with respect to the curve at zero voltage), meaning that the IL-rich region becomes wider as the voltage increases. There is a fair agreement between the results obtained from the Kelvin equation (solid blue lines in the plots) and the numerical solution (blue squares in the plots). However, at higher voltages where the IL-rich phase is favored, there is no similarity between the two curves, especially at high temperatures.

In the case of oppositely charged walls, we obtain a similar behavior to that of the case of equally charged electrodes. Figure 7.13a is a phase diagram plotted in the voltage-temperature plane. The IL-rich phase region becomes wider as the voltage is applied to a pore with respect to the bulk electrolyte. We also observe the re-entrant behavior, meaning that the capillary ionization line bends at higher voltages where the transition occurs from the IL-rich phase to the IL-poor phase. Similarly, the vertical lines denote the temperatures at which the thermodynamic characteristics such as accumulated charge, differential capacitance,

[2] This case corresponds to a conventional electrochemical double-layer capacitor.

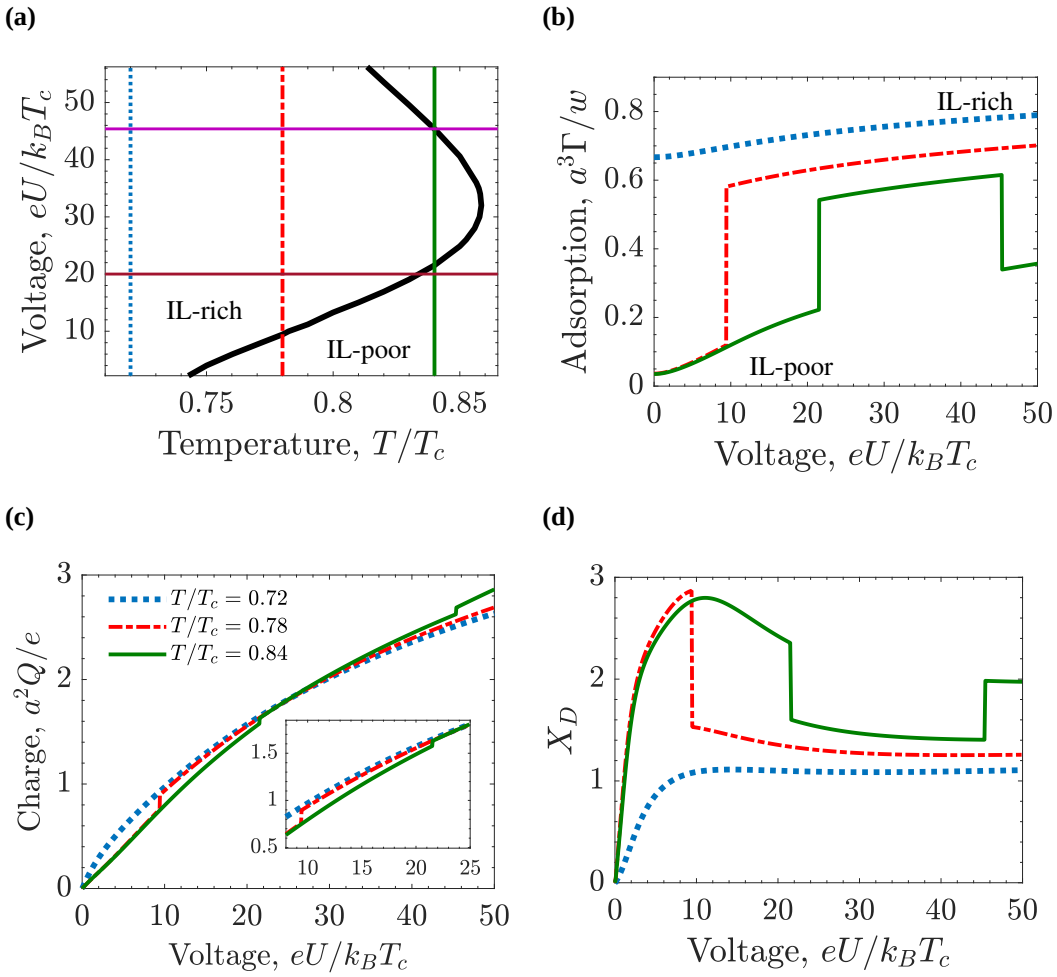

FIGURE 7.13 Voltage-induced capillary ionization and charging of oppositely charged slit-shaped mesopores. (a) Phase diagram in the voltage-temperature plane. The thick black line denotes the first-order transitions between the IL-rich and IL-poor phases while the thin vertical lines indicate the temperatures: $T/T_c = 0.72$ (blue), $T/T_c = 0.78$ (red), $T/T_c = 0.84$ (green), used in the other panels. The horizontal lines mark the voltages $eU/k_BT_c = 20$ and $eU/k_BT_c = 45.4$ used in Figure 7.16. **(b)** Amount of IL adsorbed in the pore. **(c)** Accumulated charge in the pore as a function of the applied voltage. **(d)** Charging parameter, X_D. The chemical potential $\mu/k_BT_c = -4.57$, the pore width $w = 20a$, and ionophilicity $a^3h_s/\xi_0 = 0.25$, where ξ_0 is the bare correlation length and a the ion diameter. In all the plots, blue lines denote $T/T_c = 0.72$, red $T/T_c = 0.78$, and green $T/T_c = 0.84$. For typical values of the ion diameter $a = 0.7\,\mathrm{nm}$ and room temperature for T_c, the various units are: thermal voltage $e/k_BT_c \approx 26\,\mathrm{mV}$ for voltage, and $e/a^2 \approx 2\,e\,\mathrm{nm}^{-2} \approx 32\,\mu\mathrm{C\,cm}^{-2}$ for accumulated charge.

adsorption, charging parameter, and stored energy are calculated. Figures 7.13b, 7.13c and 7.13d show the ion adsorption, Γ, accumulated charge, (Q), and the charging parameter, X_D, respectively, calculated at $T/T_c = 0.72$, $T/T_c = 0.78$, and $T/T_c = 0.84$.

Let us consider now the case in which there are two transitions, $T/T_c = 0.84$ (green line in Figure 7.13a). Figure 7.14 shows the charge and ion density profiles at $eU/k_BT_c = 21.5$ and $eU/k_BT_c = 45.4$. The difference between the ion structures near the pore walls in the IL-rich and IL-poor phases decreases for increasing voltage. At high voltage, the charge density as well as the ion density near the pore walls ($z/w < 2.5$ and $z/w > 17.5$) are the same in both phases. Thus, the thermodynamic state becomes determined by the in-pore bulk region,

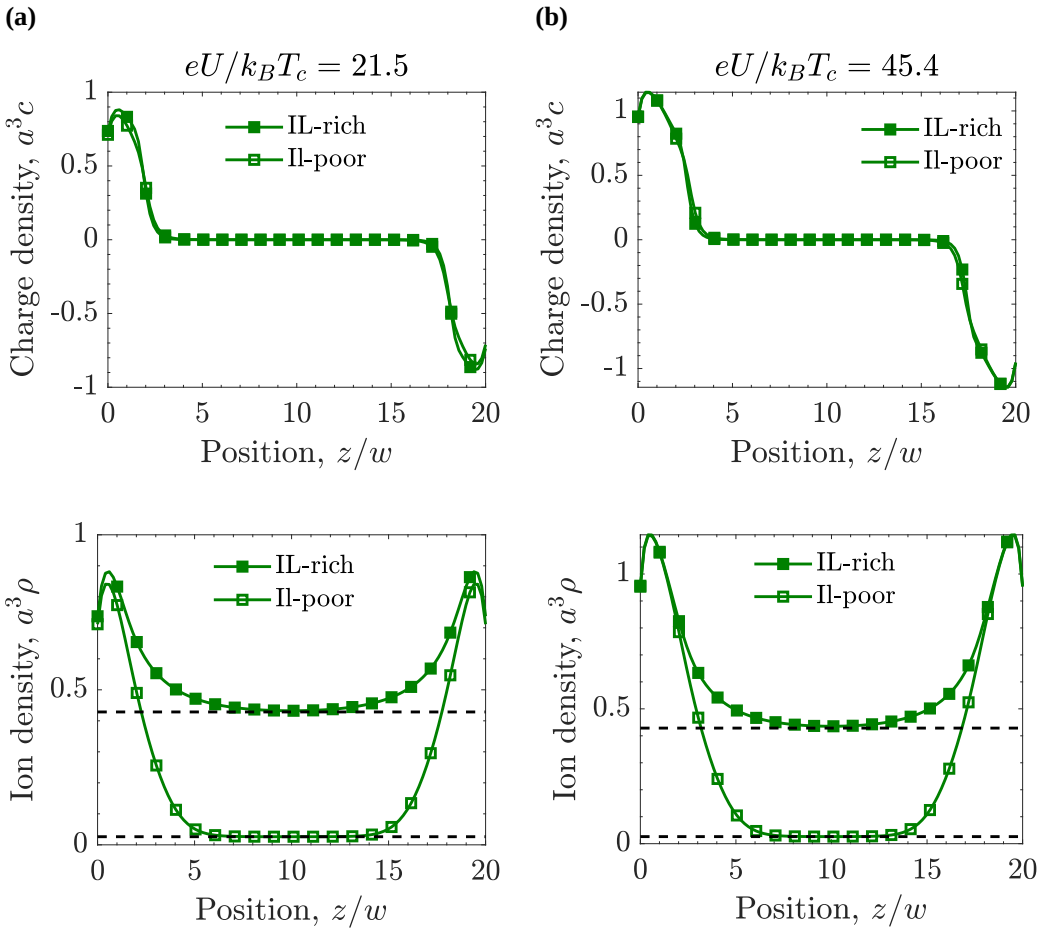

FIGURE 7.14 Charge and ion density profiles at the capillary ionization transition of oppositely charged slit-shaped mesopores. (a) Charge and ion density profiles at $eU/k_BT_c = 21$. **(b)** Charge and ion density profiles at $eU/k_BT_c = 46$. In all the the plots, the chemical potential $\mu/k_BT_c = -4.57$, the temperature $T/T_c = 0.84$, slit width $w = 20a$, and ionophilicity $a^3h_s/\xi_0 = 0.25$, where ξ_0 is the bare correlation length and a the ion diameter. The dashed horizontal lines show the bulk values in the corresponding phases. The filled symbols represent the IL-rich phase while the unfilled symbols denote the IL-poor phase.

favoring the IL-poor phase.

Figure 7.15a shows the differential capacitance. At low temperatures, the system is in the IL-rich region, characterized by a high ion density, and hence, the capacitance has a bell shape. At higher temperatures, the IL-poor phase becomes stable, and the capacitance shape changes to bird-like. Figure 7.15b corresponds to the stored energy in the pore. Since the walls are oppositely charged, the accumulated charge, the differential capacitance, and the stored energy are calculated from $z = 0$ to $z = w/2$. Thus, those characteristics' magnitude is roughly half of the magnitude when the two walls are equally charged.

Finally, since the behavior is similar to the case of walls equally charged, we only present the accumulated charge and the stored energy as a function of the temperature. Figure 7.16 shows the accumulated charge and the stored energy as a function of the temperature for two voltages $eU/k_BT_c = 20$ and $eU/k_BT_c = 45.4$ at which there is a positive and negative magnitude of the

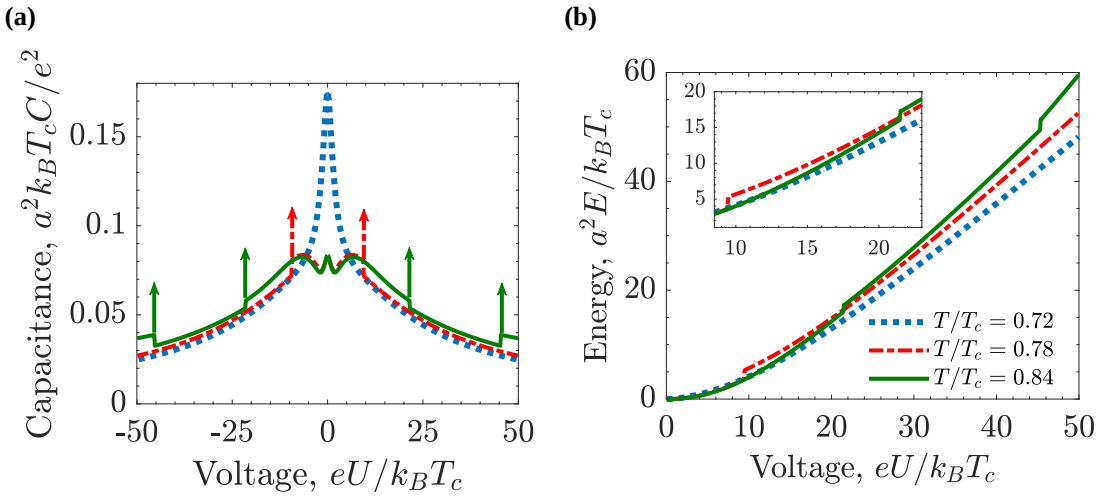

FIGURE 7.15 Differential capacitance and stored energy at the capillary ionization of oppositely charged slit-shaped mesopores. (a) Differential capacitance. The vertical arrows indicate that capacitance diverges at the capillary ionization transition according to the Dirac delta function in Eq. (4.34). **(b)** Stored energy. The chemical potential $\mu/k_BT_c = -4.57$, the pore width $w = 20a$, and ionophilicity $a^3h_s/\xi_0 = 0.25$, where ξ_0 is the bare correlation length and a the ion diameter. In both plots, blue lines denote $T/T_c = 0.72$, red $T/T_c = 0.78$, and green $T/T_c = 0.838$. For typical values of the ion diameter $a = 0.7\,\mathrm{nm}$ and room temperature for T_c, the various units are: thermal voltage $e/k_BT_c \approx 26\,\mathrm{mV}$ for voltage, thermal electric capacitance $e^2/(k_BT_ca^2) \approx 620\,\mu\mathrm{F\,cm^{-2}}$ for capacitance, and $k_BT_c/a^2 \approx 0.84\,\mathrm{mJ\,cm^{-2}} \approx 0.23\,\mathrm{nW\,cm^{-2}}$ for energy.

jump, respectively when the capillary transition occurs.

7.3.1 Integral capacitance for dilute and semi-dilute mixture

In this section, we compute the integral capacitance for small and medium bulk density of ions, ρ_b and different values of ionophilicity, h_s. These results would be useful to compare with the molecular simulation results presented in the next chapter. The integral capacitance is given by

$$C_{int}(U) = \frac{Q}{U} \tag{7.3}$$

Figures 7.17 and 7.18 show the integral capacitance calculated at bulk density $\rho_b = 0.08$ and $\rho_b = 0.17$, respectively, by implementing both approximations for the excluded volume interactions: Carnahan-Starling and lattice-gas. In this case, we have considered temperatures far from coexistence since these results will be useful for comparison purposes with the molecular simulations (presented in the next chapter).

Regarding the behavior of integral capacitance itself, it is important to highlight that, as the differential capacitance, $C_{int}(U)$ exhibits the three different shapes displayed so far, that is, bell-, camel- and bird-like. However, the integral capacitance shape seems to be more sensitive to the entropic approximation chosen, meaning that, under the same set of parameters, integral capacitance displays different forms when implementing CS or lg expressions. Additionally, this trend is consistent with our results in Chapter 6, where we found that, when implementing

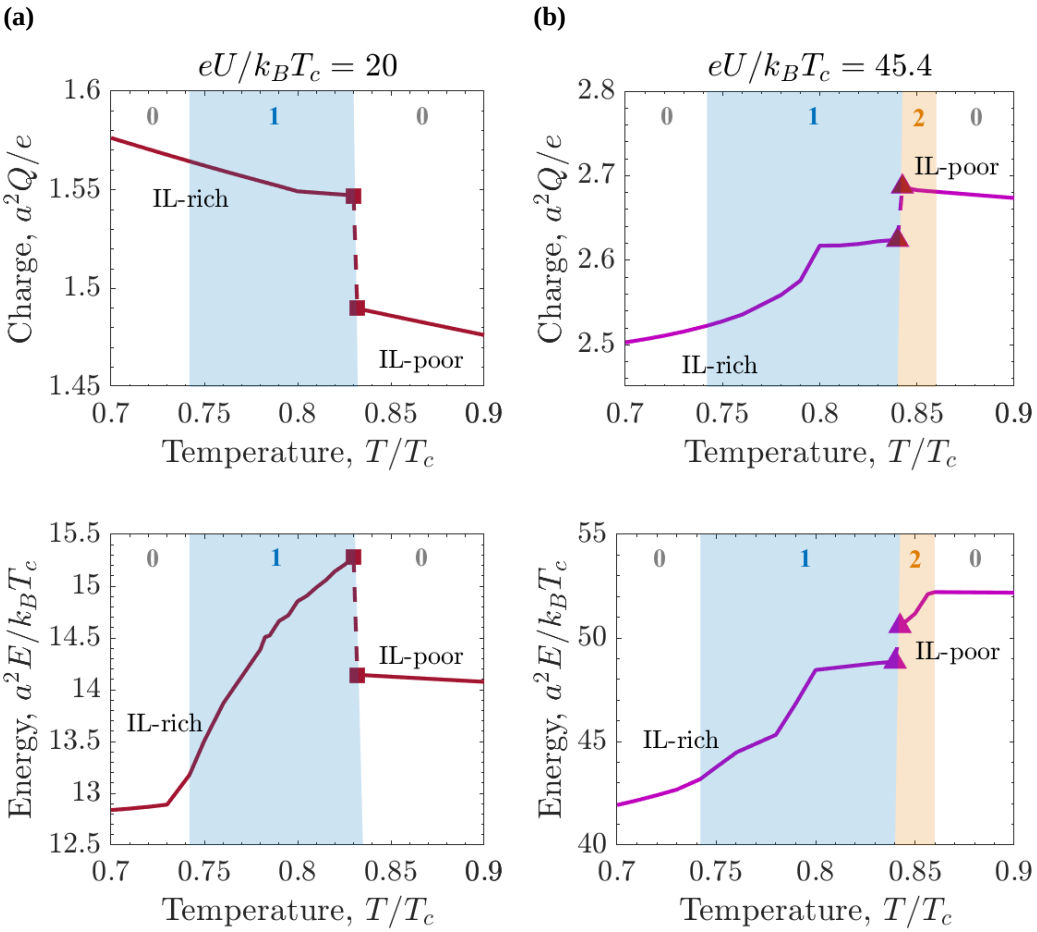

FIGURE 7.16 Accumulated charge and stored energy in oppositely charged slit-shaped mesopores as a function of temperature. **(a)**Accumulated charge (top) and stored energy (bottom) for applied voltage $eU/k_BT_c = 20$. **(b)** Accumulated charge (top) and stored energy (bottom) for applied voltage $eU/k_BT_c = 45.4$. The colored areas show the regions with one and two transitions as indicated by the corresponding numbers. Chemical potential $\mu/k_BT_c = -4.57$, slit width $w = 20a$ and ionophilicity $a^3h_s/\xi_0 = 0.25$, where ξ_0 is the bare correlation length and a the ion diameter.

lg expression, the transformations between the different capacitance shapes are shifted to higher densities with respect to the CS approximation.

For a dilute system with $a^3\rho_b = 0.08$ (see Figure 7.17), the capacitance's shape strongly depends on the ionophilicity. A poorly ionophilic electrode ($a^3h_s/\xi_0 = 0.01$) displays bird-shaped capacitance at every temperature for both CS and lg approximations. However, in the latter case, the displayed "wings" are more prominent. For a stronger ionophilic electrode ($a^3h_s/\xi_0 = 0.2$ and $a^3h_s/\xi_0 = 0.5$), the capacitance shape does not depend on the temperature anymore in the case of the CS expression, and thus, bell-shaped is displayed, implying that more ions are close to the surface electrode independent of the temperature. Therefore, the capacitance has a maximum at PZC and then decreases for increasing voltage. In the case of lg approximation, the bell-like capacitance is the only observed shape, provided the electrode is strongly ionophilic (see Figure 7.17b (bottom)).

For a more concentrated system with $a^3\rho_b = 0.17$ (see Figure 7.18), mostly bell shape is observed with the CS approximation. A smooth bird-shape is displayed only for a poorly

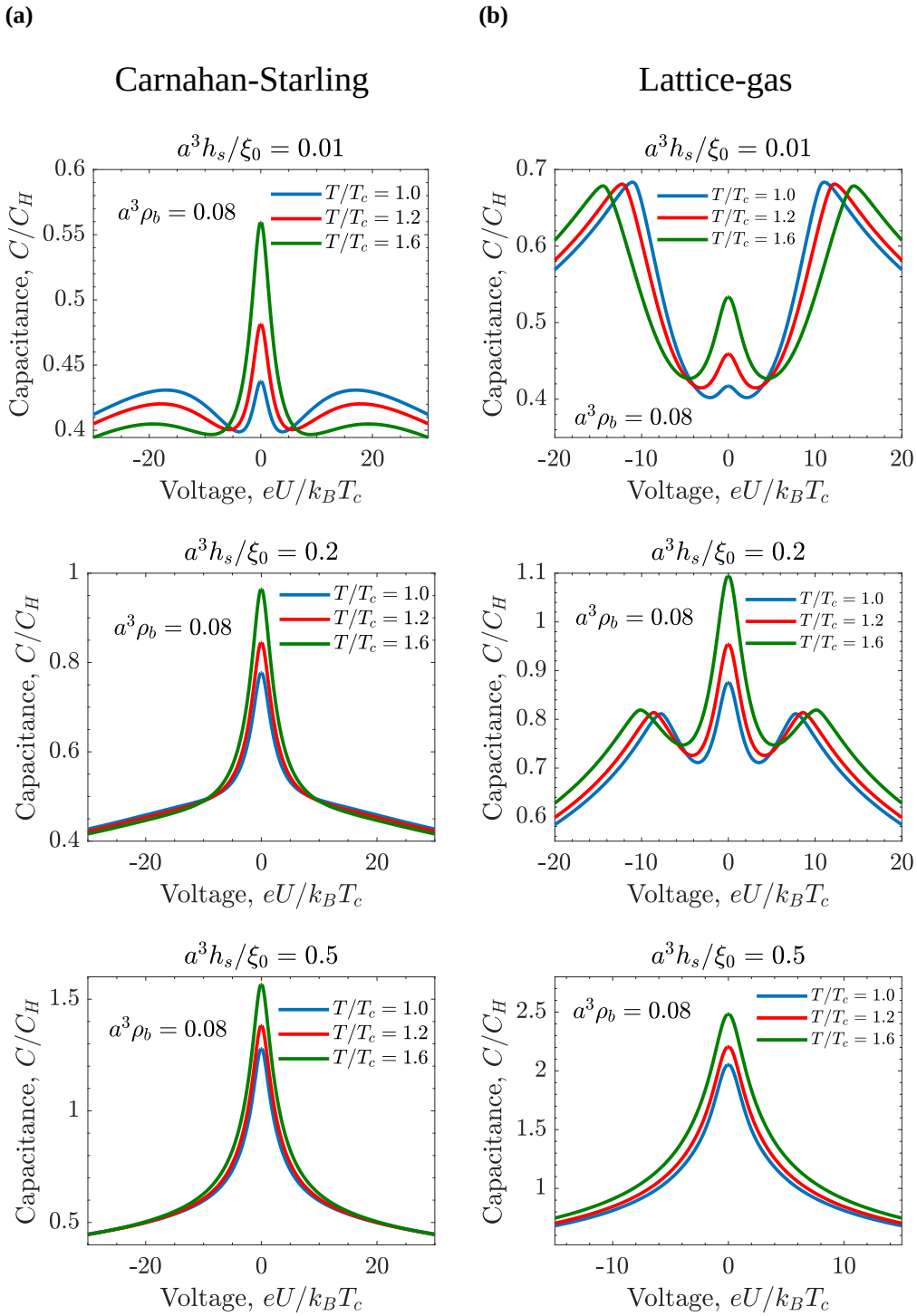

FIGURE 7.17 Integral capacitance of oppositely charged slit-shaped mesopores at bulk density $\mathbf{a^3\rho_b = 0.08}$. (a) Integral capacitance calculated for the Carnahan-Starling (CS) approximation and three different values of ionophilicity: $a^3h_s/\xi_0 = 0.01$ (top), $a^3h_s/\xi_0 = 0.2$ (middle), and $a^3h_s/\xi_0 = 0.5$ (bottom). **(b)** Integral capacitance calculated for the Lattice-gas (lg) approximation and three different values of ionophilicity: $a^3h_s/\xi_0 = 0.01$ (top), $a^3h_s/\xi_0 = 0.2$ (middle), and $a^3h_s/\xi_0 = 0.5$ (bottom). In all the plots, ξ_0 is the bare correlation length and a the ion diameter. Blue lines correspond to temperature $T/T_c = 1.0$, red lines $T/T_c = 1.2$, and green lines denote $T/T_c = 1.6$. The slit width $w = 40a$. The voltage is measured in thermal voltage $e/k_BT_c \approx 26\,\mathrm{mV}$, and capacitance is measured in unit of $C_H = \epsilon_r/4\pi a$.

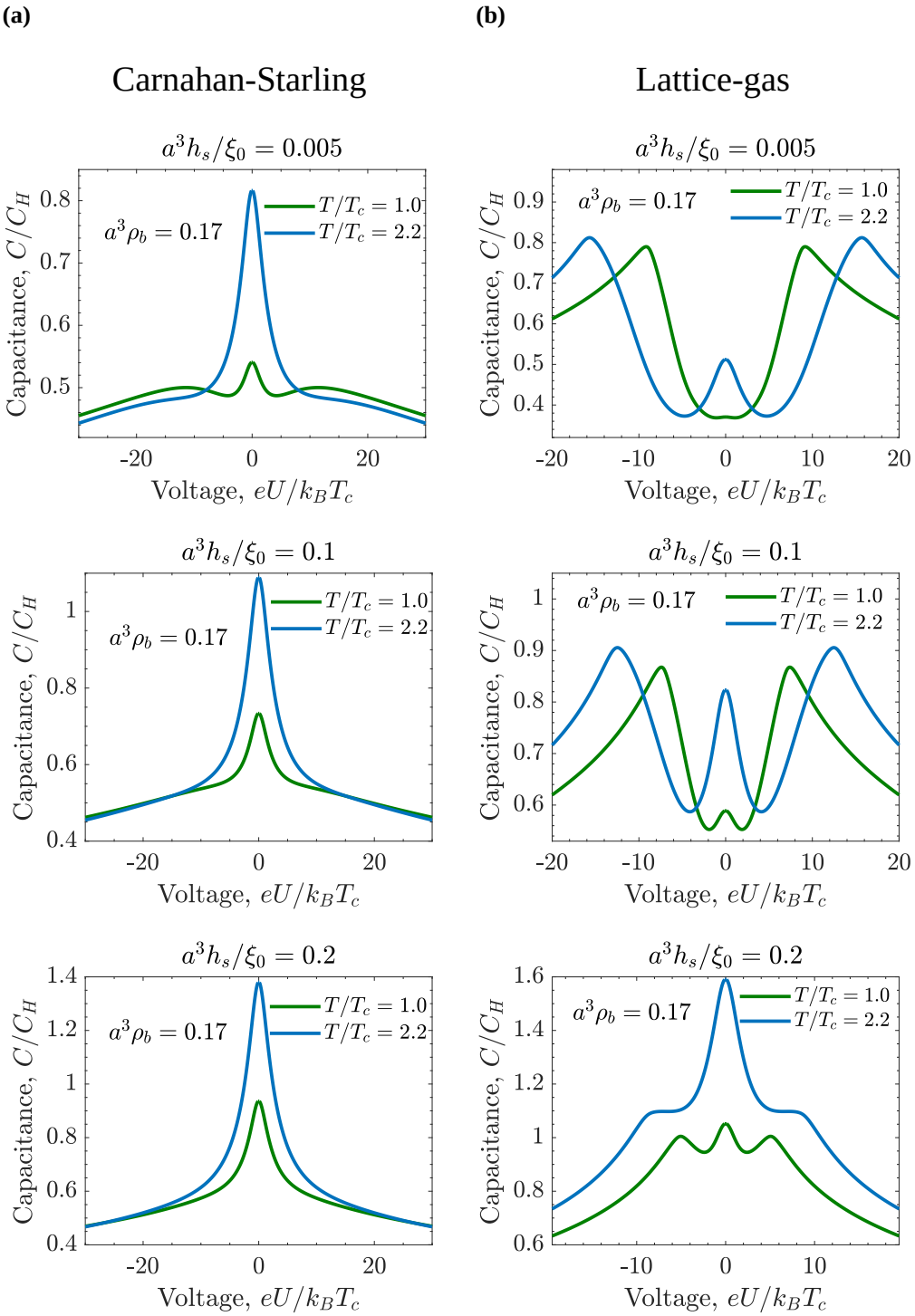

FIGURE 7.18 Integral capacitance of oppositely charged slit-shaped mesopores at bulk density $\mathbf{a^3\rho_b = 0.17}$. (a) Integral capacitance calculated for the Carnahan-Starling (CS) approximation and three different values of ionophilicity: $a^3h_s/\xi_0 = 0.005$ (top), $a^3h_s/\xi_0 = 0.1$ (middle), and $a^3h_s/\xi_0 = 0.2$ (bottom). **(b)** Integral capacitance calculated for the Lattice-gas (lg) approximation and three different values of ionophilicity: $a^3h_s/\xi_0 = 0.005$ (top), $a^3h_s/\xi_0 = 0.1$ (middle), and $a^3h_s/\xi_0 = 0.2$ (bottom). In all the plots, ξ_0 is the bare correlation length and a the ion diameter. Green lines correspond to temperature $T/T_c = 1.0$ and blue lines denote $T/T_c = 2.2$. The slit width $w = 40a$. The voltage is measured in thermal voltage $e/k_BT_c \approx 26\,\mathrm{mV}$, and capacitance is measured in unit of $C_H = \epsilon_r/4\pi a$.

ionophilic electrode and the lowest temperature considered $T/T_c = 1.0$ (Figure 7.18a (top)). In the case of the lg expression, a well-defined bird shape is displayed. However, for the highest temperature and the highest ionophilicity, there is a transition between bird to bell shapes (Figure 7.18b (bottom)).

We finally remark that the capacitance increases as the temperature decreases but only for low values of the electrode's ionophilicity. If the system's concentration is large or the electrodes are strongly ionophilic, this trend is no longer observed, and the capacitance increases as the temperature increases.

Chapter 8

Molecular Simulations

In this chapter, we present results of Molecular Dynamics (MD) simulations of the system under consideration. The results presented are supplementary and support the theoretical results presented in the previous chapters. In Section 8.1 we present a brief description of the computational methods. In Section 8.1.1 we explore the bulk behavior to locate a phase separation. We compare the results with the Hypernetted-chain (HNC) theory. In Section 8.1.2, the studied mixture is confined to a slit-shaped mesopore. We present the comparison between two simulation approaches, constant potential, and constant charge simulations. The integral capacitance and adsorption results are presented in Section 8.1.3. The MD simulations were performed in LAMMPS, and the codes were provided by Prof. Enrique Lomba from the Institute of Physical Chemistry Rocasolano (IQFR) in Madrid.

Molecular simulations have become an essential tool for a wide range of research fields, from self-assembly clusters in colloids to large complex structures such as biological membranes. Computer simulations of molecular systems aim to analyze/understand macroscopic behavior from computing microscopic interactions to get a more in-depth insight into the physical principles underlying various processes. In this sense, molecular simulations have served many purposes, such as interpreting experimental results, understanding fundamental molecular theories providing quantitative estimates of experimental or purely theoretical results, and the capability to extrapolate data to ranges often experimentally inaccessible.

One important aspect when performing molecular simulations is that the reliability of the predictions of molecular simulations relies on the proper choice of the force field for the system of interest. A fundamental problem is how to efficiently sample the configuration space that includes all the possible molecular conformations for the global low energy regions, which a molecular system in thermal equilibrium will populate.

The Molecular Dynamics method is very general, and the basic idea is to solve Newton's equations of motion, $\vec{F}_i = m\vec{a}_i$, that each particle in the system obeys. The interest in MD is

generally focused on two levels: dynamical information since it is possible to collect information about process flow, aggregation, or nucleation rates, calculate diffusion constants or other transport coefficients, or determine the particle's trajectory by keeping track of each simulation step. Additionally, thermodynamic averages imply that the ergodicity hypothesis is assumed to be fulfilled for a sufficient number of particles, meaning that the time average of the simulated system is the same as the ensemble average.

8.1 Model and simulation details

In this section, we analyze the response of the fluid to an external field from an atomistic perspective. To that aim, we have devised a molecular "toy model" composed of three types of equally sized spherical particles, two of them with opposite charges (ions) and a larger number of uncharged particles (solvent). The interactions are described as follows

$$u^{\alpha\beta}(r) = u^{\alpha\beta}_{LJ}(r) + \frac{Z_\alpha Z_\beta e^2}{4\pi\epsilon_0 r} \tag{8.1}$$

where e is the electron charge, $Z_{\alpha(\beta)}$ are the ion charges (in electron units) and ϵ_0 is the vacuum permittivity. The dispersion interactions are represented by truncated and shifted Lennard-Jones potentials of the form

$$u^{\alpha\beta}_{LJ}(r) = \begin{cases} 4\varepsilon\left[\left(\frac{a_{\alpha\beta}}{r}\right)^{12} - \left(\frac{a_{\alpha\beta}}{r}\right)^{6}\right] - 4\varepsilon\left[\left(\frac{a_{\alpha\beta}}{R_c}\right)^{12} - \left(\frac{a_{\alpha\beta}}{R_c}\right)^{6}\right] & \text{if } r \le R_c \\ 0 & \text{if } r \ge R_c \end{cases} \tag{8.2}$$

where R_c is the truncation radius of the dispersive interactions. The energy and length potential parameters are adjusted, together with R_c, to get a mixture that undergoes phase separation under appropriate temperature and density conditions. The pore's confining walls are made up of three graphene layers on each side, which were created using the graphene sheet tool of the VMD package [155]. The atomic positions of each carbon atom in the electrode are assumed fixed during the simulations. From our previous theoretical findings, in this case study we will deal with ionophilic walls. Thus, we have set the wall-ion interactions as attractive and wall-solvent interactions as repulsive. Each carbon atom on the graphene sheets carries a charge defined in terms of the charge surface density or directly by fluctuating charges calculated using a constant potential simulation scheme (we will comment on this later). Coulombic forces were computed using the particle-particle-particle-mesh algorithm (P^3M) [156] with an accuracy of 10^{-8} and slab geometry [157] (except for bulk phases) and an electrostatic cutoff, $R_c^{coul} = 13.5\,\text{Å}$. We have applied standard three-dimensional periodic boundary conditions for bulk simulations, and only in two space directions when dealing with the confined system. The simulations have been carried out using the molecular dynamics package LAMMPS [158]. The simulation time step was set to $1\,\text{fs}$, and temperatures were kept fixed using a Nosé-Hoover thermostat with a relaxation time of $100\,\text{fs}$. Equilibration was achieved after runs of $2\,\text{ns}$ and production runs were $4\,\text{ns}$ long. Averages were performed using 4000 independent configura-

tions along the production run. We implemented real units [1]. However, to compare the capacitance obtained from the theory and simulations, we express the quantities in reduced units. The conversion from real to reduced units is presented in Appendix D.

	+/+	-/-	+-/s	s/s	+-/w	s/w
ε (Kcal/mol)	0.238	0.238	0.238	0.238	0.138	0.075
a (Å)	3.4	3.4	3.4	3.4	3.4	3.8
R_c^{LJ} (Å)	6.0	6.0	6.0	12.0	6.0	4.265
R_c^{coul} (Å)	13.5	13.5	-	-	13.5	-

TABLE 8.1 Potential parameters of the electrolyte mixture and the wall-particle interactions. Solvent interactions are denoted by s, and those that involve wall particles by w.

The set of potential parameters is collected in Table 8.1. The charges of cations are set to $Z_+ = 0.25e$ and $Z_- = -0.25e$ those of anions. The reduction on the ionic charge acts as an effective dielectric constant, which considers that our solvent is apolar (and non-polarizable) and thus does not screen the electric fields. This implies a relative dielectric constant $\varepsilon_r = 16$ for $|Z_\pm| = 1$, or $\varepsilon_r = 64$ for $|Z_\pm| = 2$. Our simulations have been run in the canonical ensemble, and to reproduce bulk conditions in the middle of the pore, we have used relatively large pore widths. We have considered samples of 4184 solvent molecules, and 1038 ions (solvent mole fraction $x_s = 0.8$). Samples with two total densities, $\rho_{tot} = \rho_s + \rho_+ + \rho_-$, $0.022\,\mathrm{molecules/\AA^3}$ and $0.01\,\mathrm{molecules/\AA^3}$ have been simulated, by which the inner graphene layers are placed 136 Å and 166 Å apart, respectively. This corresponds to effective pore widths (space accessible to molecular centers) of 131 Å and 160 Å.

8.1.1 Searching for the demixing conditions

Before the simulations of the confined system, we have to identify the conditions that lead to demixing. A one-to-one comparison with the theory would require a simulation in the Grand Canonical Ensemble (e.g., a Grand Canonical Monte Carlo) since our theoretical calculations have been performed at a constant chemical potential. This would be highly cumbersome from a simulation standpoint since within the density range we are considering, the required insertion moves would have a very low acceptance ratio. We have bypassed this problem to some extent by using large pores, in which the middle region acts as a reservoir of ions where bulk conditions are mostly preserved. Using our theoretical results as a guide, we are looking for conditions of low ionic concentration, which we have kept constant at a mole fraction of $x_i = (\rho_+ + \rho_-)/\rho_{tot} = 0.2$. With the concentration fixed in the canonical ensemble (*i.e.*, total density is also kept constant), one has to lower the temperature and look for a signature of the transition temperature. We have used the Hypernetted Chain (HNC) integral equation to obtain an estimate of the transition. It is well known that for temperatures close to the spinodal

[1] Distance in Å, energies in $\mathrm{kcal/mol}$, pressure in bar, charge in electron units and voltage in V [159].

decomposition line, this equation and most approximations based on the Ornstein-Zernike relation break down [160]. The no-solution boundary of the equation will then provide the sought estimate of the transition temperature. The HNC equation for a homogeneous multicomponent mixture is composed of the Ornstein-Zernike (OZ) relation

$$h_{\alpha\beta}(\mathbf{r_{12}}) = c_{\alpha\beta}(\mathbf{r_{12}}) + \sum_{\lambda} \rho_{\lambda} \int c_{\alpha\lambda}(\mathbf{r_{13}}) h_{\lambda\beta}(\mathbf{r_{32}}) d\mathbf{r_3} \tag{8.3}$$

coupled with the HNC closure

$$h_{\alpha\beta}(r) = \exp\left[-u_{\alpha\beta}(r)/k_B T + h_{\alpha\beta}(r) - c_{\alpha\beta}(r)\right] - 1 \tag{8.4}$$

where the total correlation function is $h_{\alpha\beta} = g_{\alpha\beta} - 1$, being $g_{\alpha\beta}$ the partial pair distribution function between species α and β. The partial direct correlation function, $c_{\alpha\beta}$ is defined by the OZ relation, and in contrast with the pair distribution function, does not diverge (become macroscopically long-ranged) when reaching the critical point. The set of Eqs. (8.3) and (8.4) can be solved iterating back and forward from Fourier space (where Eq. (8.3) is deconvoluted) and taking proper account of the long range of the Coulombic interactions that is directly reflected in the direct correlation functions. The procedure followed here is a generalization to multicomponent electrolytes with soft cores of the code published in reference [161]. After a series of runs, we have delimited the no-solution region of the HNC for our mixture, which we illustrate in Figure 8.1. It is essential to highlight, however, that these curves do not represent a phase diagram. They are an indication that state points close to the shaded areas will have strong concentration fluctuations, and the system will undergo a demixing transition if the state point is shifted into the shaded region.

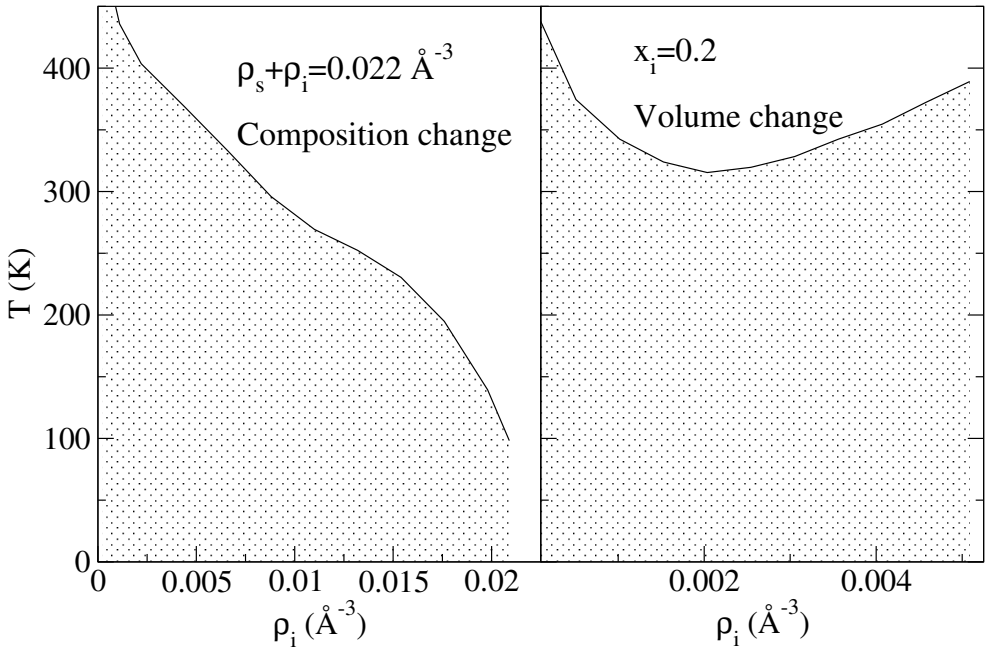

FIGURE 8.1 No-solution region of the HNC equation for our model of electrolyte. On the right are results computed at constant composition and varying total density. On the left results for constant density changing composition.

Next, we wonder to what extent these results are reliable. Aside from the arduous computation of the phase diagram of our system using, e.g., thermodynamic integration or ad hoc simulation techniques [162], we can get a grasp of how close we are to a phase transition by monitoring the evolution of density and concentration fluctuations. Density-density correlations are measured in Fourier space by means of the total structure factor,

$$\begin{aligned} S_{NN}(Q) &= \frac{1}{N}\langle\tilde{\rho}(\mathbf{Q})\tilde{\rho}(-\mathbf{Q})\rangle \\ &= \frac{1}{N}\left\langle\left|\sum_i e^{-i\mathbf{Q}\cdot\mathbf{R_i}}\right|^2\right\rangle \end{aligned} \tag{8.5}$$

where the tilde denotes Fourier transformation, N is the number of particles, $\mathbf{R_i}$ indicates the particle positions, and $\langle\ldots\rangle$ represents an ensemble average. This latter quantity is experimentally accessible from several diffraction techniques (neutron, X-ray scattering, etc.). Its low wave number behavior is directly related to the isothermal compressibility, χ_T,

$$\lim_{Q\longrightarrow 0} S_{NN}(Q) \propto \rho k_B T \chi_T. \tag{8.6}$$

It is known that $S_{NN}(Q \to 0)$ diverges in the case of vapor-liquid transitions. In the case of mixtures, besides density fluctuations, one can also analyze the correlation between concentration fluctuations, which also will diverge at the consolute point. The case of binary liquids is straightforward, and the concentration-concentration structure factor reduces to

$$\begin{aligned} S_{cc}(Q) &= N\langle\tilde{C_\alpha}(\mathbf{Q})\tilde{C_\alpha}(-\mathbf{Q})\rangle \\ &= x_2^2 S_{11}(Q) + x_1^2 S_{22}(Q) - 2x_1x_2S_{12}(Q), \end{aligned} \tag{8.7}$$

where $\tilde{C_\alpha}(\mathbf{Q}) = \tilde{\rho_\alpha}(\mathbf{Q})/\tilde{\rho_{tot}}(\mathbf{Q})$, and $S_{\alpha\beta}(Q)$ are the corresponding partial structure factors, which can be calculated from the expression (8.5) by restricting the summation to the appropriate particle types after expanding the squared term within the average, namely

$$S_{\alpha\beta}(Q) = x_\alpha\delta_{\alpha\beta} + \frac{1}{N}\sum_{i\in\alpha}\sum_{j\in\beta}\exp[-\mathbf{Q}\cdot(\mathbf{R}_i - \mathbf{R}_i)]. \tag{8.8}$$

In our case, we have three components, but since the electroneutrality condition couples anion and cation densities, we can actually consider our system as a binary mixture of ions and solvent as far as concentration fluctuations are concerned. In Figure 8.2a we present the HNC and simulation total and concentration-concentration structure factors when approaching the temperature of demixing. We observe that the theory agrees remarkably well with the simulation, and $S_{cc}(Q \to 0)$ exhibits a clear tendency to diverge when approaching the demixing temperature. The low-Q behavior of S_{NN} is typical of a high-density fluid (low compressibility) away from the liquid-vapor transition.

From the HNC we have estimated the demixing temperature at $\rho_{tot} = 0.022\,\text{Å}^{-3}$ to be

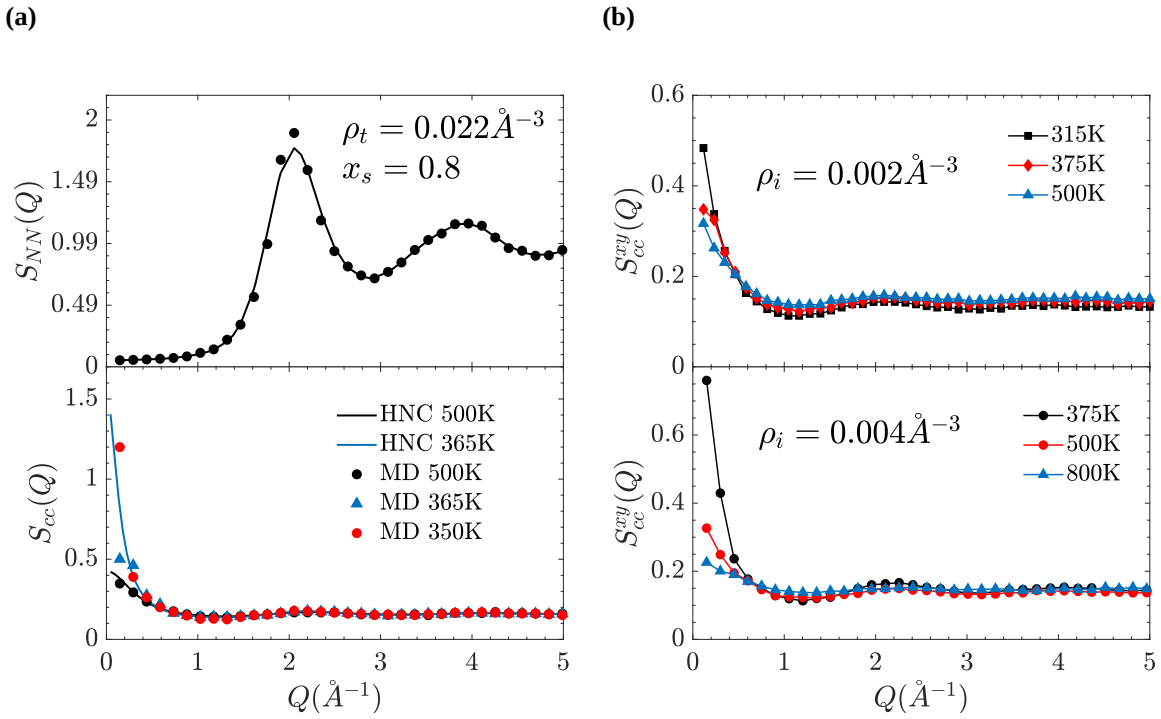

FIGURE 8.2 Structure factors. **(a)** Total and concentration-concentration structure factors when approaching the temperature of demixing computed in the HNC (curves) and obtained from simulation. **(b)** Concentration-concentration structure factor across the periodic dimension when approaching the demixing transition.

360 K, and at $\rho_{tot} = 0.01$ Å^{-3}, 315 K. These will be the values we will be using for the reference temperature corresponding to the vicinity of the demixing transition and denoted by T_c in what follows, although one must bear in mind that the values for the simulated system will be somewhat lower. Finally, we have to consider that the system under consideration is confined in one direction, which has an immediate consequence in the structure factor calculation from simulation because of the loss of periodicity along one of the directions. In this case, we have split the non-periodic dimension into three regions, two of which will be in contact with the walls and one in the center. The latter should practically display bulk behavior. The corresponding structure factors, Eqs. (8.5) and (8.7), will be calculated only over the unconfined directions, (e.g x, y). In Figure 8.2b, we illustrate the behavior of the concentration-concentration structure factors calculated across the periodic dimensions for our confined mixture when approaching the vicinity of the demixing conditions. One can appreciate the considerable increase of the concentration fluctuations. Such an increase can be further visualized for two snapshots taken along simulations in which the walls have already been slightly charged (see Figure 8.3).

Due to the charged walls, cations (violet) are adsorbed preferentially on the anode (left) and anions (blue) on the cathode (right). At 500 K, the pore is more or less uniformly filled with ions associated in dimers and tetramers. As the temperature is lowered, the concentration fluctuations substantially increase. At 300 K, large aggregates appear as a precursor of the full demixing that is likely to occur for sufficiently long times. The qualitative picture provided by the snapshots fits the behavior found in Figure 8.2b for the concentration-concentration structure

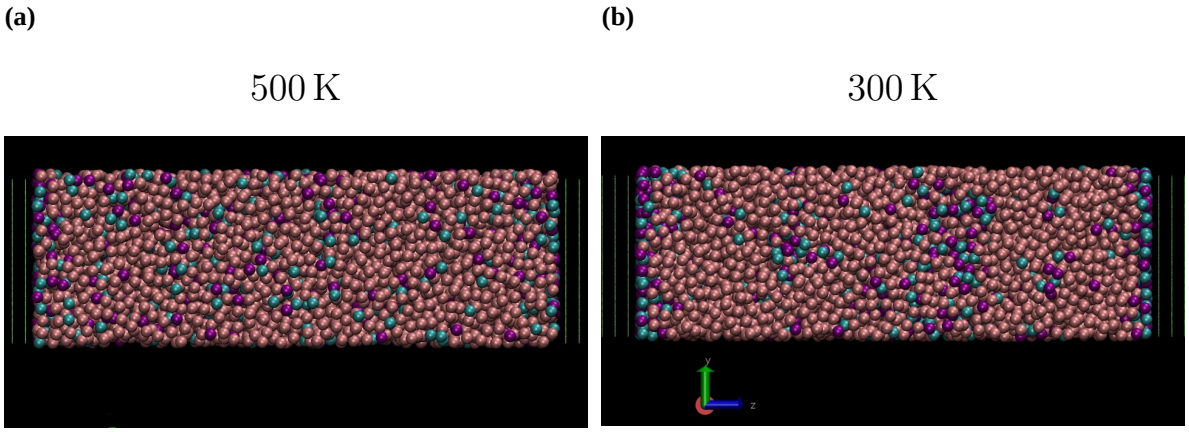

FIGURE 8.3 Snapshots of configurations of simulation run for $\rho_{\mathbf{tot}} = 0.022\,\text{Å}^{-3}$ and $\mathbf{x_i} = \mathbf{0.2}$ when approaching the critical temperature, estimated by the HNC to $360\,\text{K}$. Walls are slightly charged ($\sigma_q = 5.77 \times 10^{-5}\ \text{e/Å}^2$) and some cations (violet) and anions (blue) are adsorbed on them. One can appreciate on the left that most ions are uniformly distributed throughout the pore, whereas at lower temperature there is a visible tendency to form larger aggregates.

factor.

8.1.2 Constant potential vs constant charge simulations

We have run constant potential simulations and compared the results with those of constant charge runs. In the former case, we have used the method proposed by Wang *et al.* [163]. In this approach, which follows the method of Reed, Lanning and Madden closely [164], with corrections from Gingrich and Wilson [165], each charge site in the electrodes is represented by a Gaussian charge distribution of the form

$$\rho_j(\mathbf{r}) = q_j \frac{1}{\eta^3 \pi^{3/2}} \exp[-\eta^2 |\mathbf{r} - \mathbf{r}_j|^2] \tag{8.9}$$

where q_j are the charges on each graphene atom, placed at $\mathbf{r}_j$. The explicit values of q_j are obtained using a variational procedure that minimizes the total electrostatic energy (which includes the energy due to an external potential, U_0) with respect to the charge values at each molecular dynamics step. In this way, the external potential is kept constant. The inverse Gaussian width of the distribution is set to $\eta = 1.979\,\text{Å}^{-1}$ [164]. This procedure is computationally expensive in itself. Additionally, as implemented in [163], one can no longer take advantage of Newton's third law ($\mathbf{f}_{ij} = -\mathbf{f}_{ji}$) when evaluating the forces in a molecular dynamics calculation, which duplicates further the computational burden. On the other hand, constant potential calculations correspond more closely to the physical situation in which a capacitor is connected to an external source, and its plates are kept at a fixed voltage. The method itself allows for a direct calculation of the differential capacitance, in terms of the total charge fluctuation of the electrodes [166] for a fixed number of ions, N, namely

$$C_N^{\delta} = \frac{\langle (\delta Q)^2 \rangle}{k_B T A} + C_0 \tag{8.10}$$

The quantity in brackets corresponds to the charge fluctuation, A is the electrode area, and C_0 is the intrinsic capacitance that can be estimated by fitting the difference between the differential capacitance calculated by numerical differentiation of the surface charge with respect to the potential, and that obtained by Eq. (8.10) with $C_0 = 0$ (see [166]). These methods require incredibly long simulations (over hundreds of nanoseconds), which can only be done with a limited number of particles. As a result, for a fixed number of particles, we decided to calculate the integral capacitance [167].

$$C = \frac{\sigma_q}{\Delta U - \Delta U_{\sigma_q=0}} \tag{8.11}$$

where σ_q is the surface charge density, ΔU is the potential difference between the electrodes, and $\Delta U_{\sigma_q=0}$ corresponds to the neutral case. In our case, we can neglect this latter quantity. Once the density profiles for ions are calculated, the charge density is obtained as $c(z) = Z_+\rho_+(z) + Z_-\rho_-(z)$, from which it is possible to derive the corresponding Poisson potential using the integral form of Poisson's equation [167]

$$u(z) = u(0) - \frac{1}{\epsilon_0}\int_0^z (z - z')c(z')dz' - u_{el}(z) \tag{8.12}$$

We have set the left electrode potential to zero, $u(0) = 0$, and finally, $u_{el}(z)$ is the contribution to the potential derived from the charge distribution of the electrodes. This can be obtained analytically from Eq. (8.9) placing the electrodes perpendicular to the z-axis and integrating over the x, y dimensions. If each electrode is represented by its average surface charge density, $\sigma_q(z_i)$, Poisson's equation in one dimension together with Eq. (8.9) yield

$$u_{el}(z) = \frac{1}{\epsilon_0}\sum_{i=1}^{\text{no.of layers}} \sigma_q(z_i)\left(-\frac{1}{\eta\pi^{1/2}}e^{-\eta^2(z-z_i)^2} - (z - z_i)\left(1 + \text{erf}(\eta(z - z_i))\right)\right) \tag{8.13}$$

being erf(x) the error function. We have performed constant potential simulations with $\Delta U = 1$V and, $\rho_{tot} = 0.022\,\text{Å}^{-3}$ and $500\,\text{K}$. With the charge density profiles, we have solved Eq. (8.12) as a consistency check. Additionally, the average surface charge densities of each graphene layer, $\sigma_q(z_i)$ have been used later to run constant charge simulations. To that aim, all $\sigma_q(z_i)$ belonging to the anode/cathode have been added and assigned to the inner graphene layers or the corresponding anode and cathode in the constant charge simulation, keeping the charge uniformly distributed over the atoms. In Figure 8.4 we summarized the results of comparing constant potential and constant charge simulations.

The top graphs illustrate the density profiles of ions and solvent, clearly showing the preference of ions for the walls. The profiles reach bulk values rapidly. We have approximately a region of 25 molecular diameters around the pore center where the system displays bulk behavior. For our purposes, then a large portion of the pore can act as an ion reservoir. On the middle graphs, we have the charge density, $c(z)$, and integrated charge density,

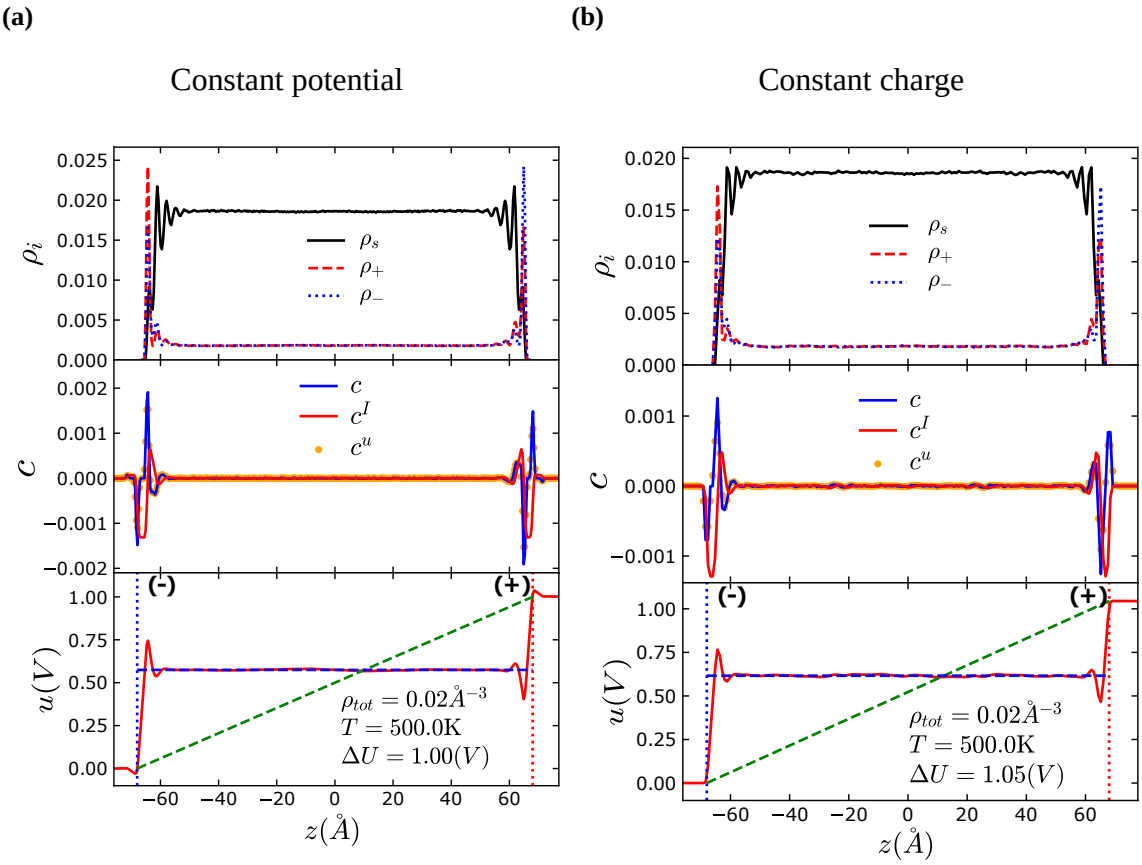

FIGURE 8.4 Density profiles, integrated charge density and Poisson potential. Density profiles (upper graphs), integrated charge density (middle graphs) and Poisson potential (bottom graphs) obtained from **(a)** the constant potential and **(b)** constant charge simulations. The green dashed lines correspond to the voltage consistent with an uniform field in a dielectric medium.

$$c^I(z) = \int_{-w/2}^{z} \left(Z_+\rho_+(z') + Z_-\rho_-(z')\right) dz' \tag{8.14}$$

The perfect screening of the electrodes after the first ionic layers is evidenced. In addition, as a consistency check, we show the charge density obtained from the differential Poisson's equation $c^u = \epsilon_0 \nabla^2 u(z)$, which agrees with the simulated quantity. Differences in the charge density in the vicinity of the electrode's position result from the fact that for constant potential simulations, charges are spread over the three graphene layers, while in constant charge simulations, they are concentrated in the inner layers. In the lower graphs, we illustrate the Poisson's potential, and in the case of constant potential simulations, it can be appreciated that the input $\Delta U = 1$V is exactly recovered at the boundaries. The constant charge simulation with the appropriate electrode surface charge densities exhibits a five percent departure in the computed Poisson potential. The value obtained corresponds to the potential difference between the inner electrodes in the constant potential simulation. We can conclude that both simulation approaches lead to consistent results for the voltage values of interest to us, and the lower the voltage or electrode charge, the better the agreement. Consequently, for our study, we will restrict ourselves to the constant charge molecular dynamics approach.

8.1.3 Integral capacitance and adsorption

We have run several series of constant charge simulations, in which charges were added to the inner layers of the graphene electrodes, ranging from $2 \times 10^{-4}\mathrm{e/atom}$ to $2 \times 10^{-3}\mathrm{e/atom}$, for both the low and moderate ionic concentration case. When comparing theory and simulations, we must readjust the Bjerrum length used in the theoretical model. If we recall that this quantity is given by $\lambda_B = e^2/(4\pi\epsilon_0\epsilon_r k_B T)$ [2], in our case where $\epsilon_r = 16$ to account for the scaling of the charges, we get $\lambda_B = 10425.0/T(K)$ Å (hence $\lambda_B(315\,\mathrm{K}) = 33.095\,\text{Å}$ and $\lambda_B(360\,\mathrm{K}) = 28.95\,\text{Å}$). In the theoretical calculations we have assumed $\lambda_B/a = \lambda_B^c(T_c/T)$. When making comparisons, we will use reduced quantities, by which all densities will be scaled with the molecular diameter ($a^3\rho$). Thus, our system for $\rho_{tot} = 0.022\,\text{Å}^{-3}$ corresponds to a reduced ionic density $a^3\rho_i = 0.17$, and the dilute system $\rho_{tot} = 0.01\,\text{Å}^{-3}$ to $a^3\rho_i = 0.08$. Concerning the capacitance and voltage, we will use thermally scaled quantities, namely C/C_H, with $C_H = \epsilon_r/(4\pi a)$ and eU/k_BT_c. The ionophilicity, h_s, was tuned to account for the average attraction (potential energy) of the ions due to the sole contribution of the walls.

For the dilute system (with $a^3\rho_i = 0.08$), the integral capacitance displays, at every temperature, a bird-shaped capacitance as appreciated in Figure 8.5b. Although the camel-like capacitance is a signature of dilute systems, this shape is not displayed since the electrode is strongly ionophilic. Thus, the capacitance shape exhibits a peak at PZC regardless of the low bulk density. Additionally, it is worth noting that, as found in previous chapters, capacitance increases as the temperature is lowered towards the demixing transition. In Figure 8.5b, we observe that the simulation results reproduce the trends predicted by the theory. One can see a substantial capacitance increase when approaching the demixing temperature, in fact, more significant than that found by the theory. One also observes that the maximum in the capacitance at low voltages, close to the PZC, is less visible in both theory and simulation for the highest temperature. However, in the latter instance, there are substantial statistical uncertainties to allow for solid conclusions.

For the more concentrated system with $\rho_i a^3 = 0.17$, Figure 8.5c shows that at the highest temperature, the integral capacitance displays a peak at the PZC and then decreases as the voltage increases exhibiting a bell-shaped curve. When approaching demixing, capacitance again increases due to the voltage-induced increase of ion density at the surface vicinity, meaning that both cations and anions are adsorbed into the surface layer, leading to a higher capacitance. For higher voltages, capacitance decreases monotonously. On the other hand, in Figure 8.5d, we see that simulation results are affected by very large statistical uncertainties. Therefore it is not possible to draw any conclusion concerning the shape of the capacitance curve. Close to demixing, there is a peak at PZC and two maxima at $eU/k_BT_c \approx 15$, in qualitative agreement with the theory. In any case, when comparing with the low-density results of Figures 8.5a and 8.5b, one observes that the capacitance increase is approximately four times larger in that case for the simulation results. The theoretical curves show the same

[2] This expression is written in standard units. However, in Chapter 4, the Bjerrum length was written in Gaussian units with $4\pi\epsilon_0 = 1$.

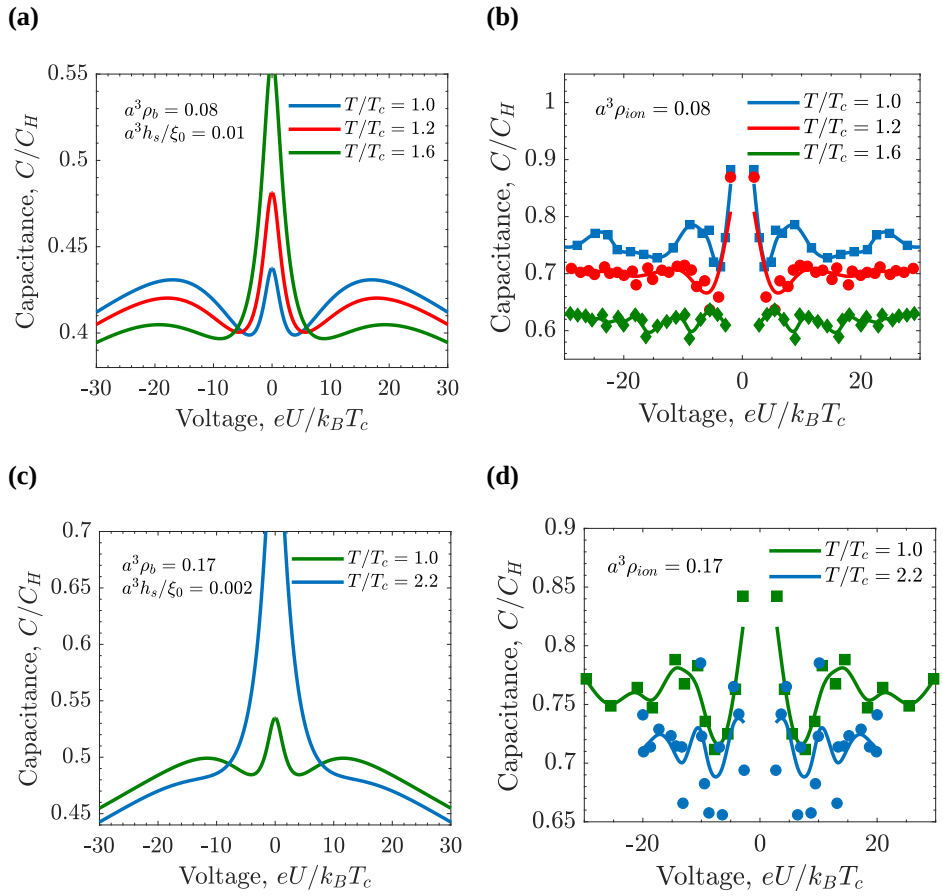

FIGURE 8.5 Integral capacitance. **(a)** Computed from the theory at bulk density $a^3\rho_i = 0.08$, ionophilicity $a^3h_s/\xi_0 = 0.01$, where ξ_0 is the bare correlation length, a the ion diameter, slit width $w = 40a$. **(b)** Computed from MD simulations at ion density $a^3\rho_{ion} = 0.08$. In panels (a) and (b), blue lines correspond to temperature $T/T_c = 1.0$ ($\lambda_B/a = 3.309$), red lines correspond to temperature $T/T_c = 1.2$ ($\lambda_B/a = 2.78$), and green lines denote $T/T_c = 1.6$ ($\lambda_B/a = 2.085$). **(c)** Computed from the theory at bulk density $a^3\rho_i = 0.1$, ionophilicity $a^3h_s/\xi_0 = 0.002$, where ξ_0 is the bare correlation length, a the ion diameter, slit width $w = 40a$. **(d)** Computed from MD simulations at ion density $a^3\rho_{ion} = 0.17$. In panels (c) and (d), green lines correspond to temperature $T/T_c = 1.0$ ($\lambda_B/a = 2.978$), and blue lines denote $T/T_c = 2.2$ ($\lambda_B/a = 1.303$).The capacitance is measured in unit of C_H.

trend, although in a less pronounced fashion. From this comparison, it is tempting to conclude that, for $\rho_i a^3 = 0.17$ the system is approaching the threshold of the region where capacitance grows with increasing temperature.

Finally, we analyze how the ionic density and the proximity to the demixing temperature affect the electrolyte adsorption onto the electrodes. For this purpose, we have calculated the adsorption coefficient as

$$\Gamma = \int_0^{w/2} \left(\rho_+(z) + \rho_-(z) - \rho_i^{\text{bulk}}\right) dz, \tag{8.15}$$

where $\rho_i^{\text{bulk}} = \langle \rho_+(w/2) + \rho_-(w/2) \rangle$, meaning that Γ measures the excess of ions over the bulk value (determined at the center of the pore for sufficiently large pores) due to the presence of the electrodes and the electrode charge.

The adsorption is plotted in Figure 8.6 as a function of the potential (in thermal units) scaled with the respective ion densities and ion diameter. From this figure, it is possible to visualize the temperature effect on the concentration, removing the sheer effect of the higher ion concentration in the system. Results for the denser system are depicted in the upper graph. For the higher ionic concentration, we observe that the voltage dependence is minimal for high temperatures. When approaching demixing, the adsorption decreases with increasing potential. In addition, by reducing the temperature by a factor of two, adsorption is increased in the same proportion. In the dilute system, we see that the voltage dependence of adsorption is almost negligible at high temperature; however, when approaching the spinodal decomposition temperature, there is a 30% rise in adsorption when voltage is increased up to $eU(k_BT_c) \approx 30$. At high voltage and low temperature, electrostatic energy dominates. When comparing the bulk ionic concentration for our two systems, there is a factor two, whereas the charge density of the dilute system near the electrode is nearly eighty percent that of the more concentrated one. Away from demixing, the ratio between bulk ionic concentrations and charge density equals two in both instances. In the low-density case, it is easy to increase the near-electrode charge by adding counterions. However, it may be easier to increase the near-electrode charge in the higher density case by removing coions. In the first case, the adsorption increases, but in the second case, it decreases. This explains the qualitatively different behavior displayed by the dilute system at low temperatures and why the scaled adsorption at high temperatures is almost independent of voltage.

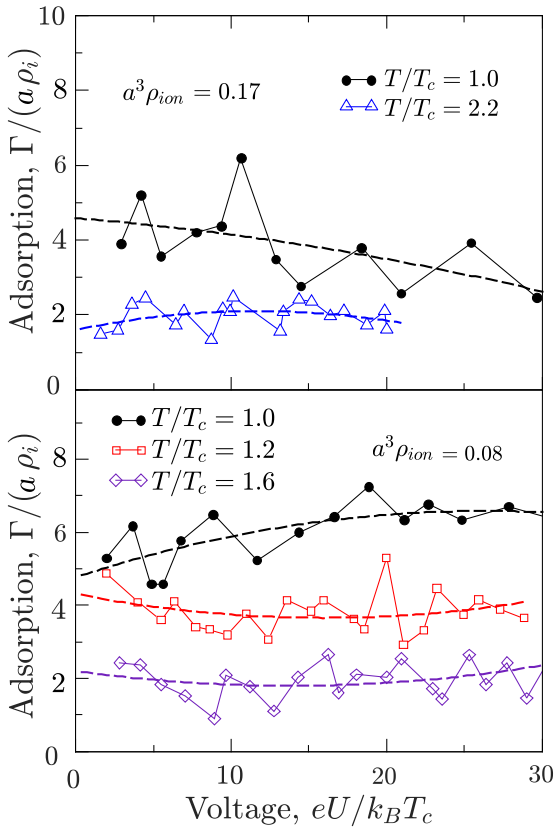

FIGURE 8.6 Capillary ionization of slit mesopores in the chemical potential-temperature plane. The black solid line denotes the bulk coexistence (at μ_{sat}) that ends at the critical point, while the solid blue line is the capillary ionization curve obtained from the Kelvin equation (Eq. (3.10)).

Chapter 9

Conclusions

This thesis studied electrical double layers with ionic liquid–solvent mixtures close to demixing under two confinement forms. Upon demixing, the mixture can separate into a phase rich in ions, called IL-rich, and a phase rich in the solvent called IL-poor phase (Figure 4.2). We proposed a mean-field model suitable to describe the system (Chapter 4). In particular, we considered the cations and anions to be of the same size, the dielectric constant as temperature- and position-independent. Additionally, we treated the hard-core interactions on the level of the local-density approximation.

In the first case of confinement (Chapter 6), we studied an IL-solvent mixture in contact with a single planar electrode. We considered the Carnahan-Starling (CS) and lattice-gas expressions for the excess free energy associated with the excluded volume interactions. We solved this model analytically and numerically, and the results can be summarized as follows.

- Analytic expressions were obtained by using perturbation expansion, which provides good agreement with the numerical results for the charge density at low potentials (Figure 6.2). Likewise, we determined the capacitance shapes (at low potentials) and calculated the capacitance diagrams analytically, showing the regions in which positive (camel shaped) and negative curvatures are displayed. The transformation between the camel- and bell-like shapes can be induced by changing the ion density and temperature (Figure 6.3).
- The numerical calculations revealed the emergence of a *bird*-shaped capacitance which exhibits three peaks as a function of voltage (Figure 6.5). We also calculated the capacitance diagrams where we showed the regions with the camel, bird, and bell shapes, obtained by changing the electrode's ionophilicity and bulk ion density at different fixed temperatures (Figure 6.6).
- Interestingly, when we consider the Carnahan-Starling free energy, the camel-shaped capacitance, which is a signature of dilute electrolytes, can be displayed at high densities in the case of ionophobic electrodes. However, when implementing the lattice-gas entropy, the camel-like capacitance is not displayed in the high-density regime.
- We found that a transformation between the bell and bird shapes can be caused by varying temperature (Figure 6.7) due to voltage-induced adsorption of an IL at an electrode, as manifested by the charging parameter X_D (Figures 6.8c and 6.8d), which shows a strong

peak at a non-zero voltage. Such an enhanced electrosorption leads to stronger screening and hence to the appearance of wings in the bell-shaped capacitance.

- We calculated the energy stored in an EDL at different temperatures (Figures 6.8a and 6.8b). For the CS entropy, the energy increases when approaching demixing, which can be used to generated electricity from heat [15, 131, 151–154]. For the lattice-gas model, however, there seems to be no energy enhancement when approaching demixing. This suggests that the type of solvent (particularly the size of solvent molecules) can play an important role in energy storage. It will be interesting to study such solvent-dependent effects in more detail in future work.

Although we presented a simple model with a number of simplifying assumptions, and more detailed and realistic models, or simulations, will alter, from a quantitative point of view, the results of our calculations, we reasonably expect that our model still captures the qualitative behavior and provides the basis for further studies of electrical double layers in the vicinity of ionic liquid–solvent demixing. It would be interesting to validate our predictions by more rigorous theories, simulations, and experiments, especially those obtained at high ion concentrations at which the local density approximation is known to be inaccurate [168]. However, it is worth noting that our simulation results confirmed the main theoretical findings, and we will comment on this latter.

In the second case, we studied ionic liquid-solvent mixtures in slit-shaped nanopores (Chapter 7). We considered the Carnahan-Starling (CS) for the excess free energy associated with the excluded volume interactions. To solve the model numerically, we implemented a finite differences (FD) scheme. The results obtained are summarized next.

- For non-polarized mesopores, we computed the capillary ionization transition curve and plotted it against the bulk phase diagram to show the coexistence shift when the system is confined (Figure 7.1). Additionally, we estimated the location of the capillary transition by implementing the Kelvin equation and obtained a good agreement with our numerical solution.
- We revealed that a pore could become spontaneously ionized as a function of temperature, slit width, or applied voltage, as manifested by a jump in the amount of an ionic liquid adsorbed in the pore (Figures 7.2 and 7.4).
- Voltage-induced capillary-ionization transition exhibits a re-entrant behavior and creates jumps in the accumulated charge and stored energy. Although in real porous electrodes with a pore-size distribution, these jumps will be averaged out, the possibility to obtain a sudden increase in the stored energy by minute changes of voltage or temperature is spectacular. It may be used to boost energy storage or generate electricity from waste heat (Figure 7.4).
- We analyzed the re-entrant behavior (*i.e.* a second capillary transition at higher voltages) from the density profiles (Figure 7.5) and found that at high voltages, the thermodynamic state is determined by the in-pore bulk region, and the IL-poor phase is favored.

- We studied the influence of the slit width and electrode's ionophilicity in the energy storage. We found that the stored energy decreases as the ionophilicity increases since a strong ionophilic electrode displays the bell-like capacitance that exhibits a maximum at PZC and rapidly decreases as the voltage increases (Figure 7.10). Regarding the slit width, the stored energy decreases when the slit becomes wider. In a wider slit, the ion-wall interactions become weaker since the ions are distributed in a wider space, and then, the accumulated charge decreases. Additionally, we note that the dependence on the slit width w is only when $w < 2\lambda_D$.
- We calculated the integral capacitance for oppositely charged electrodes and different bulk densities (Figures 7.17 and 7.18) and found that integral capacitance displays, as the differential capacitance does, the three different shapes: camel, bird, and bell shapes.

Concerning the molecular simulations (Chapter 8), we have studied the concentration fluctuations of a simple electrolyte model consisting of two charged Lennard-Jones spheres in a solution of an uncharged Lennard-Jones liquid confined by parallel graphene layers as electrodes. Using constant potential molecular dynamics simulations and several constant charge simulations, we have analyzed the effect of the proximity to the demixing transition on the electric double layers and, as predicted by the theoretical results, we have confirmed the existence of two relevant trends in the response of capacitance to concentration fluctuations: in dilute systems, capacitance increases as the demixing temperature is approached, and when the ionic concentration increases this effect tends to become less and less apparent, until the opposite behavior takes over. Additionally, we have found that the "bird-like" capacitance, predicted by our theory, appears when LJ interactions are taken into account and may lead to phase separation. Finally, we have calculated the adsorption (Eq. (8.15)) that provides a structural explanation of the effects observed on the capacitance.

Appendix A

Second-order perturbation expansion

In the frame of the standard perturbation expansion procedure presented in Chapter 5, the solutions of the electrostatic potential and the order parameter were assumed: $u = u_0 + \varepsilon u_1 + \varepsilon^2 u_2 + ...$ and $\phi = \phi_0 + \varepsilon\phi_1 + \varepsilon^2\phi_2 + ...$, for the electrostatic potential,u, and the order parameter ϕ, respectively, where ε is a small parameter.

In the first order approximation, we obtained Eqs. (5.11) and (5.12), with their respective solution given by Eqs. (5.14) and (5.15). In the second-order expansion, we obtained Eqs. (5.17) and (5.16), their respective solutions are given as follows

$$\begin{aligned} u_2(z) = &\frac{eUh_s}{k_BT_c\lambda_D^2\bar{\rho}_b(\xi_0^{-1}+\xi^{-1})(2\lambda_D^{-1}\xi^{-1}+\xi^{-2})}\exp(-z(\lambda_D^{-1}+\xi^{-1})) \\ &- \frac{eUh_s}{k_BT_c\lambda_D^2\bar{\rho}_b(\xi_0^{-1}+\xi^{-1})(2\lambda_D^{-1}\xi^{-1}+\xi^{-2})}\exp(-z/\lambda_D) \end{aligned} \tag{1}$$

$$\begin{aligned} \phi_2(z) = &\left[-\left(\frac{2\lambda_D^{-1}+\xi_0^{-1}}{\xi_0^{-1}+\xi^{-1}}\right)\left(\frac{\xi_0^{-2}\bar{T}eU^2}{2(k_BT_c)^2(\xi^{-2}-4\lambda_D^{-2})}\right)\right. \\ &\left. -\left(\frac{2\xi^{-1}+\xi_0^{-1}}{\xi_0^{-1}+\xi^{-1}}\right)\left(\frac{\xi_0^{-2}\bar{T}A(\bar{\rho}_b)}{6\bar{\rho}_b\xi^{-2}}\right)\left(\frac{h_s}{\xi_0^{-1}+\xi^{-1}}\right)^2\right]\exp(-z/\xi) \\ &+\frac{\xi_0^{-2}\bar{T}eU^2}{2(k_BT_c)^2(\xi^{-2}-4\lambda_D^{-2})}\exp(-2z/\lambda_D)+\frac{\xi_0^{-2}\bar{T}A(\bar{\rho}_b)}{6\bar{\rho}_b\xi^{-2}}\left(\frac{h_s}{\xi_0^{-1}+\xi^{-1}}\right)^2\exp(-2z/\xi) \end{aligned} \tag{2}$$

where

$$A(\bar{\rho}_b) = \bar{\rho}_b^2\left.\frac{\partial^2\bar{\mu}_{ex}}{\partial\bar{\rho}^2}\right|_{\bar{\rho}=\bar{\rho}_b} - 1. \tag{3}$$

Then, the final expressions of the electrostatic potential and the order parameter are

$$u(z) = \frac{eU}{k_B T_c}\exp(-z/\lambda_D) - \frac{eUh_s}{k_B T_c \lambda_D^2 \bar{\rho}_b(\xi_0^{-1}+\xi^{-1})(2\lambda_D^{-1}\xi^{-1}+\xi^{-2})}\exp(-z/\lambda_D) + \frac{eUh_s}{k_B T_c \lambda_D^2 \bar{\rho}_b(\xi_0^{-1}+\xi^{-1})(2\lambda_D^{-1}\xi^{-1}+\xi^{-2})}\exp(-z(\lambda_D^{-1}+\xi^{-1})) \quad (4)$$

$$\phi(z) = \left[\frac{h_s}{\xi_0^{-1}+\xi^{-1}} - \left(\frac{2\lambda_D^{-1}+\xi_0^{-1}}{\xi_0^{-1}+\xi^{-1}}\right)\left(\frac{\xi_0^{-2}\bar{T}eU^2}{2(k_B T_c)^2(\xi^{-2}-4\lambda_D^{-2})}\right) - \left(\frac{2\xi^{-1}+\xi_0^{-1}}{\xi_0^{-1}+\xi^{-1}}\right)\left(\frac{\xi_0^{-2}\bar{T}A(\bar{\rho}_b)}{6\bar{\rho}_b\xi^{-2}}\right)\left(\frac{h_s}{\xi_0^{-1}+\xi^{-1}}\right)^2\right]\exp(-z/\xi) + \frac{\xi_0^{-2}\bar{T}eU^2}{2(k_B T_c)^2(\xi^{-2}-4\lambda_D^{-2})}\exp(-2z/\lambda_D) + \frac{\xi_0^{-2}\bar{T}A(\bar{\rho}_b)}{6\bar{\rho}_b\xi^{-2}}\left(\frac{h_s}{\xi_0^{-1}+\xi^{-1}}\right)^2\exp(-2z/\xi) \quad (5)$$

Appendix B

Calculation of the capillary ionization transition

For the studied system, let us consider the bulk phase diagram shown in Figure B.1. In order to obtain the capillary ionization transition line, the chemical potential is varied within the spinodal region (shown by red arrows), where the grand potential exhibits two minima along a fixed temperature line. Then, Eqs. (5.25)-(5.26) are solved to obtain the electrostatic potential, $u(z)$, and the order parameter, $\phi(z)$, profiles. The grand potential is calculated by inserting $u(z)$ and $\phi(z)$ into Eq. (4.17), and two solutions are obtained, denoting the IL-rich and IL-poor phases. The intersection point between both branches of the grand potential indicates the chemical potential at the capillary ionization transition, μ_{ci}.

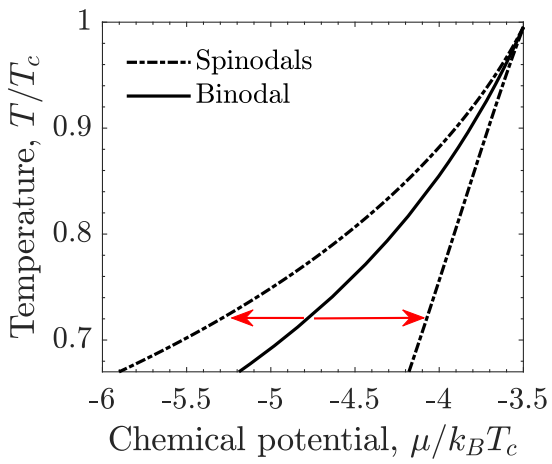

FIGURE B.1 Phase diagram in the temperature-chemical potential plane, illustrating the spinodal region in which the grand potential has two minima.

To illustrate how we obtained the capillary ionization curves, consider the phase diagram in Figure 7.4a. For instance, at $T_{ci}/T_c = 0.838$, there are two capillary transitions (re-entrant behavior described in Chapter 7). Figure B.2a shows the grand potential curve as a function of the chemical potential at $T_{ci}/T_c = 0.838$ for two different voltages $eU/k_BT_c = 21$ (top) and $eU/k_BT_c = 46$ (bottom). The intersection point corresponds to $\mu_{ci}/k_BT_c = 4.57$ at which capillary ionization occurs in both voltages.

Likewise, it is possible to obtain the capillary ionization curve by looking at the grand potential branches' intersection as a function of the temperature or the applied voltage. In fact,

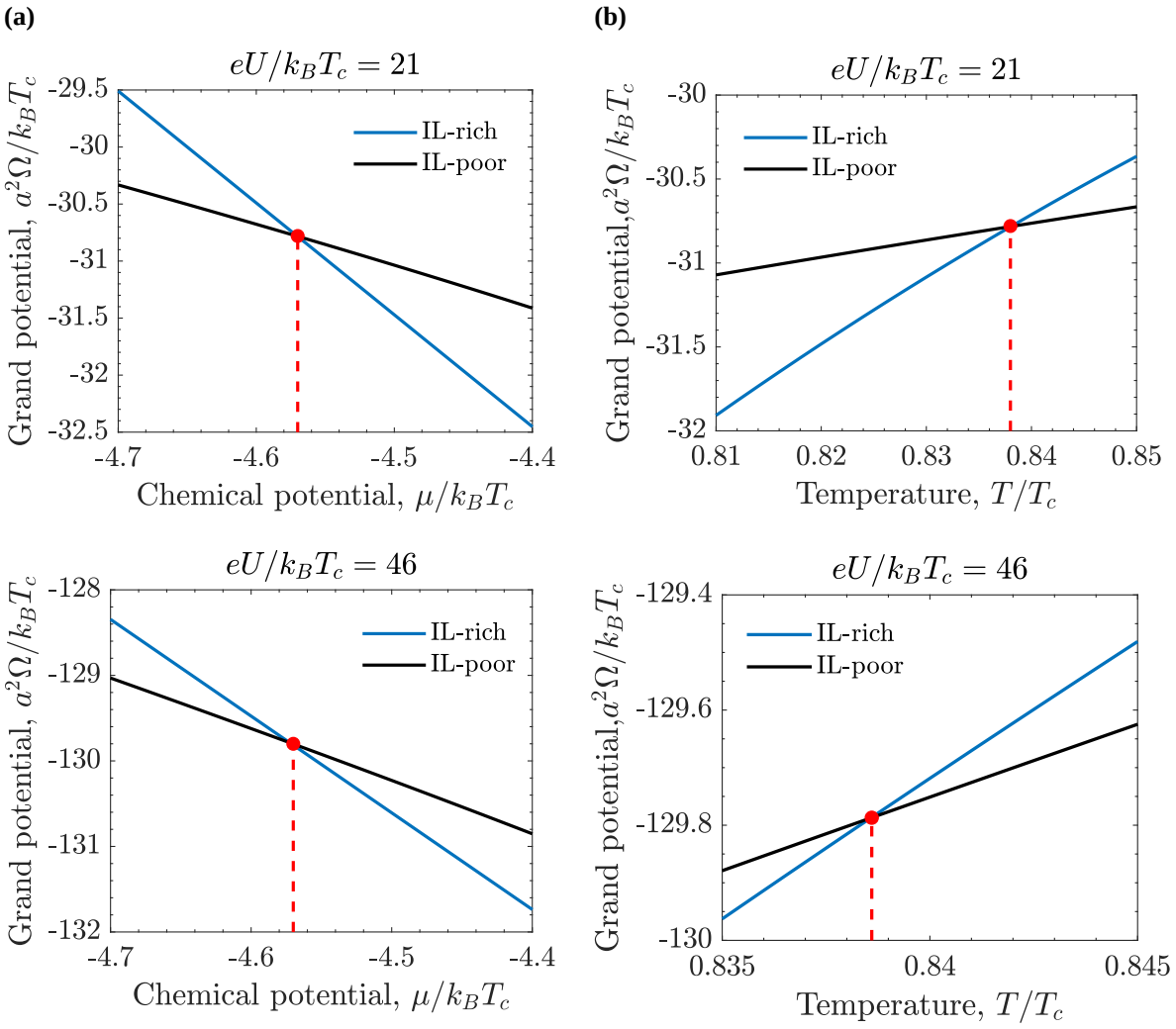

FIGURE B.2 Grand potential as a function of the chemical potential and temperature. **(a)** Grand potential as a function of the chemical potential at fixed temperature $T_{ci}/T_c = 0.838$ calculated at two different voltages: $eU/k_BT_c = 21$ (top) and $eU/k_BT_c = 46$ (bottom). Black lines denote the IL-poor phase whereas blue lines denote the IL-rich phase. Red point marks the chemical potential at the capillary ionization transition, $\mu_{ci}/k_BT_c = -4.57$, which correspond to the intersection point between both branches (IL-rich and IL-poor) of the grand potential. **(b)** Grand potential as a function of the temperature at fixed chemical potential $\mu_{ci}/k_BT_c = -4.57$ calculated at two different voltages: $eU/k_BT_c = 21$ (top) and $eU/k_BT_c = 46$ (bottom). Black lines denote the IL-poor phase whereas blue lines denote the IL-rich phase. Red point marks the temperature at the capillary ionization transition, $T_{ci}/T_c = 0.838$, which correspond to the intersection point between both branches (IL-rich and IL-poor) of the grand potential.

we have considered the grand potential as a function of three parameters, temperature T/T_{ci}, chemical potential μ/k_BT_c and voltage eU/k_BT_c. The results obtained by keeping two of these parameters constant and varying the other one should be consistent, which is a way to check our calculations. Figures B.2b show the grand potential as a function of the temperature at fixed chemical potential $\mu_{ci}/k_BT_c = -4.57$ for two different voltages $eU/k_BT_c = 21$ and $eU/k_BT_c = 46$, the intersection temperature, $T_{ci}/T_c = 0.838$, marks the capillary ionization transition. This is consistent with Figure B.2a.

Consistently, Figure B.3 shows the grand potential difference, $\Delta\Omega = \Omega_{rich} - \Omega_{poor}$, as a

function of the applied voltage at fixed chemical potential $\mu_{ci}/k_BT_c = -4.57$ and temperature $T_{ci}/T_c = 0.838$. Capillary ionization occurs when the curve crosses the zero-line, in this case at $eU/k_BT_c = 21$ and $eU/k_BT_c = 46$.

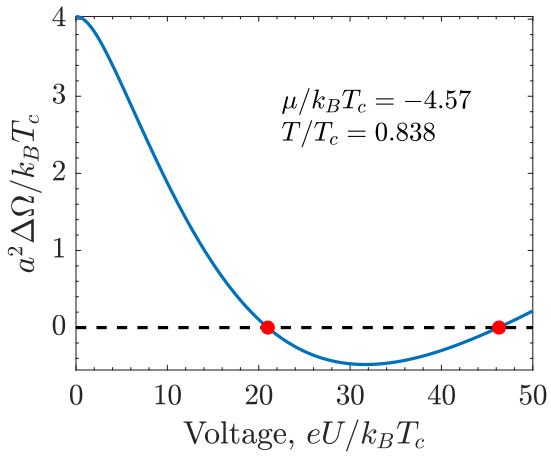

FIGURE B.3 Grand potential difference as a function of the voltage at fixed chemical potential $\mu_{ci}/k_BT_c = -4.57$ and temperature $T_{ci}/T_c = 0.838$. The grand potential difference is calculated as $\Delta\Omega = \Omega_{rich} - \Omega_{poor}$. The red points mark the voltages at which capillary ionization occurs, $eU/k_BT_c = 21$ and $eU/k_BT_c = 46$. This is consistent with the results shown in the previous figures.

Appendix C

Temperature effect on the Bjerrum length

To single out the effects related to demixing, we have assumed the relative dielectric constant, ϵ_r as temperature independent. At room temperature, ϵ_r ranges from 80 for water down to about 10 for less polar solvents like alkohols and increases monotonically with increasing temperature [169–171]. Correspondingly the Bjerrum length $\lambda_B = e^2/(\epsilon_r k_B T)$ acquires a relatively weak dependence on temperature and can increase or decrease with temperature. We have assumed $\lambda_B/a = \lambda_B^c(T_c/T)$. However, for simplicity we could assume a temperature-independent Bjerrum length $\lambda_B = a$ (corresponding to $\epsilon_r \approx 80$ at room temeprature). Figure C.1 shows that the temperature dependence and the choice of ϵ_r do not affect our results qualitatively.

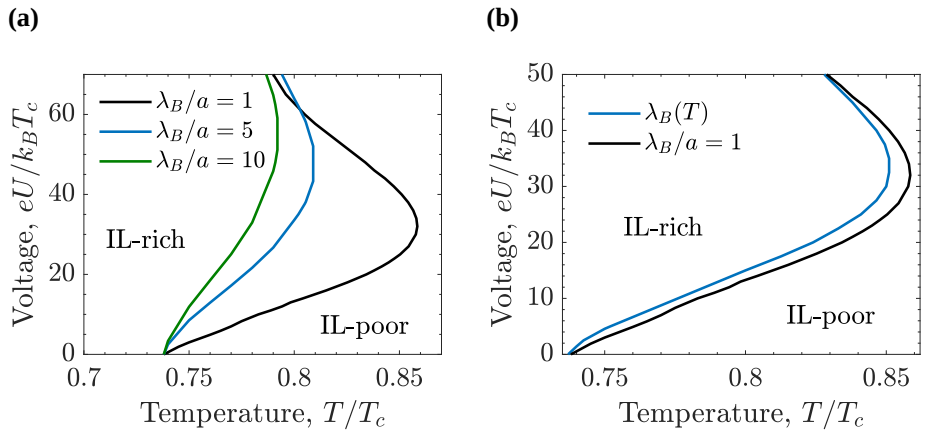

FIGURE C.1 Effect of Bjerrum length on voltage-induced capillary ionization transitions. (a) Phase diagrams in the temperature-voltage plane showing the locations of first-order transitions between the IL-rich and IL-poor phases for a few values of the Bjerrum length λ_B expressed in terms of the ion diameter a. **(b)** Phase diagrams for the Bjerrum length $\lambda_B/a = 1$ and for a temperature-dependent Bjerrum length $\lambda_B(T) = \lambda_B^c(T_c/T)$, where λ_B^c $(= a)$ is the Bjerrum length at the critical temperature T_c. This temperature dependence of $\lambda_B(T)$ means that ϵ_r is temperature independent.

Appendix D

Units conversion in LAMMPS

In Chapter 8, molecular simulations were performed in real units. However, in order to compare the results obtained with those obtained from our model, a transformation from real units to reduced is required. Recalling the parameters used in the molecular simulations, we have

$$\epsilon = 0.238\,\mathrm{Kcal/mol}$$
$$a = 3.4\,\text{Å}$$
$$q = 0.25\,\mathrm{e}$$
$$\rho_{tot} = 0.0221\,\text{Å}^{-3}$$

With $\epsilon/k_B = 119.846\,\mathrm{K}$ then, the reduced quantities are

$$T^* = \frac{k_B T(K)}{\epsilon} = \frac{T(K)}{119.846} \qquad \text{Reduced temperature} \tag{6}$$

$$q^* = \frac{q(e)}{\epsilon\sqrt{4\pi\epsilon_0 a}} = 5.06434 \qquad \text{Reduced charge} \tag{7}$$

$$u^* = \frac{U}{\epsilon N} = \frac{U(\mathrm{Kcal/mol})}{0.238N} \qquad \text{Reduced energy} \tag{8}$$

Now, we express the capacitance and voltage in thermal units. Thermal voltage is given by

$$\frac{eU}{k_B T_c} = \frac{eU(eV)}{8.617333262 \times 10^{-5}(eVK^{-1})T_c(K)} \tag{9}$$

Regarding the thermal capacitance per unit of surface area, we have

$$\frac{C}{C_H} = \frac{a(\text{Å})Q(e)w^{-2}(\text{Å}^{-2})}{U(V)\epsilon_0(eV^{-1}\text{Å}^{-1})} \tag{10}$$

where $C_H = \epsilon_0/a$ is the Helmholtz capacitance. Additionally, the permitivity ϵ_0 must be expressed in units $e^2(eV)^{-1}\text{Å}^{-1}$, then

$$\frac{C}{C_H} = \frac{a(\text{Å})\sigma_q(e/\text{Å}^{-2})}{0.0055263U(V)(e^2(eV)^{-1}\text{Å}^{-1})} \tag{11}$$

The potential energy exerted by the electrodes over the ions [1] has been calculated by means of three simulations:

1) All wall's particle interactions set to zero (except for a small wall-particle repulsion to avoid overlaps with the electrodes) to obtain $U_{\text{W}p} = 0$.
2) All wall's solvent-particle interactions set to zero to obtain $U_{\text{W}s} = 0$.
3) The wall-ion interaction set to $U_{\text{W}i} = U_{\text{W}s=0} - U_{\text{W}p=0}$.

In reduced units, and divided by the number of particles, one gets $U_{\text{W}\pm}/N_{\pm}\epsilon = -0.385$. This energy is due to the presence of two walls of area $L_xL_y/a^2 \approx 153$. The contribution to the ion particle energy because of the presence of the walls per unit area is

$$\frac{U_{\text{W}\pm}a^2}{N_{\pm}\epsilon L_xL_y} = -0.00252 \tag{12}$$

The calculation has been run for $k_BT/\epsilon = 4.17$ (that is, $500\,\text{K}$ in LAMMPS real units, recalling that $T_c \approx 360\,\text{K}$).

[1] The solvent particles only experience a short term repulsion; therefore its net contribution is almost zero.

Computational tools

Most of the calculations (analytical and numerical) presented in this thesis, as well as the result plots, have been done using MATLAB® software [172]. In the case of the single-charged surface system, the `bvp4c` routine of the same software was implemented.

The Molecular Dynamics simulations have been performed in LAMMPS simulator [158, 159, 173], and to visualize the simulations of the system under consideration, we have used the tool OVITO [174].

Finally, the text has been written in LaTex environment [175], and all the schemes have been done using Inkscape [176].

Bibliography

[1] T. Welton, “Room-Temperature Ionic Liquids. Solvents for Synthesis and Catalysis,” *Chem. Rev.*, vol. 99, no. 8, pp. 2071–2084, 1999.

[2] M. V. Fedorov and A. A. Kornyshev, “Ionic Liquids at Electrified Interfaces,” *Chem. Rev.*, no. 5, 2014.

[3] S. Perkin, “Ionic liquids in confined geometries,” *Phys. Chem. Chem. Phys.*, vol. 14, no. 15, pp. 5052–5062, 2012.

[4] D. Bonn, J. Eggers, J. Indekeu, J. Meunier, and E. Rolley, “Wetting and spreading,” *Rev. Mod. Phys.*, no. 2, 2009.

[5] L. D. Gelb, K. E. Gubbins, R. Radhakrishnan, and M. Sliwinska-Bartkowiak, “Phase separation in confined systems,” *Rep. Prog. Phys.*, vol. 62, no. 12, pp. 1573–1659, 1999.

[6] J. R. Miller and P. Simon, “Materials science – electrochemical capacitors for energy management,” *Science*, vol. 321, pp. 651–652, 2008.

[7] P. Simon and Y. Gogotsi, “Materials for electrochemical capacitors,” *Nature Mater.*, vol. 7, no. 11, pp. 845–854, 2008.

[8] F. Béguin, V. Presser, A. Balducci, and E. Frackowiak, “Carbons and electrolytes for advanced supercapacitors,” *Adv. Mater.*, vol. 26, no. 14, pp. 2219–2251, 2014.

[9] A. González, E. Goikolea, J. A. Barrena, and R. Mysyk, “Review on supercapacitors: Technologies and materials,” *Renew. Sust. Energ. Rev.*, vol. 58, pp. 1189–1206, 2016.

[10] S. Porada, R. Zhao, A. van der Wal, V. Presser, and P. Biesheuvel, “Review on the science and technology of water desalination by capacitive deionization,” *Prog. Mater. Sci.*, vol. 58, no. 8, pp. 1388–1442, 2013.

[11] M. E. Suss and V. Presser, “Water desalination with energy storage electrode materials,” *Joule*, vol. 2, no. 1, pp. 10–15, 2018.

[12] Y. Zhang, P. Srimuk, M. Aslan, M. Gallei, and V. Presser, “Polymer ion-exchange membranes for capacitive deionization of aqueous media with low and high salt concentration,” *Desalination*, vol. 479, p. 114331, 2020.

[13] D. Brogioli, “Extracting renewable energy from a salinity difference using a capacitor,” *Phys. Rev. Lett.*, vol. 103, no. 5, 2009.

[14] A. Härtel, M. Janssen, D. Weingarth, V. Presser, and R. van Roij, “Heat-to-current conversion of low-grade heat from a thermocapacitive cycle by supercapacitors,” *Energy Environ. Sci.*, vol. 8, no. 8, pp. 2396–2401, 2015.

[15] M. Janssen and R. van Roij, “Reversible heating in electric double layer capacitors,” *Phys. Rev. Lett.*, vol. 118, no. 9, p. 96001, 2017.

[16] J. Chmiola, G. Yushin, Y. Gogotsi, C. Portet, P. Simon, and P. L. Taberna, “Anomalous increase in carbon capacitance at pore sizes less than 1 nanometer,” *Science*, vol. 313, p. 1760, 2006.

[17] E. Raymundo-Piñero, K. Kierczek, J. Machnikowski, and F. Béguin, “Relationship between the nanoporous texture of activated carbons and their capacitance properties in different electrolytes,” *Carbon*, vol. 44, pp. 2498–2507, 2006.

[18] S. Kondrat and A. Kornyshev, “Superionic state in double-layer capacitors with nanoporous electrodes,” *J. Phys.: Condens. Matter*, vol. 23, p. 022201, 2011.

[19] S. Kondrat, C. R. Pérez, V. Presser, Y. Gogotsi, and A. A. Kornyshev, “Effect of pore size and its dispersity on the energy storage in nanoporous supercapacitors,” *Energy Environ. Sci.*, vol. 5, p. 6474, 2012.

[20] C. Péan, C. Merlet, B. Rotenberg, P. A. Madden, P.-L. Taberna, B. Daffos, M. Salanne, and P. Simon, “On the dynamics of charging in nanoporous carbon-based supercapacitors,” *ACS Nano*, vol. 8, p. ACS Nano, 2014.

[21] A. J. Pak and G. S. Hwang, “Charging rate dependence of ion migration and stagnation in ionic-liquid-filled carbon nanopores,” *J. Phys. Chem. C*, vol. 120, p. 24560, 2016.

[22] K. Breitsprecher, C. Holm, and S. Kondrat, “Charge me slowly, I am in a hurry: Optimizing charge–discharge cycles in nanoporous supercapacitors,” *ACS Nano*, vol. 12, no. 10, pp. 9733–9741, 2018.

[23] K. Breitsprecher, M. Janssen, P. Srimuk, B. L. Mehdi, V. Presser, C. Holm, and S. Kondrat, “How to speed up ion transport in nanopores,” *Nat. Commun.*, vol. 11, no. 1, 2020.

[24] C. Lian, H. Liu, C. Li, and J. Wu, “Hunting ionic liquids with large electrochemical potential windows,” *AIChE Journal*, vol. 65, no. 2, pp. 804–810, 2018.

[25] H. Tokuda, S.-J. Baek, and M. Watanabe, “Room-temperature ionic liquid-organic solvent mixtures: Conductivity and ionic association,” *Electrochemistry*, vol. 73, no. 8, pp. 620–622, 2005.

[26] V. V. Chaban, I. V. Voroshylova, O. N. Kalugin, and O. V. Prezhdo, “Acetonitrile boosts conductivity of imidazolium ionic liquids,” *J. Phys. Chem. B*, vol. 116, no. 26, pp. 7719–7727, 2012.

[27] E. Rilo, J. Vila, S. García-Garabal, L. M. Varela, and O. Cabeza, “Electrical conductivity of seven binary systems containing 1-ethyl-3-methyl imidazolium alkyl sulfate ionic liquids with water or ethanol at four temperatures,” *J. Phys. Chem. B*, vol. 117, no. 5, pp. 1411–1418, 2013.

[28] H. Montes-Campos, S. Kondrat, E. Rilo, O. Cabeza, and L. M. Varela, “Random-alloy model for the conductivity of ionic liquid–solvent mixtures,” *J. Phys. Chem. C.*, vol. 124, no. 22, pp. 11 754–11 759, 2020.

[29] R. Burt, K. Breitsprecher, B. Daffos, P.-L. Taberna, P. Simon, G. Birkett, X. S. Zhao, C. Holm, and M. Salanne, “Capacitance of nanoporous carbon-based supercapacitors is a trade-off between the concentration and the separability of the ions,” *J. Chem. Phys. Lett.*, 2016.

[30] R. Evans, U. M. B. Marconi, and P. Tarazona, “Fluids in narrow pores: Adsorption, capillary condensation, and critical points,” *J. Chem. Phys.*, vol. 84, no. 4, pp. 2376–2399, 1986.

[31] R. Evans, “Fluids adsorbed in narrow pores: Phase equilibria and structure,” *J. Condens. Matter Phys.*, vol. 2, no. 46, pp. 8989–9007, 1990.

[32] J. Jagiello and M. Thommes, “Comparison of DFT characterization methods based on n2, ar, CO2, and h2 adsorption applied to carbons with various pore size distributions,” *Carbon*, vol. 42, no. 7, pp. 1227–1232, 2004.

[33] P. I. Ravikovitch and A. V. Neimark, “Density functional theory model of adsorption on amorphous and microporous silica materials,” *Langmuir*, vol. 22, no. 26, pp. 11 171–11 179, 2006.

[34] G. Kupgan, T. P. Liyana-Arachchi, and C. M. Colina, “NLDFT pore size distribution in amorphous microporous materials,” *Langmuir*, vol. 33, no. 42, pp. 11 138–11 145, 2017.

[35] R. Parsons, “The electrical double layer: recent experimental and theoretical developments,” *Chem. Rev.*, vol. 90, no. 5, pp. 813–826, 1990.

[36] J.-P. Hansen and H. Löwen, “Effective interactions between electric double layers,” *Annu. Rev. Phys. Chem.*, vol. 51, no. 1, pp. 209–242, 2000.

[37] D. Ben-Yaakov, D. Andelman, R. Podgornik, and D. Harries, “Ion-specific hydration effects: Extending the Poisson-Boltzmann theory,” *Curr. Opin. Colloid Interface Sci.*, vol. 16, no. 6, pp. 542–550, 2011.

[38] H. Butt, K. Graf, and M. Kappl, *Physics and Chemistry of Interfaces*. Wiley, 2003.

[39] H. Wang and L. Pilon, "Accurate simulations of electric double layer capacitance of ultramicroelectrodes," *J. Phys. Chem. C.*, vol. 115, no. 33, pp. 16 711–16 719, 2011.

[40] N. Gavish, D. Elad, and A. Yochelis, "From solvent-free to dilute electrolytes: Essential components for a continuum theory," *J. Phys. Chem. Lett.*, vol. 9, no. 1, pp. 36–42, 2017.

[41] G. Minton and L. Lue, "The influence of excluded volume and excess ion polarisability on the capacitance of the electric double layer," *Mol. Phys.*, vol. 114, no. 16-17, pp. 2477–2491, 2016.

[42] J. L. Barrat, J. P. Hansen, and J. D. Weeks, *Basic concepts for simple and complex liquids*, 2005, vol. 58, no. 1.

[43] W. Olivares and D. A. McQuarrie, "On the theory of ionic solutions," *Biophys. J.*, vol. 15, no. 2, pp. 143–162, 1975.

[44] L. Magna, Y. Chauvin, G. P. Niccolai, and J. M. Basset, "The importance of imidazolium substituents in the use of imidazolium-based room-temperature ionic liquids as solvents for palladium-catalyzed telomerization of butadiene with methanol," *Organometallics*, vol. 22, no. 22, pp. 4418–4425, 2003.

[45] K. Ghandi, "A Review of Ionic Liquids, Their Limits and Applications," *Green and Sustainable Chemistry*, vol. 04, no. 01, pp. 44–53, 2014.

[46] N. D. Harper, K. D. Nizio, A. D. Hendsbee, J. D. Masuda, K. N. Robertson, L. J. Murphy, M. B. Johnson, C. C. Pye, and J. A. C. Clyburne, "Survey of Carbon Dioxide Capture in Phosphonium-Based Ionic Liquids and End-Capped Polyethylene Glycol Using DETA (DETA = Diethylenetriamine) as a Model Absorbent §," *Ind. Eng. Chem. Res.*, no. 5, pp. 2822–2830.

[47] V. A. Azov, K. S. Egorova, M. M. Seitkalieva, A. S. Kashin, and V. P. Ananikov, ""Solvent-in-Salt" Systems for Design of New Materials in Chemistry, Biology and Energy Research," *Chem. Soc. Rev.*, vol. 47, no. 4, pp. 1250–1284, 2018.

[48] S. Aparicio, M. Atilhan, and F. Karadas, "Thermophysical Properties of Pure Ionic Liquids: Review of Present Situation," *Ind. Eng. Chem. Res.*, vol. 49, no. 20, pp. 9580–9595, 2010.

[49] M. J. Earle, J. M. Esperança, M. A. Gilea, J. N. Canongia Lopes, L. P. Rebelo, J. W. Magee, K. R. Seddon, and J. A. Widegren, "The distillation and volatility of ionic liquids," *Nature*, vol. 439, no. 7078, pp. 831–834, 2006.

[50] D. R. Macfarlane, N. Tachikawa, M. Forsyth, J. M. Pringle, P. C. Howlett, G. D. Elliott, J. H. Davis, M. Watanabe, P. Simon, and C. A. Angell, "Energy applications of ionic liquids," *Energy Environ. Sci.*, vol. 7, no. 1, pp. 232–250, 2014.

[51] R. S. Borges, H. Ribeiro, R. L. Lavall, and G. G. Silva, “Temperature stable supercapacitors based on ionic liquid and mixed functionalized carbon nanomaterials,” *J. Solid. State. Electrochem.*, vol. 16, no. 11, pp. 3573–3580, 2012.

[52] S. Fletcher, V. J. Black, I. Kirkpatrick, and T. S. Varley, “Quantum design of ionic liquids for extreme chemical inertness and a new theory of the glass transition,” *J. Solid. State. Electrochem.*, vol. 17, no. 2, pp. 327–337, 2013.

[53] N. V. Plechkova and K. R. Seddon, Eds., *Ionic Liquids Completely UnCOILed*. Hoboken, NJ: John Wiley & Sons, 2015.

[54] M. Gaune-Escard and K. R. Seddon, *Molten salts and ionic liquids: never the twain?* John Wiley & Sons, 2012.

[55] N. V. Plechkova and K. R. Seddon, “Applications of ionic liquids in the chemical industry,” *Chem. Soc. Rev.*, vol. 37, no. 1, pp. 123–150, 2008.

[56] A. Lewandowski and A. Świderska-Mocek, “Ionic liquids as electrolytes for Li-ion batteries—An overview of electrochemical studies,” *J. Power Sources*, vol. 194, no. 2, pp. 601–609, 2009.

[57] M. Galiński, A. Lewandowski, and I. Stępniak, “Ionic liquids as electrolytes,” *Electrochim. Acta.*, vol. 51, no. 26, pp. 5567–5580, 2006.

[58] I. Shown, A. Ganguly, L. C. Chen, and K. H. Chen, “Conducting polymer-based flexible supercapacitor,” *Energy Sci. Eng.*, vol. 3, no. 1, pp. 1–25, 2015.

[59] X. Sun, H. Luo, and S. Dai, “Ionic Liquids-Based Extraction: A Promising Strategy for the Advanced Nuclear Fuel Cycle,” *Chem. Rev.*, vol. 112, no. 4, pp. 2100–2128, 2012.

[60] A. Stojanovic and B. K. Keppler, “Ionic Liquids as Extracting Agents for Heavy Metals,” *Sep. Sci. Technol.*, vol. 47, no. 2, pp. 189–203, 2012.

[61] I. Kilpeläinen, H. Xie, A. King, M. Granstrom, S. Heikkinen, and D. S. Argyropoulos, “Dissolution of Wood in Ionic Liquids,” *J. Agric. Food Chem.*, vol. 55, no. 22, pp. 9142–9148, 2007.

[62] H. Wang, G. Gurau, and R. D. Rogers, “Ionic liquid processing of cellulose,” *Chem. Soc. Rev.*, vol. 41, no. 4, p. 1519, 2012.

[63] H.-P. Steinrück, J. Libuda, P. Wasserscheid, T. Cremer, C. Kolbeck, M. Laurin, F. Maier, M. Sobota, P. S. Schulz, and M. Stark, “Surface Science and Model Catalysis with Ionic Liquid-Modified Materials,” *Adv. Mater.*, vol. 23, no. 22-23, pp. 2571–2587, 2011.

[64] F. Endres, “Ionic liquids: solvents for the electrodeposition of metals and semiconductors,” *ChemPhysChem*, vol. 3, no. 2, pp. 144–154, 2002.

[65] M. C. Buzzeo, R. G. Evans, R. G. Compton *et al.*, "Non-haloaluminate room-temperature ionic liquids in electrochemistry-a review," *ChemPhysChem*, vol. 5, no. 8, pp. 1106–1120, 2004.

[66] D. R. MacFarlane, M. Forsyth, P. C. Howlett, J. M. Pringle, J. Sun, G. Annat, W. Neil, and E. I. Izgorodina, "Ionic liquids in electrochemical devices and processes: managing interfacial electrochemistry," *Acc. Chem. Res.*, vol. 40, no. 11, pp. 1165–1173, 2007.

[67] M. Salanne, "Ionic liquids for supercapacitor applications," *Top. Curr. Chem.*, vol. 375, no. 3, p. 63, 2017.

[68] O. Pizio, S. Sokołowski, and Z. Sokołowska, "Electric double layer capacitance of restricted primitive model for an ionic fluid in slit-like nanopores: A density functional approach," *J. Chem. Phys.*, vol. 137, no. 23, pp. 1–11, 2012.

[69] J. Bikerman, "XXXIX. Structure and capacity of electrical double layer," *Lond.Edinb.Dubl.Phil.Mag.*, vol. 33, no. 220, pp. 384–397, 1942.

[70] E. Wicke and M. Eigen, "Über den einfluß des raumbedarfs von ionen in wäßriger lösung auf ihre verteilung in elektrischen feld und ihre aktivitätskoeffizienten," *Zeitschrift für Elektrochemie, Berichte der Bunsengesellschaft für physikalische Chemie*, vol. 56, no. 6, pp. 551–561, 1952.

[71] V. Freise, "Zur theorie der diffusen doppelschicht," *Zeitschrift für Elektrochemie*, vol. 56, no. 8, pp. 822–827, 1952.

[72] M. Eigen and E. Wicke, "The thermodynamics of electrolytes at higher concentration," *J. Phys. Chem.*, vol. 58, no. 9, pp. 702–714, 1954.

[73] I. Borukhov, D. Andelman, and H. Orland, "Steric effects in electrolytes: A modified poisson-boltzmann equation," *Phys. Rev. Lett.*, vol. 79, no. 3, pp. 435–438, 1997.

[74] D. di Caprio, Z. Borkowska, and J. Stafiej, "Simple extension of the Gouy–Chapman theory including hard sphere effects." *J. Electroanal. Chem.*, vol. 540, pp. 17–23, 2003.

[75] K. B. Oldham, "A Gouy-Chapman-Stern model of the double layer at a (metal)/(ionic liquid) interface," *J. Electroanal. Chem.*, vol. 613, no. 2, pp. 131–138, 2008.

[76] M. McEldrew, Z. A. Goodwin, A. A. Kornyshev, and M. Z. Bazant, "Theory of the Double Layer in Water-in-Salt Electrolytes," *J. Phys. Chem. Lett.*, vol. 9, no. 19, pp. 5840–5846, 2018.

[77] K. Bohinc, V. Kralj-Iglič, and A. Iglič, "Thickness of electrical double layer. Effect of ion size," *Electrochim. Acta.*, vol. 46, no. 19, pp. 3033–3040, 2001.

[78] A. A. Kornyshev, "Double-Layer in Ionic Liquids: Paradigm Change?" *J. Phys. Chem. B*, vol. 111, no. 20, pp. 5545–5557, 2007.

[79] M. Girotto, R. M. Malossi, A. P. dos Santos, and Y. Levin, "Lattice model of ionic liquid confined by metal electrodes," *J. Chem. Phys.*, vol. 148, no. 19, p. 193829, 2018.

[80] M. T. Alam, M. M. Islam, T. Okajima, and T. Ohsaka, "Measurements of differential capacitance at mercury/room-temperature ionic liquids interfaces," *J. Phys. Chem. C.*, vol. 111, no. 49, pp. 18 326–18 333, 2007.

[81] R. Atkin and G. G. Warr, "Structure in confined room-temperature ionic liquids," *J. Phys. Chem. C*, vol. 111, no. 13, pp. 5162–5168, 2007.

[82] F. Endres, "Physical chemistry of ionic liquids," *Phys. Chem. Chem.*, vol. 12, no. 8, pp. 1648–1648, 2010.

[83] R. Atkin, N. Borisenko, M. Drüschler, S. Z. El Abedin, F. Endres, R. Hayes, B. Huber, and B. Roling, "An in situ stm/afm and impedance spectroscopy study of the extremely pure 1-butyl-1-methylpyrrolidinium tris(pentafluoroethyl)trifluorophosphate/au(111) interface: Potential dependent solvation layers and the herringbone reconstruction," *Phys. Chem. Chem.*, vol. 13, no. 15, pp. 6849–6857, 2011.

[84] M. Mezger, H. Schroder, H. Reichert, S. Schramm, J. S. Okasinski, S. Schoder, V. Honkimaki, M. Deutsch, B. M. Ocko, J. Ralston, M. Rohwerder, M. Stratmann, and H. Dosch, "Molecular Layering of Fluorinated Ionic Liquids at a Charged Sapphire (0001) Surface," *Science*, vol. 322, no. 5900, pp. 424–428, 2008.

[85] M. Mezger, R. Roth, H. Schröder, P. Reichert, D. Pontoni, and H. Reichert, "Solid-liquid interfaces of ionic liquid solutions - Interfacial layering and bulk correlations," *J. Chem. Phys.*, vol. 142, no. 16, 2015.

[86] S. Perkin, L. Crowhurst, H. Niedermeyer, T. Welton, A. M. Smith, and N. N. Gosvami, "Self-assembly in the electrical double layer of ionic liquids," *Chem. Commun.*, vol. 47, no. 23, pp. 6572–6574, 2011.

[87] V. Lockett, R. Sedev, J. Ralston, M. Horne, and T. Rodopoulos, "Differential Capacitance of the Electrical Double Layer in Imidazolium-Based Ionic Liquids: Influence of Potential, Cation Size, and Temperature," *J. Phys. Chem. C.*, vol. 112, no. 19, pp. 7486–7495, 2008.

[88] F. Silva, C. Gomes, M. Figueiredo, R. Costa, A. Martins, and C. M. Pereira, "The electrical double layer at the [BMIM][PF6] ionic liquid/electrode interface - Effect of temperature on the differential capacitance," *J. Electroanal. Chem.*, vol. 622, no. 2, pp. 153–160, 2008.

[89] M. Drüschler, N. Borisenko, J. Wallauer, C. Winter, B. Huber, F. Endres, and B. Roling, "New insights into the interface between a single-crystalline metal electrode and an extremely pure ionic liquid: slow interfacial processes and the influence of temperature on interfacial dynamics," *Phys. Chem. Chem.*, vol. 14, no. 15, pp. 5090–5099, 2012.

[90] V. B. Ivaništšev, K. Kirchner, and M. V. Fedorov, “Double layer in ionic liquids: capacitance vs temperature,” 2017.

[91] M. Holovko, V. Kapko, D. Henderson, and D. Boda, “On the Influence of Ionic Association on the Capacitance of an Electrical Double Layer,” *Chem. Phys. Lett.*, vol. 341, no. 3-4, pp. 363–368, 2001.

[92] J. Reszko-Zygmunt, S. Sokołowski, D. Henderson, and D. Boda, “Temperature dependence of the double layer capacitance for the restricted primitive model of an electrolyte solution from a density functional approach,” *J. Chem. Phys.*, vol. 122, no. 8, p. 084504, 2005.

[93] M. Chen, Z. A. H. Goodwin, G. Feng, and A. A. Kornyshev, “On the Temperature Dependence of the Double Layer Capacitance of Ionic Liquids,” *J. Electroanal. Chem.*, vol. 819, pp. 347–358, 2018.

[94] J. Vatamanu, O. Borodin, and G. D. Smith, “Molecular simulations of the electric double layer structure, differential capacitance, and charging kinetics for n-methyl-n-propylpyrrolidinium bis(fluorosulfonyl)imide at graphite electrodes,” *J. Phys. Chem. B*, vol. 115, no. 12, pp. 3073–3084, 2011.

[95] M. Z. Bazant, B. D. Storey, and A. A. Kornyshev, “Double layer in ionic liquids: Overscreening versus crowding,” *Phys. Rev. Lett.*, vol. 106, no. 4, p. 46102, 2011.

[96] V. Lockett, M. Horne, R. Sedev, T. Rodopoulos, and J. Ralston, “Differential capacitance of the double layer at the electrode/ionic liquids interface,” *Phys. Chem. Chem.*, vol. 12, no. 39, pp. 12 499–12 512, 2010.

[97] M. V. Fedorov, N. Georgi, and A. A. Kornyshev, “Double layer in ionic liquids: The nature of the camel shape of capacitance,” *Electrochem. commun.*, vol. 12, no. 2, pp. 296–299, 2010.

[98] C. Cruz, A. Ciach, E. Lomba, and S. Kondrat, “Electrical Double Layers Close to Ionic Liquid-Solvent Demixing,” *J. Phys. Chem. C*, vol. 123, no. 3, pp. 1596–1601, 2019.

[99] D. Di Caprio, Z. Borkowska, and J. Stafiej, “Specific ionic interactions within a simple extension of the Gouy-Chapman theory including hard sphere effects,” *J. Electroanal. Chem.*, vol. 572, no. 1, pp. 51–59, 2004.

[100] M. S. Kilic, M. Z. Bazant, and A. Ajdari, “Steric effects in the dynamics of electrolytes at large applied voltages. i. double-layer charging,” *Phys. Rev. E*, vol. 75, p. 021502, 2007.

[101] M. Fedorov and A. A. Kornyshev, “Towards understanding the structure and capacitance of electrical double layer in ionic liquids,” *Electrochim. Acta.*, vol. 53, no. 23, pp. 6835–6840, 2008.

[102] M. V. Fedorov and A. A. Kornyshev, "Ionic Liquid Near a Charged Wall: Structure and Capacitance of Electrical Double Layer," *J. Phys. Chem. B*, vol. 112, no. 38, pp. 11 868–11 872, 2008.

[103] N. Georgi, A. A. Kornyshev, and M. V. Fedorov, "The Anatomy of the Double Layer and Capacitance in Ionic Liquids with Anisotropic Ions: Electrostriction vs Lattice Saturation," *J. Electroanal. Chem.*, vol. 649, p. 261, 2010.

[104] M. M. Islam, M. T. Alam, T. Okajima, and T. Ohsaka, "Electrical Double Layer Structure in Ionic Liquids: An Understanding of the Unusual Capacitance-Potential Curve at a Nonmetallic Electrode," *J. Phys. Chem. C*, vol. 113, no. 9, pp. 3386–3389, 2009.

[105] M. Sha, Q. Dou, F. Luo, G. Zhu, and G. Wu, "Molecular Insights into the Electric Double Layers of Ionic Liquids on Au(100) Electrodes," *{ACS} Appl. Mater. Interfaces*, vol. 6, no. 15, pp. 12 556–12 565, 2014.

[106] B. Docampo-Álvarez, V. Gómez-González, O. Cabeza, V. B. Ivaništšev, L. J. Gallego, and L. M. Varela, "Molecular dynamics simulations of novel electrolytes based on mixtures of protic and aprotic ionic liquids at the electrochemical interface: Structure and capacitance of the electric double layer," *Electrochim. Acta.*, vol. 305, pp. 223–231, 2019.

[107] R. Górniak and S. Lamperski, "On the influence of physical parameters on the properties of the electric double layer modelled by soft potentials. A Monte Carlo study," *Electrochim. Acta.*, vol. 286, pp. 279–286, 2018.

[108] A. C. Forse, J. M. Griffin, C. Merlet, P. M. Bayley, H. Wang, P. Simon, and C. P. Grey, "NMR Study of Ion Dynamics and Charge Storage in Ionic Liquid Supercapacitors," *J. Am. Chem. Soc.*, vol. 137, no. 22, pp. 7231–7242, 2015.

[109] M. Brüssel, M. Brehm, T. Voigt, and B. Kirchner, "Ab initio molecular dynamics simulations of a binary system of ionic liquids," *Phys. Chem. Chem.*, vol. 13, no. 30, pp. 13 617–13 620, 2011.

[110] P. Wu, J. Huang, V. Meunier, B. G. Sumpter, and R. Qiao, "Voltage dependent charge storage modes and capacity in subnanometer pores," *J. Phys. Chem. Lett.*, vol. 3, no. 13, pp. 1732–1737, 2012.

[111] G. Feng and P. T. Cummings, "Supercapacitor Capacitance Exhibits Oscillatory Behavior as a Function of Nanopore Size," *J. Phys. Chem. Lett.*, vol. 2, pp. 2859–2864, 2011.

[112] D. E. Jiang, Z. H. Jin, and J. Z. Wu, "Oscillation of Capacitance inside Nanopores," *Nano Lett.*, vol. 11, pp. 5373–5377, 2011.

[113] R. Szparaga, C. E. Woodward, and J. Forsman, "Capillary condensation of ionic liquid solutions in porous electrodes," *J. Phys. Chem. C*, vol. 117, no. 4, pp. 1728–1734, 2013.

[114] J. Comtet, A. Niguès, V. Kaiser, B. Coasne, L. Bocquet, and A. Siria, "Nanoscale capillary freezing of ionic liquids confined between metallic interfaces and the role of electronic screening," *Nat. Mater.*, vol. 16, no. 6, pp. 634–639, 2017.

[115] C. Alba-Simionesco, B. Coasne, G. Dosseh, G. Dudziak, K. E. Gubbins, R. Radhakrishnan, and M. Sliwinska-Bartkowiak, "Effects of confinement on freezing and melting," *J. Phys. Condens. Matter*, vol. 18, no. 6, pp. R15–R68, 2006.

[116] A. Elshwishin, J. Köser, W. Schröer, and B. Qiao, "Liquid-liquid phase separation of ionic liquids in solutions: Ionic liquids with the triflat anion solved in aryl halides," *J. Mol. Liq.*, vol. 192, pp. 127–136, 2014.

[117] J. Rotrekl, J. Storch, P. Velíšek, W. Schröer, J. Jacquemin, Z. Wagner, P. Husson, and M. Bendová, "Liquid Phase Behavior in Systems of 1-Butyl-3-alkylimidazolium bis{(trifluoromethyl)sulfonyl}imide Ionic Liquids with Water: Influence of the Structure of the C5 Alkyl Substituent," *J. Solution. Chem.*, vol. 46, no. 7, pp. 1456–1474, 2017.

[118] H. Nishimori and G. Ortiz, *Elements of Phase Transitions and Critical Phenomena*. Oxford University Press, 2010.

[119] P. Yatsyshin, N. Savva, and S. Kalliadasis, "Geometry-induced phase transition in fluids: Capillary prewetting," *Phys. Rev. E*, vol. 87, no. 2, p. 020402, 2013.

[120] J. Jiang and S. I. Sandler, "Capillary phase transitions of linear and branched alkanes in carbon nanotubes from molecular simulation," *Langmuir*, vol. 22, no. 17, pp. 7391–7399, 2006.

[121] A. Malijevský and A. O. Parry, "Condensation and evaporation transitions in deep capillary grooves," *J. Condens. Matter Phys.*, vol. 26, no. 35, 2014.

[122] S. Monfared, T. Zhou, J. E. Andrade, K. Ioannidou, F. Radjai, F.-J. Ulm, and R. J.-M. Pellenq, "The effect of confinement on capillary phase transition in granular aggregates," *arXiv preprint arXiv:2008.04201*, 2020.

[123] K. Binder and D. P. Landau, "Capillary condensation in the lattice gas model: A Monte Carlo study," *J. Chem. Phys.*, vol. 96, no. 2, pp. 1444–1454, 1992.

[124] G. G. Láng, "Interface stress measurements in an electrochemical environment," *Encyclopedia of Interfacial Chemistry: Surface Science and Electrochemistry*, pp. 195–206, 2018.

[125] G. Lippmann, "Relations entre les phénoménes électriques et capillaires," Ph.D. dissertation, Gauthier-Villars Paris, France, 1875.

[126] F. Mugele and J. C. Baret, "Electrowetting: From basics to applications," *J. Condens. Matter Phys.*, vol. 17, no. 28, 2005.

[127] J. Berthier, “Electrowetting Theory,” in *Micro-Drops and Digital Microfluidics*. Elsevier, 2013, pp. 161–224.

[128] A. O. Parry and R. Evans, “Universal fluctuation-induced corrections to the Kelvin equation for capillary condensation.”

[129] J. Powles, “On the validity of the Kelvin equation,” *J. Phys. A: Math. Gen.*, vol. 18, no. 9, p. 1551, 1985.

[130] A. Malijevskỳ, A. O. Parry, and M. Pospíšil, “Edge contact angle and modified Kelvin equation for condensation in open pores,” *Phys. Rev. E*, vol. 96, no. 2, p. 020801, 2017.

[131] C. Cruz, S. Kondrat, E. Lomba, and A. Ciach, “Effect of proximity to ionic liquid-solvent demixing on electrical double layers,” *J. Mol. Liq.*, vol. 294, p. 111368, 2019.

[132] F. Pousaneh, A. Ciach, and A. Maciołek, “Effect of ions on confined near-critical binary aqueous mixture,” *Soft Matter*, vol. 8, no. 29, pp. 7567–7581, 2012.

[133] F. Pousaneh, A. Ciach, and A. Maciołek, “How ions in solution can change the sign of the critical Casimir potential,” *Soft Matter*, vol. 10, no. 3, pp. 470–483, 2014.

[134] V. Kralj-Iglič and A. Iglič, “A Simple Statistical Mechanical Approach to the free Energy of the Electric Double Layer Including the Excluded Volume Effect,” *J. Phys. II*, vol. 6, no. 4, pp. 477–491, 1996.

[135] L. G. Gagliardi, C. B. Castells, C. Ràfols, M. Rosés, and E. Bosch, “Static Dielectric Constants of Acetonitrile/Water Mixtures at Different Temperatures and Debye−Hückel A and a 0 B Parameters for Activity Coefficients,” *J. Chem. Eng. Data*, vol. 52, no. 3, pp. 1103–1107, 2007.

[136] S. Riniker, B. A. C. Horta, B. Thijssen, S. Gupta, W. F. van Gunsteren, and P. H. Hünenberger, “Temperature Dependence of the Dielectric Permittivity of Acetic Acid, Propionic Acid and Their Methyl Esters: A Molecular Dynamics Simulation Study,” *ChemPhysChem*, vol. 13, no. 5, pp. 1182–1190, 2012.

[137] M. Orhan, “Dielectric and Transport Properties of Acetonitrile at Varying Temperatures: a Molecular Dynamics Study,” *Bull. Korean Chem. Soc.*, vol. 35, no. 5, pp. 1469–1478, 2014.

[138] E. Gongadze and A. Iglič, “Decrease of permittivity of an electrolyte solution near a charged surface due to saturation and excluded volume effects,” *Bioelectrochemistry*, vol. 87, pp. 199–203, 2012.

[139] M. Girotto, A. P. dos Santos, and Y. Levin, “Simulations of ionic liquids confined by metal electrodes using periodic Green functions,” *J. Chem. Phys.*, vol. 147, no. 7, p. 074109, 2017.

[140] A. Ciach, J. Pękalski, and W. T. Góźdź, "Origin of similarity of phase diagrams in amphiphilic and colloidal systems with competing interactions," *Soft Matter*, vol. 9, no. 27, p. 6301, 2013.

[141] N. F. Carnahan and K. E. Starling, "Equation of State for Nonattracting Rigid Spheres," *J. Chem. Phys.*, vol. 51, no. 2, pp. 635–636, 1969.

[142] E. Gongadze and A. Iglič, "Asymmetric size of ions and orientational ordering of water dipoles in electric double layer model - an analytical mean-field approach," *Electrochim. Acta*, vol. 178, pp. 541–545, 2015.

[143] J. S. Sin, S. J. Im, and K. I. Kim, "Asymmetric electrostatic properties of an electric double layer: A generalized Poisson-Boltzmann approach taking into account non-uniform size effects and water polarization," *Electrochim. Acta*, vol. 153, pp. 531–539, 2015.

[144] E. Gongadze, L. Mesarec, V. Kralj-Iglic, and A. Iglic, "Asymmetric Finite Size of Ions and Orientational Ordering of Water in Electric Double Layer Theory Within Lattice Model," *Mini-Reviews Med. Chem.*, vol. 18, no. 18, pp. 1559–1566, 2018.

[145] A. Butka, V. R. Vale, D. Saracsan, C. Rybarsch, V. C. Weiss, and W. Schröer, "Liquid-Liquid Phase Transition in Solutions of Ionic Liquids with Halide Anions: Criticality and Corresponding States," *Pure Appl. Chem.*, vol. 80, no. 7, pp. 1613–1630, 2008.

[146] A. C. Forse, C. Merlet, J. M. Griffin, and C. P. Grey, "New Perspectives on the Charging Mechanisms of Supercapacitors," *J. Am. Chem. Soc.*, vol. 138, pp. 5731–5744, 2016.

[147] K. Breitsprecher, M. Abele, S. Kondrat, and C. Holm, "The effect of finite pore length on ion structure and charging," *J. Chem. Phys.*, 2017.

[148] J. C. Strikwerda, *Finite difference schemes and partial differential equations*. Siam, 2004, vol. 88.

[149] M. V. Fedorov and A. A. Kornyshev, "Ionic Liquid Near a Charged Wall: Structure and Capacitance of Electrical Double Layer," *J. Phys. Chem. B*, vol. 112, no. 38, pp. 11 868–11 872, 2008.

[150] M. T. Alam, M. M. Islam, T. Okajima, and T. Ohsaka, "Capacitance Measurements in a Series of Room-Temperature Ionic Liquids at Glassy Carbon and Gold Electrode Interfaces," *J. Phys. Chem. C.*, no. 42, 2008.

[151] M. Janssen, A. Härtel, and R. van Roij, "Boosting Capacitive Blue-Energy and Desalination Devices with Waste Heat," *Phys. Rev. Lett.*, vol. 113, no. 26, p. 268501, 2014.

[152] A. Härtel, M. Janssen, D. Weingarth, V. Presser, and R. van Roij, "Heat-to-Current Conversion of Low-Grade Heat from a Thermocapacitive Cycle by Supercapacitors," *Energ. Environ. Sci.*, vol. 8, no. 8, pp. 2396–2401, 2015.

[153] J. Wang, S.-P. Feng, Y. Yang, N. Y. Hau, M. Munro, E. Ferreira-Yang, and G. Chen, ""Thermal Charging" Phenomenon in Electrical Double Layer Capacitors," *Nano Lett.*, vol. 15, no. 9, pp. 5784–5790, 2015.

[154] M. Janssen, E. Griffioen, P. Biesheuvel, R. van Roij, and B. Erné, "Coulometry and Calorimetry of Electric Double Layer Formation in Porous Electrodes," *Phys. Rev. Lett.*, vol. 119, no. 16, p. 166002, 2017.

[155] W. Humphrey, A. Dalke, and K. Schulten, "VMD – Visual Molecular Dynamics," *J. Mol. Graphics*, vol. 14, pp. 33–38, 1996.

[156] F. R. Hockney and J. Eastwood, *Computer Simulation Using Particles*. Adam Hilger, 1988.

[157] I.-C. Yeh and M. L. Berkowitz, "Ewald summation for systems with slab geometry," *J. Chem. Phys.*, vol. 111, no. 7, pp. 3155–3162, 1999.

[158] S. Plimpton, "Fast parallel algorithms for short-range molecular dynamics," *J. Comp. Phys.*, vol. 117, pp. 1 – 19, 1995.

[159] "LAMMPS Molecular Dynamics Simulator."

[160] E. Lomba, "An efficient procedure for solving the reference hypernetted chain equation (rhnc) for simple fluids: Illustrative results with application to phase coexistence for a lennard-jones fluid," *Mol. Phys.*, vol. 68, pp. 87 – 95, 1989.

[161] E. Lomba and J. S. Høye, "Hncr - a program to calculate the structure and thermodynamics of binary mixtures of charged hard spheres," *Comp. Phys. Comm.*, vol. 69, pp. 420–428, 1992.

[162] N. G. Almarza, E. Lomba, C. Martin, and A. Gallardo, "Demixing in binary mixtures of apolar and dipolar hard spheres," *J. Chem. Phys.*, vol. 129, p. 234504, 2008.

[163] Z. Wang, Y. Yang, D. L. Olmsted, M. Asta, and B. B. Laird, "Evaluation of the constant potential method in simulating electric double-layer capacitors," *J. Chem. Phys.*, vol. 141, no. 18, p. 184102, 2014.

[164] S. K. Reed, O. J. Lanning, and P. A. Madden, "Electrochemical interface between an ionic liquid and a model metallic electrode," *J. Chem. Phys.*, vol. 126, p. 084704, 2007.

[165] T. R. Gingrich and M. Wilson, "On the ewald summation of gaussian charges for the simulation of metallic surfaces," *Chem. Phys. Lett.*, vol. 500, no. 1-3, pp. 178–183, 2010.

[166] P. Cats, R. S. Sitlapersad, W. K. den Otter, A. R. Thornton, and R. van Roij, "Capacitance and structure of electric double layers: Comparing brownian dynamics and classical density functional theory," 2021.

[167] B. Docampo-Álvarez, V. Gómez-González, O. Cabeza, V. B. Ivaništšev, L. J. Gallego, and L. M. Varela, "Molecular dynamics simulations of novel electrolytes based on mixtures of protic and aprotic ionic liquids at the electrochemical interface: Structure and capacitance of the electric double layer," *Electrochim. Acta*, vol. 305, pp. 223–231, 2019.

[168] D. Antypov, M. C. Barbosa, and C. Holm, "A simple non-local approach to treat size correlations within Poisson-Boltzmann theory," *Phys. Rev. E*, vol. 71, p. 061106, 2005.

[169] A. Catenaccio, Y. Daruich, and C. Magallanes, "Temperature dependence of the permittivity of water," *Chem. Phys. Lett.*, 2003.

[170] L. G. Gagliardi, C. B. Castells, C. Ràfols, M. Rosés, and E. Bosch, "Static dielectric constants of acetonitrile/water mixtures at different temperatures and debye-Hückel a and a_0b parameters for activity coefficients," *J. Chem. Eng. Data*, 2007.

[171] S. Riniker, B. A. C. Horta, B. Thijssen, S. Gupta, W. F. van Gunsteren, and P. H. Hünenberger, "Temperature dependence of the dielectric permittivity of acetic acid, propionic acid and their methyl esters: A molecular dynamics simulation study," *ChemPhysChem*, 2012.

[172] MATLAB, *version 9.3.0 (R2017b)*. Natick, Massachusetts: The MathWorks Inc., 2017.

[173] S. Plimpton, "Short-Range Molecular Dynamics," *J. Comput. Phys.*, vol. 117, no. 6, pp. 1–42, 1997.

[174] A. Stukowski, "Visualization and analysis of atomistic simulation data with OVITO - The Open Visualization Tool," *Modelling and Simulation in Material Science and Engineering*, vol. 18, no. 1, 2010.

[175] L. Lamport, "Latex: A document preparation system, adison," 1986.

[176] Inkscape Project, "Inkscape."

Institute of Physical
Chemistry
Polish Academy of Sciences

Kasprzaka 44/52
01-224 Warsaw,
Poland

www.ichf.edu.pl